THE DEVELOPMENT OF PHOSPHORESCENT NANOCLUSTERS FOR LIGHT EMITTING DIODES

By

Padmanaban Sasthan kuttipillai

A DISSERTATION

Submitted to
Michigan State University
in partial fulfillment of the requirements
for the degree of

Chemical Engineering – Doctor of Philosophy

2018

ABSTRACT

THE DEVELOPMENT OF PHOSPHORESCENT NANOCLUSTERS FOR LIGHT EMITTING DIODES

By

Padmanaban Sasthan kuttipillai

Organic light emitting diodes (OLEDs) are undoubtedly the most mature organic optoelectronic devices as they have been commercialized in cell phones, televisions, and wearable electronics displays and may potentially become a leading solid-state lighting technology. OLEDs continue to attract new applications and their market value is expected to grow to 50 billion USD by 2023 owing to their lower power consumption, ultra-thin form factor, fast response time, and unrivaled color rendering properties. However, several challenges are preventing OLEDs from achieving their full potential. These include a decrease in performance at higher brightness, lower light outcoupling efficiency, limited efficiency in the near-infrared, and the high cost associated with the heavy metal complex based phosphorescent emitters. In the first part of this thesis we seek to understand the factors determining recombination dynamics of charge carriers in OLEDs as they play a crucial role in device performance and lifetime. We develop a method utilizing sensing layers to probe recombination in OLEDs with various emissive layer architectures. We identify the factors that control recombination and provide profiles that can improve the quantum efficiency at higher brightness. The second aim of this thesis is to develop efficient, inexpensive phosphorescent emitters as alternatives to the widely used platinum and iridium complexes. We therefore have developed novel earth abundant metal halide based phosphorescent nanoclusters and demonstrate their application in optically and electrically pumped nanocluster light emitting diodes (NCLEDs). We utilize transient dynamics and density functional theory (DFT) calculations and identify host quenching and exciton formation efficiency as key factors for improving

electrically pumped devices. Based on this understanding, we have developed molybdenum nanoclusters and report the highest electrically-driven NCLED efficiency through modification of apical ligands. This work demonstrates the promising potential of phosphorescent, earth abundant and inexpensive metal halide nanoclusters that can extend deeper into the near-infrared and expand the catalog of emitters for low-cost optoelectronic applications.

ACKNOWLEDGMENTS

I would like to express my sincere gratitude to my advisor, Dr. Richard Lunt for his diligent guidance and continuous support throughout my doctoral program. Thank you for being an inspiration, your constant demand for high standards in executing and communicating research were instrumental to my personal and professional development as a person and a researcher. I am truly grateful for your patience, encouragement, timely feedback, and discussion of ideas. I also want to thank my thesis committee members: Dr. Scott Calabrese Barton, Dr. Rebecca Anthony and Dr. Tim Hogan not only for their time but for also providing insight on this work. I wish to thank our collaborators: Dr. Per Askeland, Dr. Benjamin Levine, Dr. Richard Staples, Dr. Dan Holmes, Dr. Nelson Sepulveda, Dr. Rafmag Cabrera, Dr. Ken Kearns, Dr. Tony, Dr. Sukrit, and Dr. Hunter for their invaluable assistance. My sincere appreciation to Melany Sponseller from the ONE Lab for helping me with the UPS measurement despite her busy schedule. Thanks to Scott Bankruff at the glass blowing facility in the chemistry lab for the prompt assistance making and sealing those reaction tubes.

Many thanks to Donna, Jennifer, Nikki, Tiffany, Kim, and Danielle in the CHEMS office for providing prompt and friendly support to move things quickly in my research. I thank both past and present members of the MOELab for their support and friendship that made my days at MSU enjoyable. I learned so much working with these talented colleagues. Special thanks to my desk buddy Peggy for being a great citizen of the lab and for your willingness to help me and others on many occasions. Thanks Chris and Yimu for helping me during the initial stage of the research. I am always amazed by Chris's knack for troubleshooting instruments in the laboratory. Pei, thank you for all the assistance in drawing beautiful molecules - you always seemed to be calm and

composed. Chenchen, you have a big heart, thank you for being generous and providing us with an endless supply of fruits and snacks. Alex, thank you for the afternoon pizza and the wonderful plants. Matt Bates, thanks for the help reading part of the thesis and being a great safety rep. for the lab. Many thanks to our postdocs, Dhanashree, Jorge, Lilli, and Dianyi for sharing their wealth of knowledge. Thanks to the undergraduates, John, Juan, Lucas, Tyler, Adam, Mark, Nathan, Kevin, Audrey, Matt, for all your hard work. I wish you all great success in the future. I appreciate my other friends at MSU: Aseel, Amrita, Easwar, Markus, Nick Kamar, Christine, Xinting, Hershey, Jake, Iman, David, Mr.Wu, you all made the coffee hours and other activities to look forward to.

A good support team is vital for surviving graduate school and staying sane. I would like to thank all my family and friends back home for their continued support. Friends here in Michigan: Wenberg's, Nandy, Renga, Gautham, Ganesh, Nag, Mathangi, Venkat, Shilpa and others in the US for providing me the support and encouragement throughout my PhD studies. Special thanks to Gayathri and Mathan for your friendship and hosting us on many weekends that helped me recover from the frustration of experimental work. Thanks Dad, Mom, and Arun for always believing in me - I owe completion of this thesis to my Dad. I am so thankful to my daughter Satvika for being the best cheerleader anyone could ever ask for. We are so blessed to have you in our lives and you will always be the beat of our heart. Lastly, I am grateful to my wife Ambujam for her unconditional love during the good and bad times, persistent encouragement, and emotional support throughout this journey. These past several years have been a rough ride both personally and professionally and I would not have made it without you. I feel these years showed us the importance of family and strengthened our commitment to each other and I look forward many more years of togetherness. Thank you and I love you!

TABLE OF CONTENTS

LIST OF TABLES

LIST OF FIGURES

KEY TO SYMBOLS AND ABBREVIATIONS

S	singlet
T	triplet
p	polaron
n	refractive index of the medium
E_i	eigen value of a state
E_i^{el}	electronic energy
E_i^{vib}	vibrational energy
c_1	positive integers
eV	electron-volt
m_s	z- component of angular momentum of electron
S^T	total spin quantum number
Q_i	normal mode coordinate
S_0	ground singlet state
S_1	first excited singlet state
n_i	number of excited quanta
$\hbar$	modified Planck's constant, 1.05×10^{-34} m^2 kg / s
h	Planck's constant, 6.626×10^{-34} m^2 kg / s
D	donor
D*	excited donor
A	acceptor
A*	excited Acceptor
k_F	rate of Förster transfer

r	distance between donor and acceptor
R_0	Förster radius
F_D	area normalized donor emission
σ_A	absorption cross section area of acceptor
k_D	Dexter rate constant
K	experimental factor
R_{D-A}	donor-Acceptor separation
Ř	total van der Walls radium
J	current Density
V	Voltage
$N_t(E)$	trap state energy distribution
N_{eff}	effective density of states
H	total concentration of traps
T_c	measure of steepness of the trap states
T	temperature
e	electronic charge
k_L	rate of Langevin recombination
n	electron concentration
p	hole concentration
t	time
°C	degree Celsius
%T	percentage transmission
I_0	intensity of reference beam

I	intensity of sample beam
b	path length
c	concentration
K_r	radiative rate constant
K_{nr}	non radiative rate constant
r_p	amplitude of p polarized light
r_s	amplitude of s polarized light
i	$\sqrt{-1}$
m	exponent in the cosine law
W	width of the substrate
H	distance between the source and substrate
Å	Angstrom unit
TF_i	initial tooling factor
TF_f	final tooling factor
I_{OLED}	device current
I_{det}	photo current
R	responsivity of the detector
P_{opt}	optical power
$\bar{R}$	average wavelength responsivity
cd	candela
sr	steradian
$\bar{\lambda}$	average wavelength
P_{flux}	photon flux

q	electric charge (1.602×10^{-19} coulombs)
F_{sensor}	fraction of sensor photon emission
I_{Sens}	EL intensity of sensor
I_{Emit}	EL intensity of emitter
QY_{Sens}	quantum yield of sensor
QY_{Emit}	quantum yield of emitter
a, b, c	lattice constants
C2/c	space group
C_n	electron capture coefficient
C_p	hole capture coefficient
C_s	solution concentration
n_i and p_i	intrinsic electron and hole concentration
d_{hkl}	inter planar spacing
hkl	miller indices of crystallographic plane
v_{ref}	reference sample NMR frequency
v_{sample}	sample NMR frequency
υ_{em}	emission calibration factors
υ_{ext}	excitation calibration factors
I^B_{ext}	blank excitation intensity
I^S_{ext}	sample excitation intensity
I^S_{em}	sample emission intensity
η_{out}	outcoupling efficiency
ε_r	dielectric constant

Ψ_i	wave functions
$\mathcal{H}$	Hamiltonian
$\phi_i^{\vec{R}}(\vec{r})$	electronic component of wave function
$\chi_i(\overrightarrow{R})$	vibrational component of wave function
ϕ_a	atomic orbital
σ	sigma bonding orbital
$\sigma*$	sigma antibonding orbital
π	pi bonding orbital
π^*	pi antibonding orbital
ω	angular frequency
$\tilde{\nu}$	wavenumber
$\Psi_{el,f}$	final electronic state
$\Psi_{el,i}$	initial electronic state
$\lvert e\hat{r}\rvert$	dipole operator
η_{PL}	photoluminescence efficiency
κ	dipole orientation factor
λ	wavelength
σ_A	absorption cross section area of acceptor
ε_0	permittivity of vacuum
μ	mobility
γ	recombination rate constant
μ_-	electron mobility
μ_+	hole mobility

ε	molar absorptivity
τ	luminescence lifetime
Δ	phase difference
Ψ	amplitude ratio
$\Phi[\lambda]$	luminosity function
η_p	luminous power efficiency
η_{ext}	external quantum efficiency
χ	spin formation efficiency
γ	charge balance
η_A	absorption efficiency
Alq_3	Tris-(8-hydroxyquinoline) aluminum
AM	Active matrix
AMOLED	Active matrix organic light emitting diode
BCP	Bathocuproine
BE	Binding energy
BTB	4,4'-bis(4,6-diphenyl-1,3,5-triazin-2-yl)biphenyl
CCT	Correlated color temperature
CBP	4'-Bis(N-carbazolyl)-1,1'-biphenyl
CRI	Color rendering index
D-EML	Double emissive layer
DCM	Dichloromethane
DFT	Density functional theory
DPEPO	Bis[2-(diphenylphosphino)phenyl] ether oxide

E-Host	3-(4-(9H-carbazol-9-yl)phenyl)-9-(4,6-diphenyl-1,3,5-triazin-2-yl)-9H–carbazole
EIA	Energy information administration
EIL	Electron injection layer
EL	Electroluminescence
EML	Emissive layer
EQE	External quantum efficiency
ET	Electron transport
ETL	Electron transport layer
ETM	Electron transport material
FRET	Förster resonance energy transfer
FTIR	Fourier transform infrared
G-EML	Graded emissive layer
HAT-CN	1,4,5,8,9,11-hexaazatriphenylene hexacarbonitrile
HBL	Hole blocking layer
H-Host	9,9'-diphenyl-9H ,9'H -3,3'-bicarbazole
HIL	Hole injection layer
HOMO	Highest occupied molecular orbital
HT	Hole transport
HTL	Hole transport layer
HTM	Hole transport material
IQE	Internal quantum efficiency
$Ir(mppy)_3$	Tris[2-(p-tolyl)pyridine]iridium(III)
$Ir(ppy)_3$	Tris[2-phenylpyridinato-C2,N]iridium(III)

$Ir(F_2ppy)_3$	Tris[2-(4,6-difluorophenyl)pyridinato C2,N]iridium(III)
$Ir(bzq)_3$	Fac-tris(benzo[h]quinoline) iridium(III)
$Ir(pic)_3$	Iridium tris-picolinate
IC	Internal conversion
ISC	Inter system crossing
ITO	Indium tin oxide
LCD	Liquid crystals display
LCAO	Linear combination of atomic orbitals
LEDs	Light emitting diodes
LiQ	8-hydroxy-quinolinato lithium
LMCT	Ligand to metal charge transfer
LUMO	Lowest unoccupied molecular orbital
MBE	Molecular beam epitaxy
MC	Monochromator
mcp	3-bis(N-carbazolyl)benzene
M-EML	Mixed emissive layer
MLCT	Metal to ligand charge transfer
MO	Molecular orbitals
MoOx	Molybdenum Oxide
MOVPE	Metal-organic vapor phase epitaxy
MS	Mass spectrometry
NCLED	Nanocluster light emitting diode
NIR	Near Infrared

NMR	Nuclear magnetic resonance
NPD	N,N′-di(1-naphthyl)-N,N′-diphenyl-(1,1′biphenyl)-4,4′-diamine
NTO	Natural transition orbitals
OFETs	Organic field effect transistors
OLEDs	Organic light emitting diodes
OVPD	Organic vapor phase deposition
PBMMA	Poly (butyl methacrylate-co-methyl methacrylate
PEDOT: PSS	Poly(3,4ethylenedioxythiophene)poly(styrene sulfonate)
PIC-TRZ	2-biphenyl-4,6-bis(12-phenylindolo[2,3-a]carbazol-11-yl) 1,3,5-triazine
PJT	Pseudo Jahn Teller
PLQY	Photoluminescence quantum yield
PM	Passive matrix
PMOLEDs	Passive matrix organic light emitting diodes displays
Poly-TPD	Poly(4-butylphenyldiphenylamine)
PPV	Polyphenylenvinylene
PtOEP	Platinum octa-ethyl-porphyrin
PTFE	Polytetrafluoroethylene
PVK	Polyvinylcarbazole
PyD-2Cz	2,6-di(9H-carbazol-9-yl) pyridine)
QCM	Quartz crystal monitor
QTof	Quadrupole -time of flight detector
RF	Radio frequency
RHEED	Reflection high-energy electron diffraction

RISC	Reverse intersystem crossing
RuOx	Ruthenium oxide
RZ	Recombination zone
SCE	Standard calomel electrode
SCLC	Space charge limited current
S-EML	Single emissive layer
SOC	Spin orbital coupling
SPA	Singlet polaron annihilation
SPPs	Surface plasmon polaritons
SSL	Solid-state lighting
STA	Singlet triplet annihilation
TADF	Thermally activated delayed fluorescence
TAPC	4,4-cyclohexylidenebis[N,N-bis(4-methylphenyl)benzenamine]
TAZ	3-(biphenyl-4-yl)-5-(4-tert-butylphenyl)-4-phenyl- 4H-1,2,4-triazole
TBA	Tetra butyl ammonium
TCTA	Tris (4-carbazoyl-9-ylphenyl)amine
TDDFT	Time-dependent density function theory calculations
TF	Tooling factor
TFTs	Thin film transistors
TLSC	Transparent luminescent concentrator
TPA	Triplet-polaron annihilation
TpBi	2,2′,2"-(1,3,5-benzinetriyl)-tris(1-phenyl-1-H-benzimidazole)
TPD	N, N′-Bis (3-methylphenyl)-N, N′-diphenylbenzidine

TAR	Trap assisted recombination
TTA	Triplet-triplet annihilation
UPS	Ultraviolet photoelectron spectroscopy
UV-VIS	Ultraviolet-Visible
UGH-3	1,3-bis(triphenylsilyl)benzene
VOx	Vanadium Oxide
VTE	Vacuum thermal evaporation
WPE	Wall plug efficiency
XRD	X-ray diffraction

Chapter 1 Introduction to Organic Light Emitting Diodes

Organic light emitting diodes (OLEDs) are now a key component in the displays of many cell phones, televisions, and are poised to become a leading solid state lighting technology.[1, 2] The improved understanding of photo physical and charge transport properties along with the high throughput synthetic, purification, and fabrication methods have resulted in better performance organic semiconductors and led to their application in various organic electronics devices such as OLEDs, organic field effect transistors (OFETs), solar cells, sensors, and electrochromic devices.[3] Organic semiconductors are composed of carbon and hydrogen atoms along with atoms such as nitrogen, sulfur, and oxygen. Although the electrical conductivity of these carbon based organic semiconductor materials have not reached the levels of inorganic semiconductors, they offer many unrivalled advantages such as tunable properties, low temperature processing, and mechanical flexibility.[4] They also provide the potential to fabricate electronic devices at low cost.

This thesis is aimed at understanding the recombination dynamics of OLEDs and the development of novel, inexpensive phosphorescent emitters based on molybdenum (Mo) halide based nanoclusters. These nanoclusters can act as an alternative emitter to the widely used noble, heavy metal complexes of Ir and Pt in OLEDs. In Chapter 1, we provide an overview of OLED technologies and the current challenges that OLEDs face. To provide the necessary background, Chapter 2 discusses the fundamentals of organic semiconductors physics as well as the basics of photoluminescence and electroluminescence processes. Chapter 3 details the experimental methods used throughout this thesis including, materials and optical characterization, device fabrication, and performance evaluation. Chapter 4 discusses the work carried out to understand

the recombination dynamics in OLEDs, fabricated with various emissive layer architectures. In Chapter 5, the first application of phosphorescent Mo based nanoclusters light emitting diodes (NCLEDs) is demonstrated. Insights on the factors that control the electroluminescence efficiency in these devices are provided. Chapter 6 extends this work and discusses the improvement of NCLEDs device performance thorough apical ligand control in the nanoclusters. We conclude in Chapter 7 and highlight various strategies to further improve the efficiency of NCLED devices.

1.1 Historic Development

We start with a brief review of major historical breakthroughs, which have occurred in the development of OLEDs. Electroluminescence (EL) is the process by which materials emit light in response to the applied voltage and is the underlying mechanism for the operation of OLEDs. In 1960, Pope et al. published the first report of EL from an organic single crystal of anthracene. The authors explained the EL based on injection and recombination of charge carriers in these organic materials. Despite the author's first demonstration of electroluminescence in organic crystals, the results did not attract much attention for several decades because of the very low efficiency, high driving voltage (400 V), and problems in scalability of single crystal growth. A significant step in realizing efficient EL in organic materials occurred in 1982 when Vincette et al used thermally evaporated films of micrometer thick anthracene.[5] In 1987, Tang and Van Slyke drastically improved the efficiency of their EL devices by forming heterojunctions using separate charge transport layers, including aromatic amine for hole transport and aluminum chelate for electron transport. By careful selection of materials with low mismatch of energy levels for charge transport, the turn on voltage of the devices was drastically reduced to 3.5 V. These devices reached a maximum external quantum efficiency (EQE) of 1% and showed good stability of operation for hundreds of hours.[6] Followed by this remarkable result, the demonstration of EL from

polyphenylenvinylene (PPV) and the solution processing method of fabricating OLEDs by Friend et al generated tremendous interest in developing organic materials for low cost and large area light emitting diode applications.[7]

Organic small molecules and polymers that were employed during the initial stages of the development of OLEDs suffered from intrinsically low internal quantum efficiency (IQE) of 25% due to the fluorescent nature of the emitters. The drawback of having an IQE limit of 25% from fluorescent emitters was overcome by the introduction of phosphorescent emitters which consist of heavy metal complexes, for example with Pt, Ir, and Ru.[8] The strong spin orbital coupling present in these noble metal complexes allow the relaxation of the forbidden triplet states to the ground state that led devices to achieve internal quantum efficiency of 100%.[9] The details of the different excited states and the luminescence process will be discussed in the Chapter 2. The first example of utilizing phosphorescence emitters in OLEDs was published by Baldo et al in 1998 using a red phosphorescent dye, platinum octa-ethyl-porphyrin platinum (PtOEP). The device performance was optimized by changing the doping concentration of the emitter and a maximum EQE of 4% was realized.[10] This work was quickly followed with the seminal demonstration of green phosphorescent OLEDs based on Ir complexes and laid the foundation for further development of OLEDs and ultimately helped OLEDs to come out of laboratory to become a key component in the modern displays and lighting technologies.[11]

1.2 Operating Principle

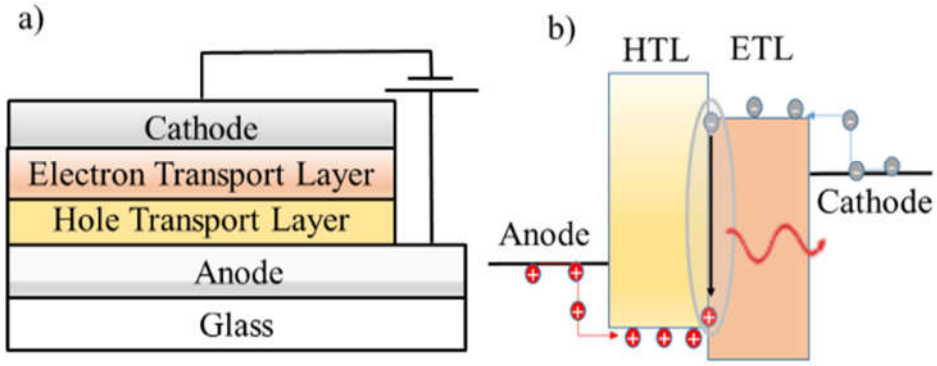

Figure 1.1 Bilayer OLED device architecture and working principle. a) Schematic representation of bilayer OLED consisting of hole transport layer (HTL) and electron transport layer (ETL). b) Simple representation of electroluminescence process such as hole injection from the anode, electron injection from the cathode, exciton formation at the interface of HTL and ETL because of the energy level alignment between the layers and relaxation of exciton while releasing excess energy in the form of photon.

OLEDs are electroluminescent devices that consist of multiple layers of thin films of organic semiconductors sandwiched between two electrodes. Figure 1.1a display an example two-layer device consisting of hole and electron transport layers and Figure 1.1b shows the basic process involved in the operation of OLEDs. When a sufficient voltage is applied across the electrodes, electric charges are injected from the opposite electrodes into the thin organic layers. Injected charges then recombine at an interface to form excitons due to the strong coulombic interaction. An exciton is an electron-hole pair, which may relax to emit a photon (light) or phonons (heat). While the intensity of the light emission from OLEDs can be controlled by the applied voltage, the wavelength (or color) of the light emission can be modified by changing bandgap of organic semiconductor materials offering a unique advantage to fabricate tunable light emitting diodes (LEDs).

1.3 External Quantum Efficiency

External quantum efficiency is the ratio of number photons emitted to the electron injected and it only account the photons emitted from the forward viewing hemisphere of the devices. EQE can be defined as the product of the four different efficiencies: spin formation (χ), charge balance (γ), photoluminescence (η_{PL}) and outcoupling (η_{out}) efficiencies as shown in the equation 1.1.

$$\eta_{\text{EQE}} = \chi \times \gamma \times \eta_{\text{PL}} \times \eta_{\text{out}} = \frac{\text{number of photons emitted}}{\text{number of electrons injected}}, \quad (1.1)$$

The spin formation efficiency (χ) is defined as the fraction of excitons that are allowed to decay radiatively. Depending on the type of emitter involved, the spin formation efficiency can have values of $\chi = 0.25$ for fluorescent emitters or 1 for phosphorescent emitters. The charge balance efficiency (γ) determines the fraction of excitons formed in the emissive layer for the electrons injected and can be used to quantify the charge leakage in the devices. Photoluminescence efficiency (η_{PL}) is defined as fraction excitons that actually undergo radiative relaxation. Outcoupling efficiency is a common bottleneck for many OLEDs device performance and it measures the fraction of generated photons that escapes in the forward viewing direction from the device. Due to refractive index mismatch between the organics, glass substrates, and the surrounding air, about 80 % of the generated light is trapped inside the devices. The internal quantum efficiency (η_{IQE}) is then defined as the product of spin formation (χ), charge balance (γ), photoluminescence (η_{PL}) efficiencies which represent the number of photons created for electron injected inside the devices. Since the spin formation and photoluminescence efficiencies are emitter specific properties; charge balance can be tuned by adopting different architecture incorporating additional layers to improve the charge injection, transport, and confinement in OLEDs. As a result, devices can achieve near unity of charge balance efficiency and have shown IQEs > 90%.

1.4 Device Architecture

As can be seen from the energy level diagram for the bilayer OLEDs (Figure 1b), a large mismatch exists between the energy level of the transport layers relative to the anode and cathode work functions respectively. This results in poor electron and hole injection into the emitter leading to low electroluminescent efficiency as well as the reduced lifetime in the devices as the energy barrier allow the excitons to accumulate near an interface and eventually leads to various exciton-exciton annihilation. To overcome this energy barrier, a multilayer architecture consisting of additional materials with favorable energy levels and preferential carrier transport has been introduced.[12] Figure 1.2 shows the evolution of OLED device architecture. As a result, these architectures reduced the charge injection barrier, improved charge transport, exciton formation efficiency, and most importantly the lifetime of the devices.[13] In addition, devices with multilayers allowed for the charge injection, transport, exciton formation and relaxation in OLEDs to be independently optimized.

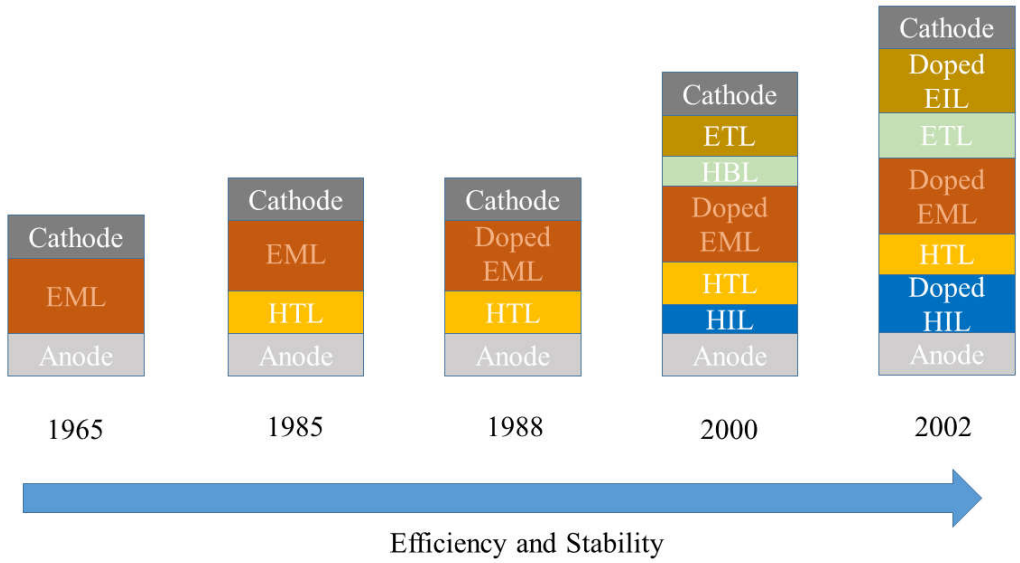

Figure 1.2 Evolution of OLED device architecture Schematics representing progress made in the OLED device architecture that improved the efficiency and stability of the devices over the

years (HIL: hole injection layer, HTL: hole transport layer, EML: emissive layer, HBL: hole blocking layer, ETL: electron transport layer, EIL: Electron injection layer)

In this section, we discuss various layers that constitute OLEDs and their functions to the operation of the device as well as provide examples of common organic materials being used in each layer.

1.4.1 Hole Injection Layer

The majority of OLEDs today use indium tin oxide (ITO) as an electrode due to the high optical transparency and good conductivity. However, the work function (4.8 eV) [14] is not ideal for hole injection into the organic layers used in fabricating OLEDs. For efficient injection of holes to the devices, hole injection layers (HILs) are necessary to reduce the hole injection barrier. In addition, HILs can also reduce the surface roughness of ITO. A typical hole injection layer consists of metal oxide layers such as vanadium oxide (VO_x), molybdenum oxide (MoO_x) and ruthenium oxide (RuO_x). These materials are mainly used in OLEDs fabricated using only vacuum thermal evaporation processes.[15]

For solution processing of OLEDs, polymers solution consisting of poly(3,4-ethylenedioxythiophene)poly(styrene sulfonate) (PEDOT-PSS) has been the most widely used HIL.[16] Recently, organic molecule consisting of 1,4,5,8,9,11-hexaazatriphenylene hexacarbonitrile (HAT-CN) [17] as well as graphene oxide have also been used as HILs in OLEDs.[18] Devices with efficient HILs shown to have improved performance such as low turn on voltage and higher power efficiency and significantly improved the lifetime of the devices by eliminating charge accumulation at the interface.[19]

1.4.2 Electron Injection Layer

To improve the electron injection, the barrier between the lowest unoccupied molecular orbitals (LUMO) level of the organics and the work function of the cathode should be minimized. Various low work function metals such as Li, Ca, and Mg have been used in OLEDs fabrication; however these metals are typically air sensitive and tend to react with organics causing faster degradation of devices.[20] Various ultrathin (~1nm) insulating layer made of LiF, CsF, CaF_2, BaF_2 have been introduced before the metal deposition and they have drastically increased the electron injection and improved the devices performance due to the band bending of organic layers when contacting the dielectrics.[21] The main drawback of these materials is the requirement for strict control over thickness as they have to be within 0.5 to 1 nm thick. At higher thicknesses these insulating materials reduce the electron injection efficiency in the devices.[22] To overcome this issue, Endo et al introduced a lithium quinolate complex such as 8-hydroxy-quinolinato lithium (LiQ) and their devices showed similar performances to LiF devices with less strict control over EIL thickness.[23] Examples of common HILs and EILs materials are shown in the Figure 1.3.

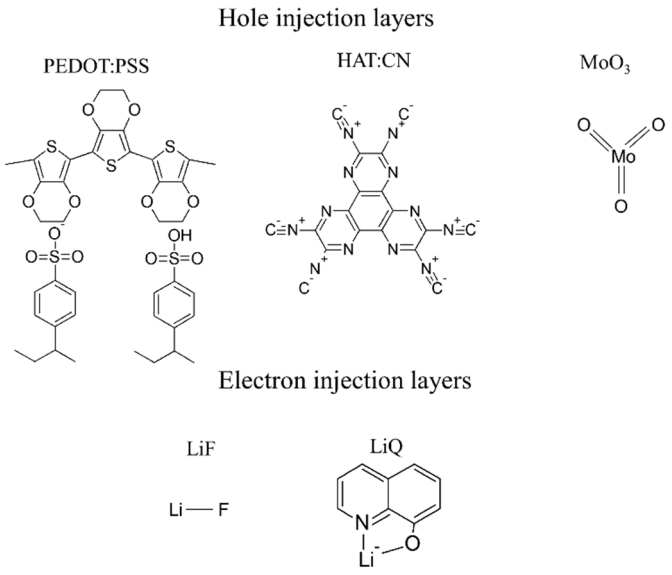

Figure 1.3 Electron and hole injection layers Example of molecular structure of commonly used hole and electron injection materials for OLEDs.

1.4.3 Hole Transport Layer

Hole transport layers (HTLs) aid in effectively transporting injected holes to the emissive layer in the multilayer OLED devices. In bilayer OLEDs, these transport layers can function both the transport and emissive layer because of their energetics and luminescence properties. Typical HTLs consist of electron donating groups such as triarylamine, diphenylamine, and carbazole. In addition to high hole mobilities, these materials should also have good thermal stability and a high glass transition temperature to yield a good quality thin film. The materials should also have favorable highest occupied molecular orbital (HOMO) levels with the neighboring layers with a minimum barrier for efficient transport of holes as well as shallow LUMO levels to block the electrons from the emissive layer.[24] Furthermore, they should also have large band gap so that they do not produce competing electroluminescence when incorporating into multilayer device architecture with a dedicated emissive layer. Figure 1.4 show some of the most commonly used HTLs materials such as N,N′-Di(1-naphthyl)-N,N′-diphenyl-(1,1′-biphenyl)-4,4′-diamine (NPD) and tris(4-carbazoyl-9-ylphenyl)amine (TCTA) OLEDs fabricated using thermal evaporation.

For solution processed OLEDs, finding suitable HTLs is challenging as the solvent used for the subsequent layers tend to remove the HTLs resulting poor performance in the devices. To address this, cross linkable hole transport material using thermal or photo cross linking methods have been developed.[25] These HTLs are resistant to solvents and have good thermal stability that allow subsequent layers to be deposited without removing the underneath layers. An example of commonly used polymer based HTLs poly (4-butylphenyldiphenylamine) (poly-TPD) is shown in the Figure 1.4.

1.4.4 Electron Transport Layer

Similar to HTLs, electron transport layers (ETLs) allow efficient transport of electrons to the emissive layer. ETLs generally contain electron withdrawing functional groups such as imidazole and triazole in their molecular structure. ETLs should have good electron mobility, an appropriate HOMO and LUMO levels for blocking holes and allowing efficient electron transport to the emissive layer respectively. Similar to HTLs , ETLs should also have high triplet energy to confine the triplets generated with in the emissive layer and large bandgap to avoid parasitic emission.[26] Figure 1.4 displays some of commonly used electron transport layers such as tris-(8-hydroxyquinoline)aluminum (Alq_3) , 2,2′,2"-(1,3,5-benzinetriyl)-tris(1-phenyl-1-H-benzimidazole (TpBi), and 3-(biphenyl-4-yl)-5-(4-tert-butylphenyl)-4-phenyl-4H-1,2,4-triazole (TAZ) in OLEDs.

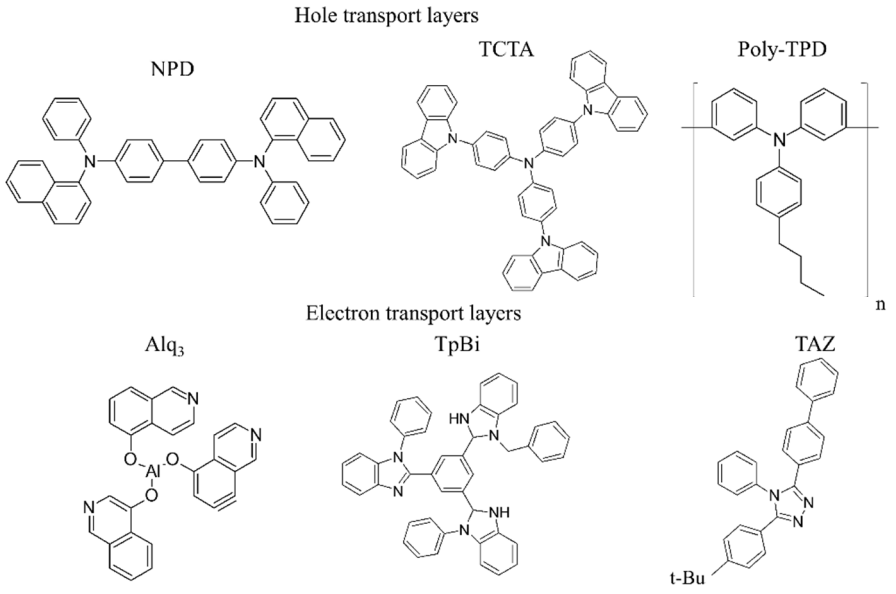

Figure 1.4 Hole and electron transport layer Molecular structure of commonly used hole and electron transport materials in OLEDs

Although these transport layers have favorable energetics to transport holes or electrons, they typically suffer from low injection efficiencies. This leads to ohmic losses and require higher field to drive the current and in some cases, allow carriers to build up on the interface, which will eventually reduce the performance and lifetime of the devices.[27] To address this, doped transport layers have been introduced. Similar to inorganic semiconductors, the conductivity of organic transport layers can also be tuned by doping with donor and acceptor molecules. In addition, doping organic semiconductor also increases the charge injection efficiency from the metal. The requirement of n-type dopant is that the dopant should have a higher HOMO level than the LUMO of the transport layer so that it can donate electrons to the transport layer, which leads to increase in the concentration of free electrons in the transport layer. Similarly, the p-type dopant, should accept electron from the transport layer creating excess holes in the transport layer. An example of p type dopants the organic molecules 2,3,5,6-tetrafluoro-7,7,8,8-tetracyanoquinodimethane (F_4-TCNQ) and the common n-type dopants are alkali metals such as Cs and Li. Charge injection

efficiency and the conductivity of the doped transport layers have been improved by the introduction of dopants that leads to devices with lower drive voltage and good stability.[28]

1.4.5 Host Material

In highly efficient OLEDs, emitters are typically doped at a very low concentration in a suitable host matrix to avoid self-quenching. The performance of the devices is optimized by changing the doping concentration of emitter in the host matrix. Successful host materials generally meet the following requirements: 1) the triplet energy of the hosts are higher than the emitter to avoid back transfer of energy from emitter to host; 2) hosts should also have favorable energy levels with the neighboring layers with good charge carrier mobilities for both electrons and holes; 3) should also have higher thermal and morphological stability to form better quality films.

Depending on the chemical structures, hosts can be predominantly hole transporting, electron transporting, or bipolar charge transporting.[29] Bipolar hosts are capable of transporting holes and electrons efficiently due to the presence of both electron donating and withdrawing functional groups linked to the molecular structure. However, they tend to have low triplet energies compared to the HT type and ET type hosts as the combination of electron donating and withdrawing groups in the same molecule unavoidably lowers the bandgap of the material via intermolecular charge transfer.

The current state of art OLED devices have been made by using the guest-host architecture. However, several shortcoming exists in this architecture as the host materials usually have higher bandgap resulting in unfavorable charge injection in the guest molecules that leads to higher turn on voltage. Additionally phase separation of guest and host molecules, resulted lower exciton formation efficiency in the devices due to the inefficient energy transfer.[30] To circumvent this

issue, various phosphorescence complexes with negligible self-quenching and good charge transport properties have been developed so that the devices can be made with a neat emissive layer. The un-doped devices have shown EQE of up to 31 % with neat emissive layer similar to the guest-host architecture, implying nearly 100% IQE and oriented dipoles.[31] In addition, having a neat emissive layer can simplify the device manufacturing, as the host-guest structure usually requires precise control for doping concentration.[32]

1.4.6 Emitters

Emitters are the light producers in the OLEDs and can be classified as fluorescent or phosphorescent depending on the type of excited states involved for the light production. Briefly there are two types of excited states can form in the organic semiconductor namely singlet and triplet excited states. These excited states differ by spin orientation of electrons that occupy the excited and ground states. That is, the electron in the excited singlet state and the electron in the ground state have opposite spins. In contrast, the electron in the triplet state has the identical spin orientation with the electron in the ground state. Chapter 2 will cover the origin of these excited states and provide details of optical processes such as the absorption, and relaxation of excited states.

1.4.6.1 Fluorescent Emitters

Emission in fluorescent emitters arise from the relaxation of singlet excited states to the ground state. Since electrical excitation creates singlet and triplet excited states in a 1:3 ratio, 75% of the excited states are unutilized in the florescent emitters due to the spin selection rules which restricts the relaxation of triplet state to the singlet ground state of the molecules.[33] As a result, the maximum IQE is only 25 % in this class of materials. Despite this lower IQE, fluorescent materials that emit particularly in the deep blue part of spectrum are still being used in current

OLED displays. Moreover, fluorescent emitters tend to have higher operational stability and the devices exhibit high color purity of electroluminescence than the phosphorescent emitters.[34] Conjugated organic molecules such as styrylbenzene, anthracene, and perylene; light emitting polymers such as polyfluorenes and fluorene-containing copolymers are the examples of fluorescent emitters.[35]

1.4.6.2 Phosphorescent Emitters

Phosphorescent emitters utilize both the singlet and triple excited states for light emission in OLEDs. Typical phosphorescent emitters consist of heavy, expensive metal atoms of Pt, Ir, and Ru surrounded by organic ligands. These emitters can be broadly classified as homoleptic and heteroleptic complexes depending on if the surrounding ligands are same or different. Platinum octaethylporphyrin (PtOEP) and tris[2-phenylpyridinato-C2,N]iridium(III)($Ir(ppy)_3$) were the first examples of widely used phosphorescent emitters in OLEDs. Electronic transitions in these transitional metal complexes predominantly involve the formation of metal to ligand charge transfer (MLCT) states. MLCT transitions occurs between the d orbital of the metal to the ligand centered π^*antibonding orbitals and routinely observed in d^6 and d^8 transition metal complexes. MLCT states play a crucial role to the photo physics of Ir based complexes and most importantly the energy of this transition can be modified by changing the metal center or ligand environment. This allows modification of the optical properties of these Ir complexes to cover the entire the visible spectrum with high photoluminescence efficiency. In addition, the presence of heavy metal atoms mixes the singlet and triplet excited states through strong spin orbital coupling (SOC) and allow the relaxation of forbidden triplet state to the ground state leading to both high PLQY for triplets and IQEs of up to 100 %.[8] The examples of Ir based complexes used in high efficiency OLEDs are given in the Figure 1.5 $Ir(ppy)_3$ is the most studied phosphorescent emitter and it exist

in two geometric isomers such as facial and meridional. The PLQY of facial isomers is higher than the mer-isomer and mer-isomer have red shifted emission compared with the fac-isomer. [36] It is therefore fortuitous that the initial demonstrations with this emitter serendipitously had predominately the fac-isomer. Figure 1.5 also highlights the subtle changes in the ligand environment and its effect on the emission color of the phosphorescent emitters.

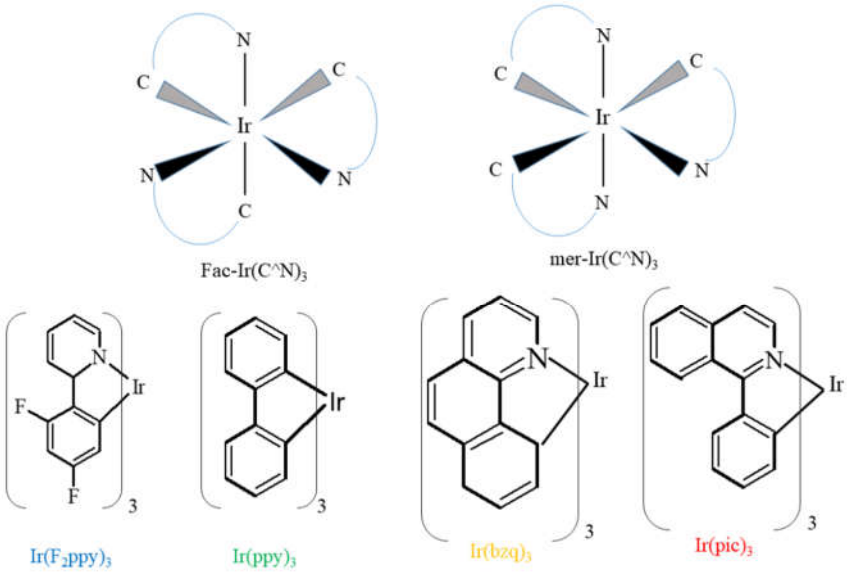

Figure 1.5 Examples of Ir based phosphorescent molecules

1.4.6.3 Thermally Activated Delayed Fluorescence Emitters

Despite the fact that phosphorescent emitter can theoretically produce an IQE of 100% in OLED devices, the scarcity and resultant cost of rare earth elements such as Ir and Pt has motivated chemists to develop organic based emitters known as thermally activated delayed fluorescence (TADF) emitters. The key requirement for TADF emitters are the small energy gap between the singlet and triplet excited states along with the ability to form a stable triplet excited state.[37] In TADF emitters, the gap between the singlet and triplet energy level are tuned to be less than 0.1 eV by selection of functional groups. This small energy gap allows mixing of triplet and singlet

state without the need for SOC and the requirement of heavy metal complexes. As a result, the triplet excited state formed during electrical excitation are converted to a singlet excited state through a process called reverse inter-system crossing (RISC) and radiatively relaxed to the ground state via fluorescence with a seemingly long lifetime. Adachi et al demonstrated the first application of TADF using the molecule 2-biphenyl-4,6-bis(12-phenylindolo[2,3-a]carbazol-11-yl)-1,3,5-triazine (PIC-TRZ) in OLEDs.[38]. The emission occurs in two different time scales in the TADF based OLEDs: prompt fluorescence (nanosecond (ns), short) and delayed fluorescence (microsecond (μs), long). Prompt fluorescence arises from the relaxation of singlet excited state originally formed along with the triplet excited state while the delayed fluorescence arise from the relaxation of singlet excited state formed after RISC process. The mechanism is also sensitive to the absolute temperature where lower temperature has been shown to deactivate the mechanism for triplet transfer to the singlet state. Although TADF emitters offer viable alternative to the visibly emitting expensive phosphorescent heavy metal complex emitters, material stability and achieving emission in the NIR are still some of the remaining challenges.

1.4.7 Exciton Blocking Layer

Due to a mismatch of energy levels between the emissive layer and the ETLs as well as the fact that the hole mobility is usually orders of magnitude higher than electron mobility in organic molecules, holes can leak from the emissive layer to electron transport layer. This often leads to loss of charge balance in the devices and ultimately reduce the electroluminescence efficiency. The leakage of holes from the emissive layer can be prevented by inserting a blocking layer with a deep HOMO level between the emissive layer and ETLs.[39, 40] The most commonly used blocking layer is bathocuproine (BCP) with HOMO level of 6.5 to 6.6.

1.5 Conventional and Inverted OLEDs

Phosphorescent and fluorescent OLEDs can be generally classified into two categories such as conventional and inverted based on the direction of the light emission with respect to the electrodes in the device architecture.

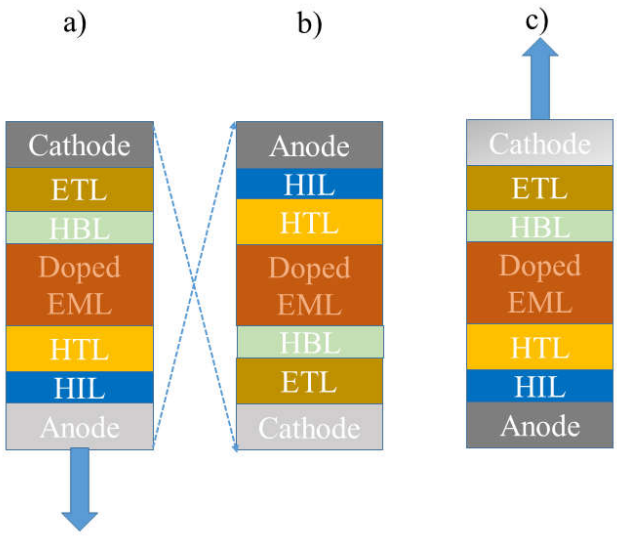

Figure 1.6 Conventional and Inverted OLEDs a) Schematics representing the conventional (bottom) vs. inverted (b) along with top emitting (c) OLEDs

Figure 1.6 display the schematics of conventional and inverted architectures used along with the top emitting OLEDs. While conventional OLEDs has the anode made of ITO is in contact with the glass substrates, inverted OLEDs has cathode in contact with the substrate. The direction of organic layers also have to be reversed in the inverted devices to efficiently inject charge carriers from the contacts to the emissive layer.

Light is isotropically generated in all directions at the point of the emitters. Accordingly, OLEDs can be designed as bottom emitting or top emitting and both require a semi-transparent electrode. In bottom emitting OLEDs, the generated light exits through the glass substrate Although the fabrication of bottom emitting OLEDs is straightforward using the established fabrication process, there are limitations of bottom emitting OLEDs. For example, bottom emitting

OLEDs suffer from poor light extraction efficiency as part of the emission is trapped as substrate modes [41],[42] and difficulty in integrating bottom emitting OLEDs into electronic circuitry that drive the operation of displays. These issues are mitigated by allowing the light to exit through the top of the devices through a semi-transparent or transparent cathode and these OLEDs are called top emitting OLEDs. Compared with bottom emitting, top emitting OLEDs offer flexibility in substrate choice such as plastics, metal foils and backplane electronics. However, the deposition of transparent electrode layer can be problematic. These electrodes are usually deposited using sputtering methods, which generate high energetic particles including sputtered atoms, and negative oxygen ions. During the process, these particles bombard and transfer their energy to the underlying layers and can cause severe damage.[43] As a result, defects and various conduction pathways arise on the devices leading to poor device yield and performance of top emitting OLEDs.[44] Nonetheless, top-emitting OLEDs with almost similar performance to bottom emitting OLEDs and even in some cases with improved efficiency have been demonstrated.[45]

1.6 Applications

OLEDs offer indispensable benefits such as tunable emission, low power consumption, ultra-thin and flexible form factors, low cost, scalability, and the ability to produce light with exceptional color rendering. In addition, OLED pixels can be easily formed compared the pixels made of LEDs (e.g. micro LEDs which are cut from single crystals and placed pixel-by-pixel). Motivated by these attractive features, OLEDs are rapidly finding application in displays such as cell phones, tablet, televisions (>55 in), wearable electronics and are being considered to use for general lighting purposes along with the others solid state lighting (SSL) technology. Figure 1.7 shows some of the example applications of OLEDs.

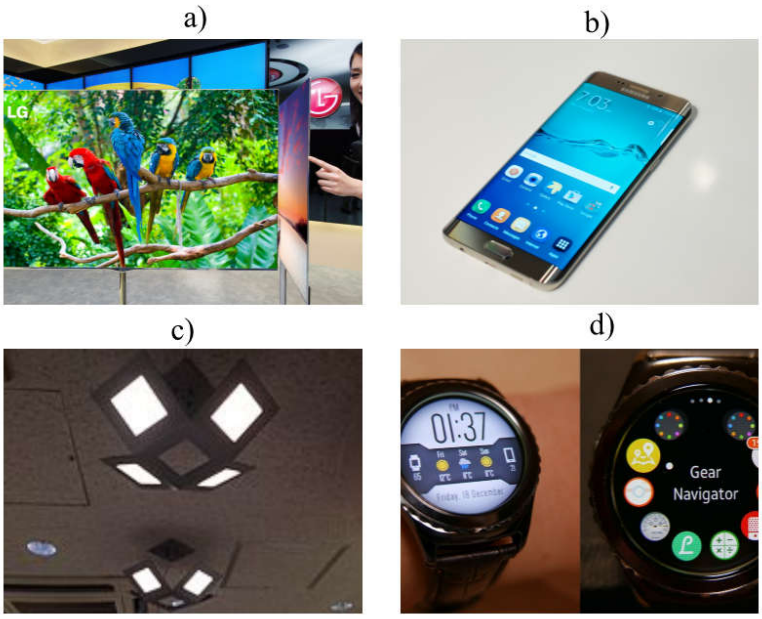

Figure 1.7 Example applications of OLEDs in a) television[46] b) cell phones[47], c) lighting[48] and d) wearable electronics[49]

Companies such as DOWDupont, Universal Display Corporation (UDC), Samsung, LG, Panasonic, Apple have all made large investments to continuously improve the performance of OLEDs to meet the specification requirement of the ever-growing consumer electronics industry and to lower the cost of the technology. OLEDs are currently being used in high-end cell phones: Samsung have been using OLEDs in their Galaxy model phones displays since 2011 and Apple just started using them in their latest iPhone X© model (supplied by Samsung). Most of the OLED materials in these devices are supplied by UDC (to Samsung). In addition, a number of wearable electronics such as Fitbit iconic©, Apple watch© and tablets such as Galaxy Tab© also using OLED based display technology. Large displays and televisions with OLEDs have also been introduced within the last decade, as they do not need to any backlight to produce light and offer thin form factors. Despite unparalleled performance of OLED displays over liquid crystal displays (LCD), the main drawback has been the higher cost associated with these displays. Thanks to the continuous technological improvement in manufacturing of OLED displays panels, the cost of 55”

inch televisions with active matrix organic light emitting diode (AMOLED) display that Samsung (model no: 55" KN55S9C) and LG (55" LG 55EA9800) introduced in 2013 with the price tag of $9,000 now sells for $1500-$3000. In the following section, we introduce the basics of the OLED display technology.

1.6.1 Displays

We first introduce the operating principle of LCDs, as they have been the dominant display technology. LCD displays consist of various parts including liquid crystals, a series of polarizer, spacer, color filters, backlight typically made of LEDs and electronics to drive the circuit. Figure 1.8 shows a simple schematic of a LCD display.

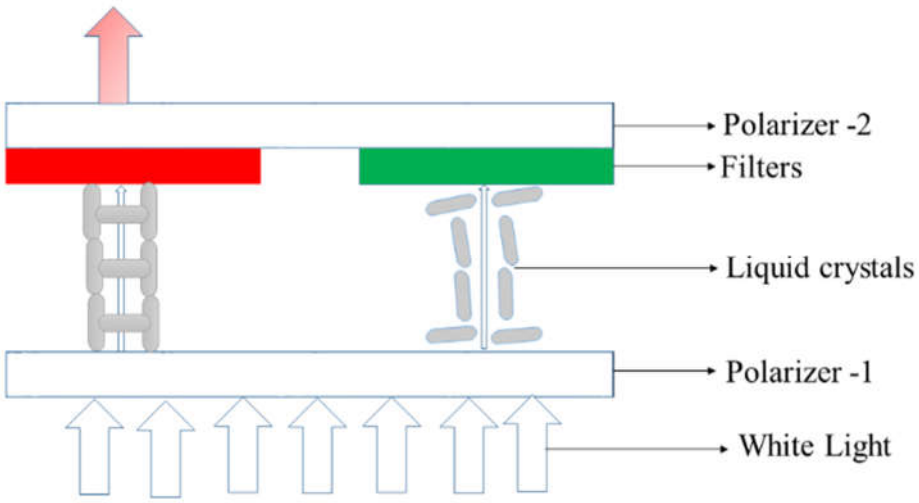

Figure 1.8 Simplified schematic demonstrating the operation of a LCD display. Liquid crystals adopt different orientation depending the applied electric field resulting in polarization and filtering of incoming white light.

Liquid crystals operate based on the twisted nematic effect. These molecules can adopt helical or untwisted structures depending on the applied electric field.[50] Each pixel consist of a layer of this liquid crystals aligned between two polarizers that are perpendicular to each other with a common white light source and color filters over each pixel. In the absence of an electric field, the liquid crystals adopt a helical structure as a result the light coming from polarizer one is

rotated. As a result, the rotated light now can pass through the second polarizer positioned orthogonal to the polarizer one resulting a bright pixel. Conversely, in the presence of an applied field, the liquid crystal adopt a linear structure and the light from polarizer one is not rotated and ultimately blocked by the second polarizer resulting in a dark pixel. By changing the applied voltage between the electrodes, one can obtain various pixel intensities in the displays.[51] Different colors such as green, blue and red can be obtained by installing color filters over each pixel.

Compared with LCDs, OLED display technologies do not require backlight as they can produce their own light at each subpixel. As a result, OLED displays offer lower power consumption, improved color rendering, thin form factor combined with the fast response time. Moroever, OLED pixels can be switched off completely resulting in a truer black and displays with essentially infinite contrast ratio. Depending on the electronic circuitry that drive the pixels, displays can be classified as passive matrix (PM) and active matrix (AM) displays

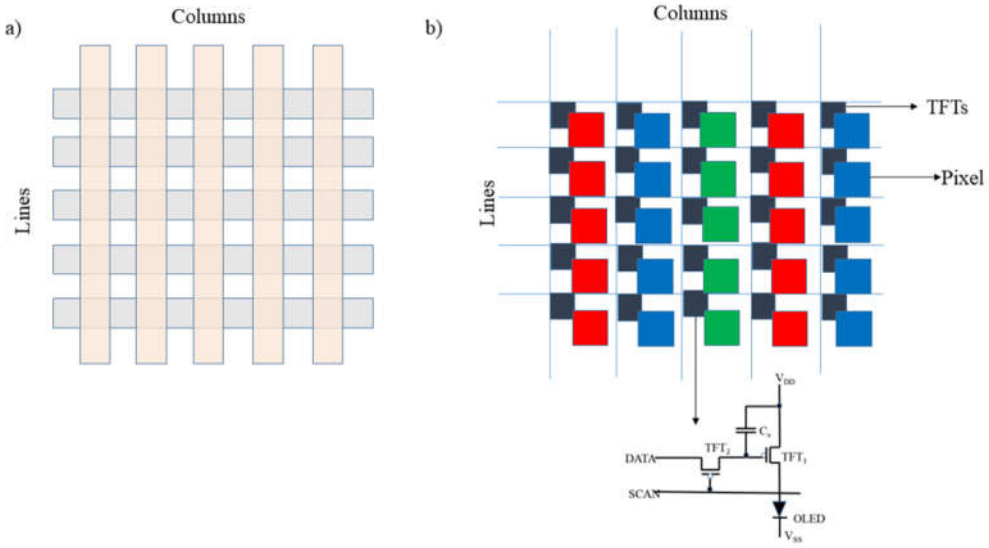

Figure 1.9 PMOLED vs. AMOLED displays PMOLED display consisting stripes of electrodes positioned perpendicular on the lines and columns b) AMOLED display made on TFTs substrates and the inset shows an example of simple electronic circuitry used to drive each OLED pixel

1.6.1.1 Passive Matrix Organic Light Emitting Diodes Displays (PMOLEDs)

PMOLED displays are fabricated by arranging anodes and cathodes in lines and columns that are perpendicular to each other as displayed in the Figure 1.9a and the intersection of the cathode and anode make up a pixel. In PMOLEDs, the line electrodes are sequentially addressed single line by line, the emission intensity of pixels in that line are controlled by the signal from the corresponding column electrode. Because of this time sequential addressing of the entire line, each pixels in that line needs to be operate at much higher brightness to compensate the work of pixels that are off in the other lines. For example, consider a display with 100 lines. To achieve panel luminance 500 cd/m^2, each pixel in the line needs to operate at 50,000 cd/m^2 to compensate the pixels that are off in the other lines. Such a high luminance cause increase power consumption due to the increased voltage and negatively impact the lifetime of OLED displays.[52] The fabrication of PMOLED display is relatively simple and they are usually used in small displays such as mp3 players. The major drawbacks of PMOLED display are slower response time and imprecise voltage control.

1.6.1.2 Active Matrix Organic Light Emitting Diodes Display (AMOLEDs)

To alleviate the higher power consumption of PMOLEDs displays, AMOLEDs displays use active matrix addressing to control each pixel in the grid using dedicated thin film transistors (TFTs). Figure 1.9b inset shows the simple electronic circuit for driving the pixel in the AMOLED display. The basic AMOLEDs circuit consist two thin film transistors (TFTs) such as TFT_1 and TFT_2 and a capacitor (C_s). While the TFT_2 control the value of the current delivered to OLEDs based on the image content, TFT_1 turn on or off the pixel in the selected row. Various materials such as amorphous Si (a-Si), poly crystalline silicon (poly-Si), single crystal Si, metal oxide have been used to fabricate TFTs. a-Si, poly-Si substrates are the most commonly used materials and

both of them are compatible with large area glass or plastic substrates. Poly-Si TFTs are usually preferred as it can deliver higher current due to the higher mobility of poly-Si and offer greater stability over a-Si TFTs.[53] The capacitor C_s holds the charge and keep the TFT_1 on until the pixel is addressed again during the next refresh cycle. This circuit allows faster and reliable control over the pixel output and used in the modern cell phone displays.[53, 54]

1.6.2 Solid State Lighting

Lighting accounts for significant portion of energy usage around the world. The U.S Energy Information Administration (EIA) estimated in 2016, residential and commercial sectors used 10 % of the total electricity for lighting.[55] Rising concerns about global warming and the desire for energy independence, propelled the development of solid state lighting (SSL) technology as it has a strong potential to reduce energy consumption.[56] Incandescent and fluorescent bulbs have been the dominant technology for decades because of their durability and low cost. While, the incandescent bulbs produce light by heating the tungsten filament using electricity, fluorescent bulbs generate light by passing electrical current through an ionized gas filled in the tubes. Owing to the extremely low efficiency, incandescent bulbs are being phased out of the market. The environmental concerns of fluorescent bulb that contains mercury and the time required to achieve full brightness accelerated the development of highly efficient, long life, and durable SSL technology. Currently, light emitting diodes (LEDs) are dominating in the solid state technology market. Commercial cool white LEDs (5700 K-CCT, CRI- 70 %) have been demonstrated with an efficiency of 160 lm /W with the price as low as $0.9/klm.[57] OLEDs have similar potential to match the LEDs performance in addition to allowing engineers to design with varied form factors. Moreover, OLEDs emit diffuse light with no glare compared to the point source such as LEDs and can installed without any additional light distribution fixtures. Companies such as OLEDWorks,

Visa Lighting, Aerelight, Acuity brands and LG displays have already released prototypes of OLED lighting fixtures that offer superior performance and improved the aesthetic appeal of the lighting environment but have yet to come down to an competitive price point.

1.7 Challenges and Strategies for Performance Improvement

OLEDs are currently the most mature organic-based electronics devices and have already been commercialized in various applications with good reported lifetimes. However, there are still remaining challenges to be addressed. For example, while the lifetime of the devices for red and green are >100,000 hrs. blue OLED lifetime and performance is a concern.[58] Currently the blue pixel on most AMOLED displays actually uses a more stable fluorescent blue emitter, which limits the overall efficiency. Additionally, the performance of phosphorescent OLEDs at higher brightness decreases much more quickly compared to their LED counterparts. Although phosphorescent OLED devices routinely achieve 100 % IQE, part of the light is trapped inside the devices due to refractive index mismatch between the organic layers and the air. Various strategies needs to be developed to improve the light coupling efficiency in OLEDs. Efforts have to be made in optimizing the manufacturing process to improve the yield, and finding the phosphorescent emitters alternative to the noble, heavy metal complexes is also necessary to reduce the cost.

1.7.1 Device Lifetime

Although OLEDs have achieved the required stability to be used in mobile phones and in televisions, considerable work needs to be done to improve the stability of OLED to be used in the solid-state lighting and to address the differential aging of three primary colors in OLEDs.[59] The differential aging of colors results in burn-in that creates a luminance difference between the adjacent pixels. As the human eye is very sensitive to contrast and color changes with the ability to distinguish just 2 % luminance differences, burn-in is a serious issue in televisions and computer

monitors.[60]. Burn-in issue in OLED televisions is largely mitigated by pixel shifting approaches. However, because computer monitors would suffer burn-in because of the large static content in the task bar, OLEDs are generally not yet recommended for this application. Performance degradation occurs while the device is in operation and typically manifests as decrease in brightness or increase in drive voltage. Three different modes of degradation have been identified in small molecule OLEDs: dark-sport degradation, catastrophic failure, and intrinsic (gradual luminance) degradation.[61] Dark spot degradation occurs at the electrode surface and decrease in luminance is due to the loss of emissive area of the device.[62] Catastrophic failure occurs at the organic layers due to the defects formed through the electrical shorts resulting in a sudden loss of some or all of the luminance as the charge leakage increases.[63] Intrinsic electrical (luminance) degradation steadily occurs during the operation of the device without any obvious change in appearance in the device area and is the most common form of degradation of OLEDs as the other two-degradation processes can effectively be avoided with proper material selection and device architecture.[64]

Various intrinsic and extrinsic factors contribute to the lifetime of the devices. For example, electrochemical stability of host materials is important. The well-studied host 4,4’-bis(N-carbazolyl)-1,1’-biphenyl (CBP) undergoes irreversible oxidation in solution at voltage above 1.8 V vs. standard calomel electrode (SCE). The cation radical can dimerize to form 3-3'biscarbazole in the solution highlighting the importance of electrochemical stability of host materials.[65]

Thermal stability of materials also important as materials with low glass transition temperature can crystalize during the operation of the devices that led to electrical shorts in the devices. In addition, materials have to be 100 % pure as the defects present in the materials can act as luminescence quenching sites or charge trapping sites in the devices.[66] In addition, device

architecture also play important role in the device lifetime. For example, if the architecture use blocking layers, charge carriers might be accumulated at the interface that cause damage to the nearby layer. For example leakage of holes to Alq_3 layer resulted formation of cationic Alq_3 species that cause severe damage to the lifetime of the devices.[67]

Extrinsic factors such as humidity, contaminant in fabricating environment, and operating conditions also play critical role in affecting the lifetime of the devices. Packaged devices show markedly improved performance over non-packaged devices as the hermetic packaging prevents the reactions between the contaminants such as water and oxygen and the organic layers at higher electric fields.[62] Nevertheless, all state of art OLED devices have to be encapsulated to preserve their performance metrics.

1.7.2 External Quantum Efficiency Roll off

The external quantum efficiency of OLEDs tends to decrease monotonically at higher current densities (high brightness) and is known as EQE roll off. This causes an increase in power consumption and the higher current can accelerate the device deterioration. Various factors contribute to the EQE roll off in the devices.

In OLEDs, excitons and charge carriers undergo various interactions during the device operation. When charge carriers move in weakly bonded organic semiconductors, it polarizes the local environment that lead to local structural distortions and the combination of charge carrier along with the distortion is referred as polaron that can also interact with the excitons. Common exciton interactions including singlet-singlet annihilation, singlet-polaron annihilation (SPA), singlet-triplet annihilation (STA), triplet-triplet annihilation (TTA), triplet-polaron annihilation (TPA). These exciton interactions increase non-linearly with exciton density resulting nonlinear dependency of EQE on current density. In addition, these interactions can potentially lead to

molecular degradation by depositing additional energy into molecular bonds. Typically in phosphorescent OLEDs, TTA and TPA processes are responsible for EQE roll off.[68]

1.7.2.1 Triplet-Triplet Annihilation (TTA)

Triplet-Triplet annihilation (TTA) is an important energy transfer mechanism between two triplets excitons formed during the EL process that reduces the overall EL. This is described mechanistically as:

$$T + T \rightarrow S^n + S_0 \rightarrow S_1 + S_o\,, \tag{1.2}$$

$$T + T \rightarrow T^n + S_0 \rightarrow T + S_0\,, \tag{1.3}$$

where, *S*, *T*, are the singlet, triplet state , and S^n, T^n, are the higher excited singlet, triplet state also known as hot exited states, S_0 is the ground state. As shown in the above reaction, one triplet is lost during the TTA process. At higher current densities, the TTA process increases in rate as the triplet concentration increases ($[T]^2$ dependence), which will reduce the triplet density in the guest molecules. As a result, the efficiency decreases at higher current. Since the rate of TTA scales with the triplet exciton density, various methods have been developed to reduce the exciton density.[68]

1.7.2.2 Triplet-Polaron Annihilation (TPA)

TPA involves interaction of a triplet exciton with a polaron. This process will then create excited charged molecule and a ground state of molecule as described in the equation 1.4,

$$T + p \rightarrow p^n + S_0 \rightarrow p + S_0 + \tilde{\nu}\,, \tag{1.4}$$

where, p and p^n are the ground state polaron and higher excited polaron states. $\tilde{\nu}$ is a phonon resulting from the relaxation of highest excited polaron to the ground state. Exciton annihilation reactions discussed above scales with exciton density, carrier density, and lifetime of the excitons. Increasing the width of exciton recombination zone or decreasing the life time of excitons has been

shown to improve the high brightness performance of OLEDs.[69] While the width of exciton recombination zone can be modified by adopting different emissive layer configurations such as single emissive layer, double emissive layer or mixed emissive layer,[70] exciton lifetime of the emitter can be altered by adopting various chemical design principles. For example, metal complexes with high zero field splitting shown to have lower exciton lifetime.[71] Exciton lifetime in OLEDs can also be altered by placing emitter in a strong optical cavity or close to the cathodes.[72]

1.7.3 Outcoupling

Optics plays a critical role in OLEDs. During the light emission process, a fraction of light is trapped inside the devices. This is due to the difference in refractive index between the individual organic layers in the device stack. In addition, refractive index difference between the organic layer stack and the ambient air also contribute to the outcoupling in the OLEDs. A simple model shows the maximum forward emitted light extraction efficiency for simple waveguide configurations can be calculated as,

$$\eta_{out} = \frac{1}{2n^2}, \tag{1.5}$$

For organic semiconductor with n = 1.6-1.8, the maximum outcoupling efficiency will be 15-18 %. The majority of the emitted light then gets wasted through coupling with substrate (waveguiding) and surface plasmon polaritons (SPPs) modes which convert light to heat.[41] The contribution of various optical modes in OLEDs fabricated with Alq_3, for example, are shown in Figure.1.10.

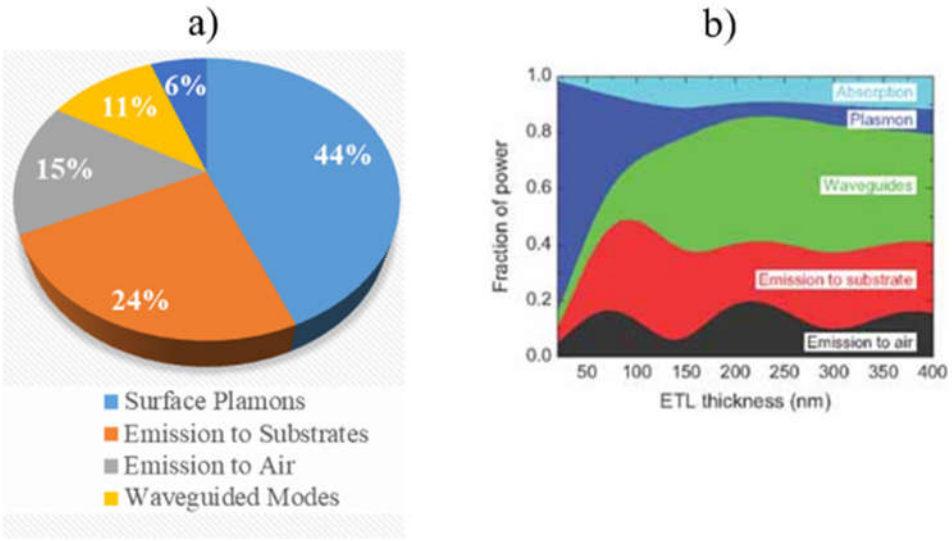

Figure 1.10 Various outcoupling modes in OLEDs a) percentage of optical power coupled with various channels estimated for an archetypical OLED fabricated using Alq_3.b) Dependence of various outcoupling modes vs. thickness of the ETL layer.[41]

As shown in the Figure 1.10, over 50 % light is trapped in the waveguide and surface plasmon modes and only 15 % light is emitted to air demonstrating the challenges in light extraction in OLEDs.[73] To reduce substrate modes, index matched microscopic lens can be placed on bottom emitting OLEDs to extract the light trapped in the substrate modes.[74] In addition, scattering particles, mechanical roughening of the glass substrates can also be used externally to the OLEDs to scatter the light that would otherwise trapped due to total internal reflection between the substrate and air.[75, 76] However, these techniques will affect the unique form factors of OLEDs and is not suitable for the large area devices and alternative methods needs to be developed. One way to extract more light from the conventional devices is to use high refractive index (HI) substrates so that the mismatch between the organic layers and substrates is minimized resulting more generated light reaching the substrates.[77]

Further improvements in EQE were obtained by incorporating periodic outcoupling structure on the HI substrate which resulted record high EQE of 40 % in the devices.[78, 79] However, these methods increase the production cost and show extraction efficiency enhancement

only at certain viewing angles. To circumvent this issue, low index grids have been embedded into the organic layer and attached microlenses, which doubled the outcoupling efficiency over conventional devices.[80]

Since the loss through SPPs are high in OLEDs, various methods adopted to minimize the coupling to SPPs. SPPs can be defined as longitudinal P polarized waves travelling at the interface of dielectric layer and cathodes with the optical field decaying exponentially into the adjacent media.[81] Methods have been focused to scatter the SPPs generated by installing grating structure with a periodic modulation of refractive indexes to scatter SPPs back to the substrates.[82] Alternatively, one can minimize the excitation of SPPs in OLEDs as the coupling between the SPPs and the emitting dipole is depending on the distance and orientation of the dipoles.[41] According to wave optics theory, the horizontally oriented dipoles couples weakly with the SPPs, so the emitter with horizontal orientation should produce high light extraction efficiency.[83] In addition, devices that employ emitters with horizontal dipole orientation can enable higher EQE because of the increased forward emitted light in this orientation of the emitters.[83, 84]

Chapter 2 Introduction to Organic Semiconductors

In this chapter, the physics behind the optical and electronic properties of organic semiconductor are reviewed. A brief discussion of molecular orbitals and electronic state formation in the organic semiconductor will be given. This will be followed by a review of various inter and intra molecular energy transfer processes involved in the organic semiconductors. Finally, a discussion about various steps of electroluminescence processes that are essential for the operation of OLED devices will be explained.

Organic semiconductors are low-cost, mechanically flexible materials consisting of conjugated organic molecules or polymers that display properties such as absorption and emission of light and electrical conductivity. In addition, these properties can be tuned by molecular design. Organic semiconductors generally have low dielectric constants (typically ε_r <4) which determine the polarizability of the materials. Upon optical or electrical excitation, the electron and holes form a neutrally charged quasi particle called an exciton. An exciton typically exhibits a binding energy (i.e., energy required to separate the excitons into free charge carriers) of about 0.5 to 1.0 eV. Excitons form due to the strong columbic interaction between holes and electrons in the low dielectric constant environment in organic semiconductors.[85] However, light absorption or electrical excitation creates free charge carriers in inorganic semiconductors as the columbic interaction is weak between the electrons and holes in the high dielectric constants (example: Si, ε_r =11) materials. Excitons are responsible for many optical properties in organic semiconductors and are essential to the operation of organic opto-electronic devices. In OLED applications, the presence of excitons actually aids in recombination and luminescence processes. To understand the origin of optical and electrical properties in the organic semiconductor, a brief discussion about molecular structure and bonding in organic molecules is necessary.

2.1 Molecular Orbitals

Orbitals are regions in space where electrons are most likely to be found in an atom. There are four different type of orbitals, namely s, p, d, and f. Since organic semiconductors primarily consist of carbon and hydrogen, we limit our discussion to the s and p orbitals. As can be seen in Figure 2.1, s orbitals are spherically symmetric around the nucleus, and p orbitals are dumbbell shaped, having three possible orientations on the *x*, *y*, and *z*-axis. Elemental carbon has six electrons in its ground state: two are in the 1s orbital, two are in the 2s orbital, and the remaining two are split between the $2p_x$ and $2p_y$ orbitals, leaving the $2p_z$ orbital unoccupied ($1s^2 2s^2 2p_x^1 2p_y^1 2p_z^0$). When two carbon atoms approach one another, the atomic orbitals in carbon combine and form hybridized orbitals as the hybridized orbitals are more energetically favorable than the individual atomic orbitals.

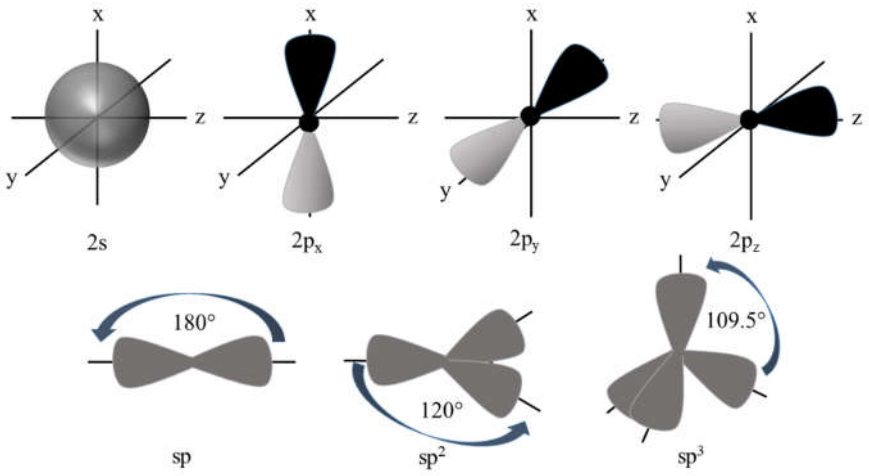

Figure 2.1 Orbital hybridization in carbon. Atomic 2s and 2p orbitals and the resulting sp, sp^2, and sp^3 hybridized orbitals in carbon.

In sp hybridization, one 2s orbital and one 2p orbital mixes to form two sp hybridized orbitals. These sp hybridized orbitals are situated 180° to each other, allowing the formation of linear molecules. sp^2 hybridization occurs between the 2s orbital and two of the 2p orbitals,

resulting three sp^2 hybridized orbitals oriented 120° apart. sp^3 hybridized orbitals form when one 2s orbital mixes with three of the 2p orbitals, resulting in four sp^3 hybrid orbitals in a tetrahedral shape with 109.5° between the orbitals. (Figure 2.1) The type of hybridization and the remaining 2p orbitals in carbon determine the number of bonds it can form with the neighbors.

Consider the molecule ethene (C_2H_4): each carbon atom has three $2sp^2$ hybrid orbitals in a plane with one remaining electron in the $2p_z$ orbital lying orthogonal to the plane. An illustration of molecular orbital formation in ethene is shown in the Figure 2.2. When two carbon atoms come together, one of the $2sp^2$ electrons is shared with the other carbon and forms a molecular orbital called σ orbital. The corresponding bond between these carbon atoms is called a σ-bond. Similarly, the other two sp^2 orbitals in carbon can make a σ bond with two 1s hydrogen atoms. The remaining electron in $2p_z$ orbital is shared between the two carbon atoms, forming π orbitals. The electrons in π orbitals will have a spatial probability density above and below the molecular axis, and the bond between the $2p_z$ shared electron is known as π-bond. These π bonds are responsible for making conjugated molecules (alternating single and double bonds) and imparting semiconducting properties to carbon based organic semiconductors.[86]

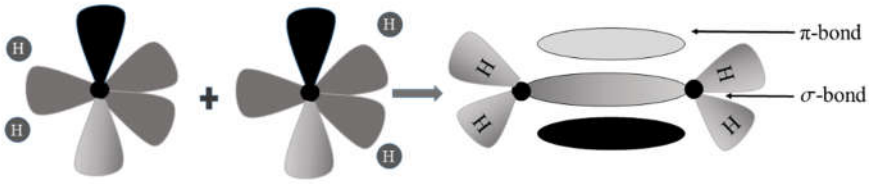

Figure 2.2 Formation of molecular orbitals in ethene The molecular σ and π orbital formation in ethene from the overlap of two sp^2 hybridized orbitals and the non-hybridized two p_z orbitals respectively.

To understand the origin of optical and electrical process in organic semiconductors, we need to understand the concept of electronic states in the organic molecules. The electronic states

are described by wave functions (Ψ_i), which can be obtained by solving time-independent Schrödinger equation 2.1

$$\mathcal{H}\,\Psi_i = E_i\,\Psi_i\,, \tag{2.1}$$

$\mathcal{H}$ denotes the Hamiltonian operator, which corresponds to the kinetic and potential energies of nuclei and electrons as well as their interaction. To solve Schrödinger equations for a many electron system, several approximations must be utilized. First, the Frank-Condon approximation states that the motion of atomic nuclei and the electron can be separated as the lighter electrons responds instantaneously for electromagnetic radiation compared to the heavier nucleus. Hence the wave function Ψ can be written as electronic part($\phi_i^{\vec{R}}(\vec{r})$) and a nuclear (vibrational) part χ_i $(\overrightarrow{R})$.

$$\Psi_i = \phi_i^{\vec{R}}(\vec{r}).\,\chi i\,(\overrightarrow{R}), \tag{2.2}$$

As a result, the total energy obtained from solving Schrodinger equation can be split into electronic and vibrational contributions as,

$$E_i = E_i^{el} + E_i^{Vib}\,, \tag{2.3}$$

To calculate the energy of many electrons present in the molecular orbitals and their spatial probability of electrons, further approximation were made in which the molecular orbitals can be expressed as a linear combination of atomic orbitals (LCAO). For example, when two hydrogen atoms with atomic orbitals ϕ_a, ϕ_b come closer and form molecular hydrogen, the resulting molecular σ-orbital can be represented by $\Psi_+ = c_1\phi_a + c_2\phi_b$ where c_1 and c_2 are positive integers. This combination can be thought of constructive inference between the two electronic wave functions that results enhanced charge density between the atomic nuclei in bonding orbitals. Similarly, molecular anti-bonding orbital σ*-orbital can be written $\Psi_- = c_1\phi_a - c_2\phi_b$ representing

destructive interference between the two electronic wave functions with a reduction of the charge density between the two nuclei leading to anti bonding character.[87] The coefficients c_1 and c_2 can be calculated by minimizing the total energy of the system. In the example of ethene (C_2H_4), the formation of these molecular orbitals (MO) between two atomic orbitals and their energetic distribution is illustrated in the Figure 2.3.

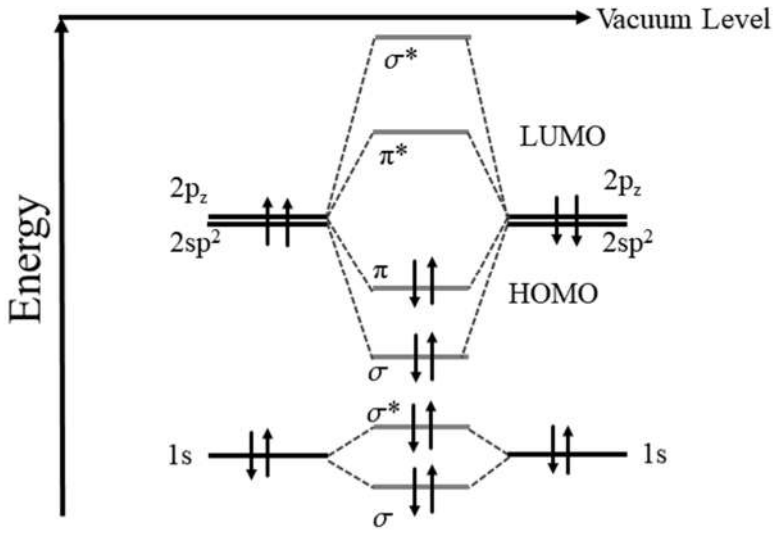

Figure 2.3 Energetic distribution of molecular orbitals Simple energy distribution diagram illustrating the formation of HOMO and LUMO in ethene resulting from the splitting of hybridized atomic carbon orbitals.

When two carbon sp^2 hybridized atoms come closer for the formation of ethene, the two electrons from the each sp^2 hybridized orbitals will occupy the σ-molecular orbitals leaving the high lying σ*molecular orbitals empty. This causes a strong attractive interaction between the nucleuses resulting a strong σ bond between these atoms. As can be seen from the Figure 2.3, the splitting between the σ-σ*orbitals is large due to the significant overlap of charge density between these orbitals. Compared with sp^2 hybridized orbitals, the interaction between $2p_z$ orbitals is very weak as they located in some distance from nuclei and the resonance interaction of electrons in the π orbital is small. This results small splitting between the π and π* orbitals.[86]. The two electrons of the each $2p_z$ orbitals occupy the π molecular orbital leaving π* orbital empty. The molecular

orbital with high energy that are completely occupied (π-orbital in ethylene) is called highest occupied molecular orbital (HOMO) and the next high energy molecular orbital that is empty (π* orbital) is called lowest unoccupied molecular orbital (LUMO), together they referred as frontier orbitals of the molecules. According to Koopmans theorem, the HOMO energy is equal to the negative of the first ionization energy of a molecule.[88] The gap between the HOMO and LUMO is also known as bandgap responsible for the optical properties such as absorption and emission cutoffs in organic semiconductors. Molecules that have larger size with extended conjugation will have lower band gap than the smaller molecules [89] as the conjugation results in additional orbital energy splitting.

2.2 Excitons

Excitons can be classified mainly based on their Bohr-radius as Frenkel, Wannier-Mott, and charge transfer excitons. Frenkel excitons are typically formed in organic semiconductor with low dielectric constant and tend to reside on a single molecule with a substantial binding energy of 0.1 to 1 eV.[90] In contrast, Wannier-Mott excitons are formed in semiconductors with high dielectric constant. Their radius is larger than the lattice spacing with a typical binding energy of 0.01 eV.[91] Another class of excitons that are important in the organic semiconductors is charge transfer excitons in which the hole and electron occupy the neighboring molecule.[92]

2.2.1 Singlet vs. Triplet Excitons

Excitons can further be classified based on their spin states. In organic molecules, these include singlet and triplet excitons depending on their total spin angular momentum. Electrons can have spin quantum number of ½ with different z-component of angular momentum $m_s = \pm ½$ that refer to the spin up (↑) and spin down (↓) orientations. According to Pauli's exclusion principle, no two electrons can occupy the same orbitals and they should have different quantum numbers

namely the principal number (n), the orbital number (l), the magnetic number (m_l), and the magnetic spin number (m_s). Most of the organic molecules will have a ground state with a single energy level consisting of two electrons that are paired (↑↓). When the electron is excited from the ground state upon optical or electrical excitation, the excited electron can have two different orientation of spin imparting different energies to the excited state of molecules. If the excited electron have the same spin orientation (antiparallel) as it was in ground state then the excited state is called singlet excited state. In contrast, if the excited electron can have same spin orientation of other unpaired electron (parallel) then the excited state is called as triplet state. Figure 2.4 shows the simple representation of excited states based on spin of the occupied electrons. The number of degenerate levels which defer by spin-orbit interaction energy, also known as multiplicity (M) can be obtained from total spin angular momentum (S^T) as (M=2S^T+1). Electron that have antiparallel and parallel spin states will have total spin (S^T= 0) and parallel spin states (S^T =1) occupy singlet (M=1) and triplet states (M=3) respectively. Compared with singlet excited state, the triplet excited state will have lower energy as the spin parallel electrons will occupy different orbitals resulting lower electron-electron repulsion in the excited state.

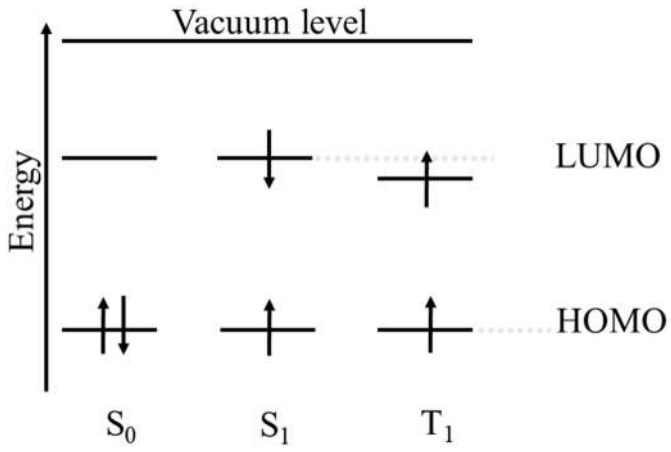

Figure 2.4 Singlet and triplet excited states. Formation of excited states in the organic semiconductor ground state *(S_0)* consists two electrons with opposite spins, excited singlet state

(S_1) consists electrons with antiparallel spins and excited triplet state (T_1) consists electrons with parallel spins. (Arrows indicates the spin of an electron)

2.3 Potential Energy Curves

Potential energy curves are useful to understand the optical transition involved between the different energy levels. These curves are obtained by calculating the energy of the molecules at different nuclear position using Schrodinger's equation. The eigenvalues for the electronic and vibrational wave functions associated with the molecular ground state (S_0) and excited state (S_1) are plotted separately for each normal mode coordinate (Q_i) of a molecule in the Figure 2.5. At very small distance between nuclei, repulsive interaction due to strong overlap of atomic orbitals dominates and at longer distance, the resonance energy is weakened and a minimum is formed. Note the vibrational energy is $(n_i+(1/2))\hbar\omega$, where n_i represent the number excited quanta numbered as 0,1,2 is obtained by assuming the atoms in the molecule as a harmonic oscillators.[87] Vibrational energy is typically given in wavenumbers ($\tilde{\nu}$) with the unit of cm^{-1}.

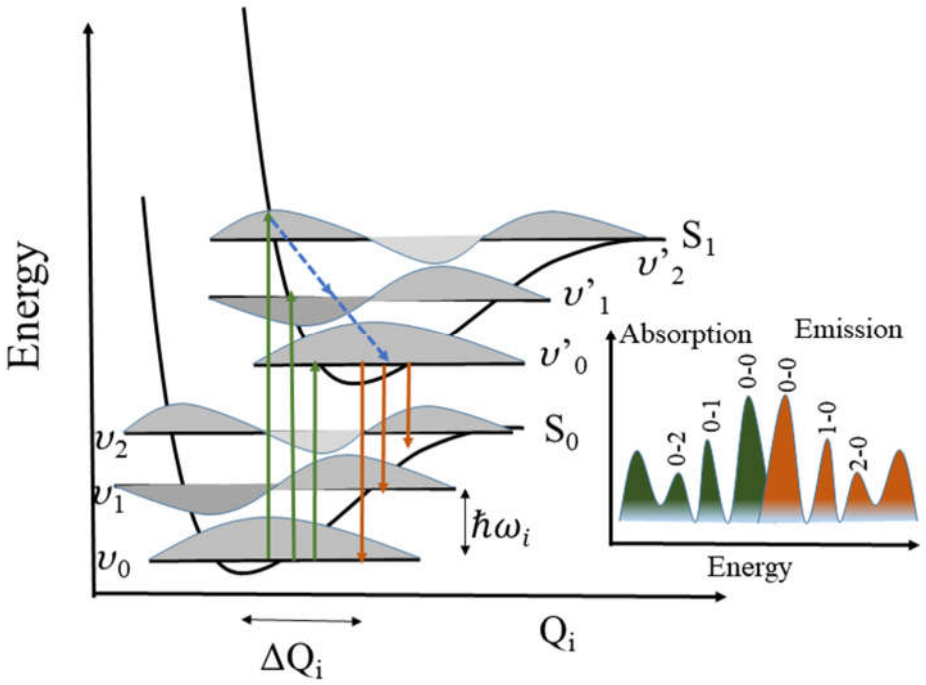

Figure 2.5 Potential energy curves Potential energy of molecules as a function of displacement in normal mode coordinate Q_i. Electronic (S_0, S_1) and vibrational levels (v =0, 1, 2) of the ground and excited state of a molecule (v'=0, 1, 2) and optical transitions such as absorption (green), emission (orange). Example of absorption and emission spectra showing a difference between the absorption maxima (0-0) and emission maxima (0-0) due to Kasha's rule (blue) (inset).

2.3.1 Jablonski Diagram

Jablonski diagram illustrates (Figure 2.6) the different optical transitions that occur between the energy states of a molecule. At room temperature, the majority of the molecules will be in the ground state with two electrons paired with opposite spin orientation (S_0).[93] During an optical excitation, ground state electrons gain energy from the photons and reach the vibrational mode of higher excited singlet state (S_2 *or* S_3). Subsequently, the electron in the higher excited state relax to the lowest singlet excited state (S_1) via a non-radiative process called internal conversion (IC) and release the excess energy in the form of phonons. The excited state electron will relax back to the ground state or undergo intersystem crossing (ISC) to the triplet excited state. However, ISC requires spin flip and hence is very slow unless there is a heavy metal present or certain degrees of symmetry (e.g. with C_{60}). According to Kasha's rule, the relaxation always

occurs from the first singlet and triplet manifold states to the ground state.[94] While the emission from the relaxation of singlet excited state to ground state is called fluorescence, emission from the triplet excited state to ground state is called phosphorescence.

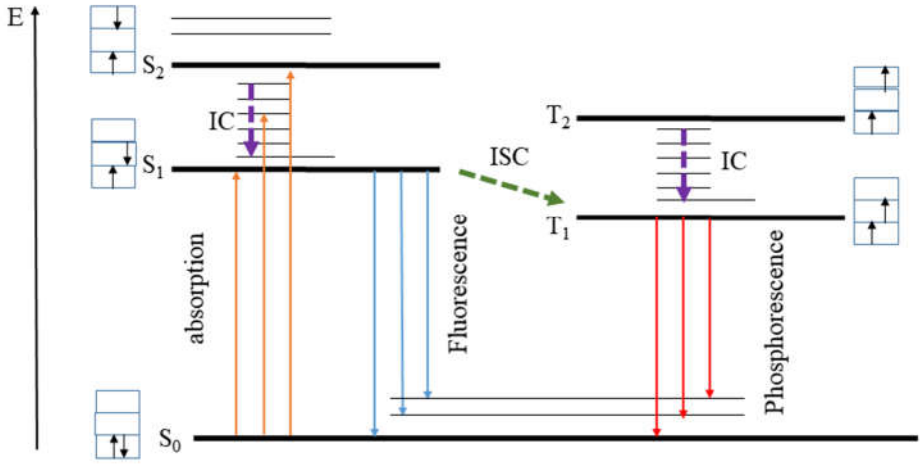

Figure 2.6 Simplified Jablonski diagram Representing optical transition between intramolecular energy states. Optical absorption (orange) always results the formation of singlet excited states S_1 and S_2. Relaxation of singlet excited state to ground state results fluorescence (blue) and relaxation of excited triplet state to ground state results phosphorescence (red). Internal conversion (IC) (dotted purple) is a non-radiative process in which electrons relax from the highest excited state to lowest excited state and inter system crossing (ISC) occurs between the singlet and triplet excited states in the phosphorescent emitters (dotted green)

Since the dipole moment operator is symmetric under particle exchange, optical transitions only occur between wave functions of similar spatial symmetry. This implies that the spin states must also have same symmetry. As a result, the transition between singlet to singlet and triplet to triplet are only allowed and relaxation of triplet state to the ground state is forbidden and very weak. However, in phosphorescent emitters containing of heavy noble metal complexes have strong spin orbital coupling that enhance the ISC rate and mix the singlet and triple excited states thus allow the relaxation of triplet state to the singlet ground state.[95] In fluorescent emitters, emission is primarily due to the relaxation of singlet excited state to the ground state. The radiative

relaxation of triplet state is outcompeted by the non-radiative processes unless there is a high degree of symmetry and the triplet states are considered as "dark" states in fluorescent emitters.[96]

2.3.2 Photoluminescence Quantum Yield

Photoluminescence quantum yield (PLQY) is a useful metric to determine the efficiency of photoluminescence. PLQY is the ratio of number of photons emitted to the number of photons absorbed by the fluorophore or phosphor and is related to the ratio of radiative decay rate (K_{r}) to the total decay rate that includes radiative and non-radiative rate (K_{nr}) of an excited state (equation 2.4)

$$\phi_{PL} = \frac{\mathrm{K}_r}{\mathrm{K_r} + \Sigma \mathrm{K}_{nr}} = \tau \mathrm{K}_r \,, \tag{2.4}$$

The intrinsic lifetime (τ) can be defined as $\frac{1}{K_r + K_{nr}}$, typically fluorescence process exhibits a lifetime of 10^{-9}-10^{-7} s and phosphorescence process shows lifetime in 10^{-4}-10^{-1}s.

2.3.3 Selection Rules

Selection rules determine the probability of optical and electrical transitions between the different states of the molecules. According to Laporte rule, the integral $< \Psi_{el,f} | e\hat{r} | \Psi_{el,i} >$ where $\Psi_{el,f}\ and\ ,\ \Psi_{el,i}$ is the final and initial state and $e\hat{r}$ is the dipole operator results non zero values only when the transition happens between the states with different parities (odd or even). If the two states share the same parity then the integral would vanish because the dipole operator has odd parity under spatial inversion and the transition is forbidden. For example, s-s and p-p transitions are not allowed.[93] The intensity of those allowed transition is depending on the orbitals overlap between the electronic states. As a results the rate of transitions between orbitals that are centered

in the same part of molecules (π-π*) is higher than the orbitals that occupy different part of molecules (example n- π *).[86]

While the intensity of optical transition is controlled by the electronic factor, vibrational factor determine the shape of the absorption and emission spectrum of molecules. According to the vibrational selection rules, vibrational transition are allowed only if the excited vibrational state have the same symmetry of transition moment operator.[97] Similar to electronic transitions, the intensity of vibrational transition between the ground state ($v = 0$) and excited state ($v' = 1$) depends on the vibrational wave functions overlap between the states. According to Frank Condon principle, the nuclei responds slow to the oscillating dipole of electromagnetic radiation and hence vibrational transition are usually shown as vertical transitions in the Figure 2.5.[98]

2.4 Energy Transfer

In addition to intramolecular transitions, energy transfer can occur between different molecules via radiative and non-radiative processes.

2.4.1 Trivial Energy Transfer

Cascade transfer is an example of radiative transfer process between the molecules. This process essentially occurs in two steps, during the first step, a donor molecule (D) in the excited state (D^*) gives off the excess energy in the form of photons and relax to the ground state as described in equation 2.5,

$$D^* \rightarrow D + h\upsilon\,, \tag{2.5}$$

In the second step (equation 2.6), the photons excite the acceptor molecule (A) from the ground state to the highest energy state (A^*)

$$A + h\upsilon \rightarrow A^*\,, \tag{2.6}$$

The efficiency of this type of energy transfer is dictated by the PL quantum efficiency of the donor and the overlap of photoluminescence of donor and absorption cross section of the acceptor.[99]

2.4.2 Förster Resonance Energy transfer (FRET)

Förster explained that energy could be transferred through overlapping dipole fields between the donor and acceptor molecules. (Figure 2.7) The rate of this energy transfer (k_F) is described in the equation 2.7 and is dependent on three factors: the distance between the donor and emitter, the overlap of absorption and emission spectrum of acceptor and donor respectively and the orientation of donor and acceptor dipole moments.[100]

$$k_F = \frac{1}{\tau}\left(\frac{R_0}{r}\right)^6, \tag{2.7}$$

where, τ is the exciton lifetime, r is the distance between the donor and emitter and R_0 is characteristic Förster radius that is defined as the distance that gives an energy transfer efficiency of 50%. The Förster radius can be related to measurable properties as:

$${R_0}^6 = \frac{9\eta_{PL}\kappa^2}{128\pi^5 n^4}\int \lambda^4 F_D[\lambda]\,\sigma_A[\lambda]\,d\lambda, \tag{2.8}$$

where, η_{PL} is the photoluminescence efficiency of the donor, κ is the dipole orientation factor, n is the index of refraction of the medium between the donor and acceptor, λ is the wavelength, F_D is the area normalized donor emission, σ_A is absorption cross section area of acceptor. It is important to note that the Förster theory assumed point dipoles and explained energy transfer between point chromophores. In condensed phase systems with closely packed donor and acceptor, the transfer rate vary r^{-2}.[101]

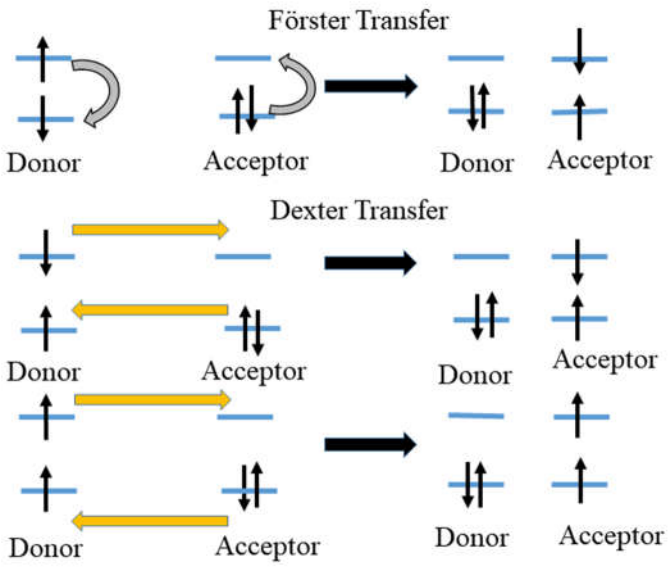

Figure 2.7 Förster and Dexter Energy Transfer Schematic illustration of Förster energy transfer mediated by dipoles and Dexter transfer where the electrons are simultaneously exchanged between adjacent molecules. While Förster transfer is only allowed for single-singlet transfer, Dexter transfer process is allowed for both singlets and triplets.

2.4.3 Dexter Energy Transfer

Dexter provided an alternative mechanism for the energy transfer mediated by quantum mechanical carrier exchange interactions. (Figure 2.7) During this process, electrons are exchanged from the excited state of the donor to the acceptor and it requires strong overlap of the molecular orbitals between the donor and acceptor. As a result, Dexter transfer is efficient only over a short range between 1-5nm compared with Förster transfer mechanism.[102] The rate constant (k_D) for the Dexter transfer can be calculated using the equation 2.9. It shows that the rate constant decrease exponentially (e^{-R}) as the separation between the donor and acceptor increases.[99]

$$k_D = K e^{-2R_{D-A}/\check{R}} \int F_D[\lambda]\sigma_A[\lambda]d\lambda , \quad (2.9)$$

where, K is an experimental factor and is related to the specific orbital interaction and $R_{D\text{-}A}$ is donor –acceptor separation and $\check{R}$ is excited state orbital radius.

2.5 Electroluminescence

Electroluminescence is the underlying mechanism for light emission in organic light emitting diodes. Since EL involves multiple steps such as charge injection from the metal to the organic semiconductor, charge transport, exciton formation, and relaxation, careful optimization of each step is required to achieve high electroluminescence efficiency.

2.5.1 Charge Injection

Understanding how charges are injected and transported into the organic semiconductors from the electrodes is key for fabricating efficient organic electronic devices such as OLEDs, OFETs and solar cells. It is particularly important for lower drive voltages. First, we review the charge injection mechanisms involved in the inorganic semiconductors. Charge injection from the Fermi level of the metals to an inorganic semiconductor is explained by well-established theories: Richardson-Schottky injection mechanism in which thermal energy allow the electrons to inject from the Fermi level of metals to semiconductor.[103] The injected current density (J) can be obtained using the equation 2.10,

$$J = A^{*}T^{2}e^{\left(\frac{-\Delta V}{kT}\right)}\left(e^{\left(\frac{eV}{nkT}\right)} - 1\right), \tag{2.10}$$

where A^{*} is the effective Richardson constant, ΔV is the height of the barrier to injection e is the elementary charge, V is the voltage across the diode, n is the ideality factor, k is the Boltzmann constant, and T is the temperature of the junction. The charge carriers then travel across the electrostatic potential originated from the image charge and the applied electric field. For this mechanism, the current density show a Arrhenius type dependence with temperature ($\ln J \propto T$)

and Poole-Frenkel type dependence on field ($\ln J \alpha \sqrt{F}$).[104] Alternatively, Fowler-Nordheim proposed an another mechanism by ignoring the image potential at the contacts and allowing the electrons to tunnel through a interfacial energy barrier between the metal and semiconductor under applied bias.[105]

Experimental studies showed that the injection current in organic solids weakly follows the temperature and applied bias dependence expected from the Richardson-Schottky injection model. In addition, Fowler-Nordheim mechanism also failed to explain the charge injection in organic semiconductors. Measuring barrier height between the metal and organic solids is not as straightforward as the formation of interfacial dipoles specific to the metal and organic semiconductors tends to pin the Fermi level.[106] Organic semiconductors exhibit Gaussian distribution of density of states. Charge injection from the metal to organic semiconductor occurs via a hybrid process which involves thermally assisted tunneling into the lowest energy density of states.[107]

2.5.2 Charge Transport

Electronic coupling in organic semiconductors are much weaker due to the weak van der Waals forces between the molecules. As a result, charge transport cannot typically be explained based on band transport observed in inorganic semiconductor but instead transport can be described by hopping processes in which charge carrier jump between sites.[108] Compared to inorganic semiconductors with the mobilities in the range of 10^3 cm^2 V/s , amorphous organic solids have mobilities only in the range of 10^{-4} to 10^{-7} cm^2 V/s due to the weak electronic coupling and disorder present in the organic semiconductor. However, crystalline organic semiconductor such as 2,6-diphenylanthracene (DPA) show mobility up to 34 cm^2 V/s and a well aligned polymer can show mobility up to 50 cm^2 V/s.[109] Lower mobilities leads to charge buildups at the contacts

and charge transport in organic semiconductor is then explained based on the space charge limited current theory.[110]

Current density (J) as a function of applied bias (V) can be related using Mott-Gourney equation 2.11,[111]

$$J = \frac{9\varepsilon_0 \varepsilon_r \mu V^2}{8d^3}, \tag{2.11}$$

where, ε_0 is permittivity in vacuum, ε_r is relative permittivity μ is the charge carrier mobility and d is the thickness. Mott-Gourney equation is derived to describe the transport of single carriers with drift velocity. In addition, this law is valid for materials without traps as charges trapped can contribute to additional space charge density.[112]

In organic semiconductors, formation of charge traps, which hinder the charge transport in the organic optoelectronic devices, is often unavoidable. Traps can be thought of as unoccupied electronic states within the bandgap. They exhibit exponential energy distribution ($N_t(E)$) and arise from the structural defect, degradation of organic semiconductors. These trap states lower the charge carrier mobility which leads to low current density in the devices. The trap charge current density is then related to voltage as, [110, 113, 114]

$$J = \frac{N_{eff}\, e\, \mu}{H^l} \left(\frac{\varepsilon_0 \varepsilon_r\, l}{e\, l+1}\right)^l \left(\frac{2l+1}{l+1}\right)^{l+1} \frac{V^{l+1}}{d^{2l+1}}, \tag{2.12}$$

where N_{eff} refers effective density of states, e is the electronic charge, μ is mobility, ε_0 permittivity in vacuum, ε_r dielectric constant of organic semiconductor, V is the applied voltage, H refers to total concentration of traps and $l = T_c/T$, where T_c refers the measure of steepness of the trap state density distribution and d is the thickness of the thin film.

2.5.3 Recombination

Recombination of hole and electrons is the essential process involved in the operation of OLEDs. Recombination of electrons and holes that are moving via hopping mechanism in the disordered, trap free organic semiconductors can be explained by Langevin theory.[115] Rate of recombination k_L can be described using the rate constant (γ) as

$$k_L = \frac{dn}{dt} = \frac{dp}{dt} = -\gamma np\,, \tag{2.13}$$

where *n, p* are electron and hole concentration. Langevin rate constant (Equation 2.14) for bimolecular recombination of holes and electrons can be written in terms of mobilities of holes (μ_+) and electrons (μ_-) as,

$$\gamma = \frac{e}{\varepsilon_0 \varepsilon_r}(\mu_+ + \mu_-)\,, \tag{2.14}$$

The trap assisted recombination (TAR) model can be used to explain the recombination in organic semiconductor with large trap densities. This was originally developed for indirect semiconductor by Shockley, Read, and Hall (SRH).[116, 117] There are four basic processes involved in TAR. First, a trap captures an electron from the conduction band and the rate of this process is governed by capture coefficient (C_n). Subsequently, the captured electron can be excited back to conduction band or is captured by a hole. The rate of electron and hole capture is governed by the coefficient (C_p). It is also possible that the trap can capture an electron from the valence band as well. The total recombination rate is calculated based on the assumption that thermal equilibrium exists between the four processes and the rate of capture is equal to the rate of emission.

$$R_{SRH} = B_{SRH}\,(np - n_1 p_1), \tag{2.15}$$

where $B_{SRH} = C_n C_p N_t / [C_n(n + n_1) + C_p\ (p + p_1)]$, C_n is the probability per unit time that the electron will be captured by an empty trap, C_p is the probability per unit time a hole will be captured by the trap filled with an electron. N_t is the total density of electron traps. The product of n_1 and p_1 under equilibrium condition is related as, $n_1 p_1 = n_i^2$, where n_i denotes the intrinsic carrier concentration in the semiconductor.[118]

Chapter 3 Experimental Techniques

This chapter discusses the basic experimental techniques utilized to characterize the structural and optical properties of the materials used in this thesis. These methods are grouped into three categories: material, optical, and thin film characterizations. We will also introduce various techniques used for fabricating LEDs and explain the procedure to calculate the essential performance metrics.

3.1 Material Characterization

3.1.1 X-Ray Diffraction

X-ray powder diffraction is a common analytical technique used to identify the phase of a crystalline material and measure crystallographic lattice constants, grain size, strain, symmetry, and atomic positions. X-ray diffractometers consist of three main elements: an X-ray tube, a sample holder and X-ray detector. XRD analysis is based on constructive interference of monochromatic X-rays due to the periodic arrangement of atoms in a crystalline sample. X-rays are generated by a cathode ray tube, filtered to yield monochromatic radiation, and directed at a variable angle (θ) toward a sample. The interaction of X rays with the sample produces constructive interference when the angle satisfies Bragg's law: $n\lambda=2d_{hkl}\sin\theta$, where n, is an integer, λ is the X-ray wavelength, d_{hkl} is the inter planar spacing. (Figure 3.1) The diffracted X-rays are collected by the detector which rotates at an angle of (2θ). Due to the random orientation of powder samples, scanning the sample thorough a range of 2θ is required to observe all the diffraction peaks. For typical powder patterns, data is collected ~5° to 70°. d-spacing is equal to $a/\sqrt{h^2+k^2+l^2}$ where, a is lattice constant, hkl are the miller indices of crystallographic plane,

which then allow identification of crystalline materials as each material has a unique set of *d*-spacings. An example X-ray diffraction pattern is shown in the Figure 3.1b

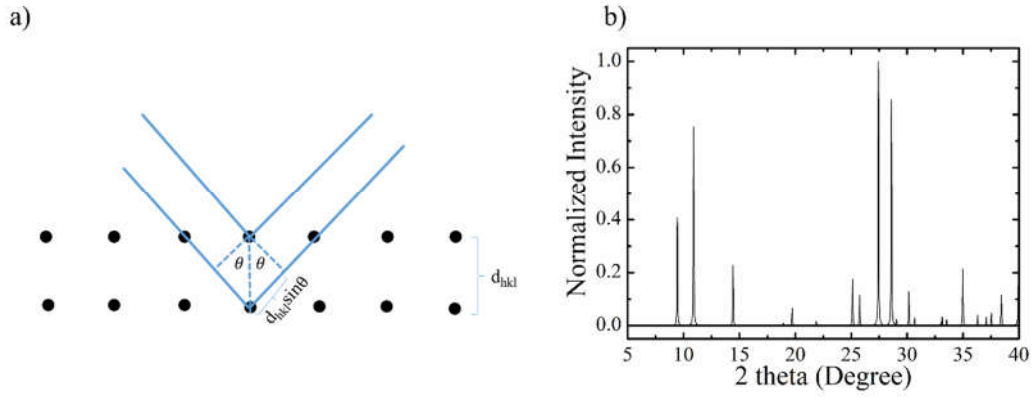

Figure 3.1 Bragg diffraction and example XRD pattern Illustration of X-rays diffraction from the crystalline plane with a spacing (d_{hkl}) due to the constructive interference b) Example diffraction pattern of as synthesized $Cs_2Mo_6I_{14}$

3.1.2 NMR Technique

Nuclear magnetic resonance (NMR) is a technique primarily used to identify the structure of organic compounds and analyze the purity of a sample. The basic principle of NMR is that the nucleus of an element acts as a charged particle in motion and has magnetic moment that can be altered by an external magnetic field. Specifically, nuclei with odd atomic number such as ^{1}H, ^{13}C , ^{19}F, and ^{31}P have nuclear spin (I=1/2). When an external magnetic field is applied, some nuclei in the sample align with the direction of the magnetic field and occupy the lowest energy spin state ($+\frac{1}{2}\alpha$). Similarly, the remaining nuclei will be in the opposite direction to external field and occupy the higher energy spin state ($-\frac{1}{2}\beta$).The difference between these two spin states is very small and dependent on the external magnetic field strength and the type of nuclei under study. The energy difference between these states is usually given in the frequency unit of MHz. Upon irradiating the sample with a radio frequency (RF) corresponding to the spin state energy difference of the nuclei,

some of the nuclei at the lowest energy spin absorb energy and reach the highest energy spin state. The absorbed frequency of this transition depend on the effective magnetic field at the nucleus as electron surrounding the nucleus modify the magnetic field through shielding. When the nuclei at the higher excited state relax to the lower energy spin state, it gives off the excess energy and the frequency of the excess energy is recorded. A schematic of NMR instrument is shown in the Figure 3.2

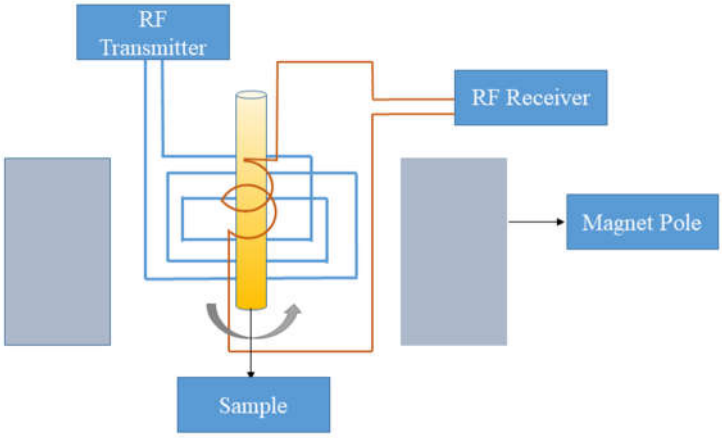

Figure 3.2 Simple schematic of a NMR instrument

Since the response of nuclei changes depending on the strength of the applied magnetic field and the RF frequency, a reference compound to characterize the specific location of the NMR peaks is needed. Tetramethylsilane is a typical reference standard, routinely used for organic compounds as it give single sharp NMR peaks which does not interfere with the resonance of atoms in the organic compounds. The difference in the frequencies that cause transition in the atomic nuclei is very small, NMR spectrum is plotted using the chemical shift (δ) with a unit of parts per million (ppm). Chemical shifts can be calculated as, $\delta = \left[\frac{v_{sample-v_{ref}}}{v_{ref}}\right] x\ 10^6$, where v_{sample} is the frequency of sample and v_{ref} is the frequency of the reference. In this thesis, we use

^{19}F NMR to confirm the apical ligand exchange reaction with the nanoclusters used in the Chapter 6.

3.1.3 Mass spectrometry

Mass spectrometry (MS) is an analytical technique used to perform both quantitative and qualitative analysis of chemical compounds by measuring mass to charge ratio of gas phase ions generated from the sample. A mass spectrometer consist of three main components: an ion source, a mass analyzer and a detector. In a typical measurement, a sample dissolved in a liquid is ionized using electrospray ionization. Ions are created by bombarding the sample with high energy electrons (>1kV). In addition to ionization, some molecules can also break into charged fragments. These ions are accelerated, separated based on the mass-charge ratio as the same mass to charge ratio ions undergoes same deflection when subject to the electric or magnetic field in a quadrupole-time of flight detector (QToF). The separated ions are detected by the electron multiplier. The mass to charge ratio is then compared with the known masses and identification of sample mass can be achieved. Example mass spectrum of tetra butyl ammonium salt is given in the Figure 3.3.

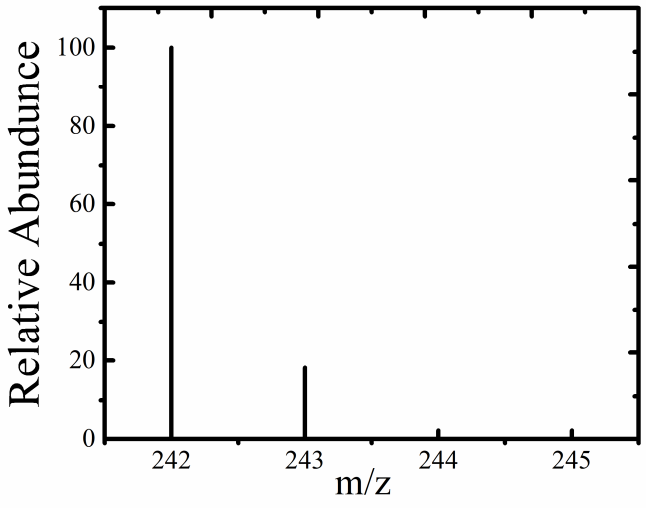

Figure 3.3 Example mass spectrum of tetra butyl ammonium iodide in acetonitrile solution recorded in the positive mode

In this thesis, mass spectrometry is used to confirm the identity of the products synthesized, particularly molybdenum iodide based nanoclusters. Mass spectra were obtained using nanocluster solutions prepared in acetonitrile and directly injected for 2 minutes using an eluent of 50:50 water: acetonitrile. Mass spectra were acquired using a dynamic range extension over *m/z* 50 to 1,500, with mass resolution ($M/\Delta M$, full width-half maximum) of approximately 20,000. Other parameters include capillary voltage of 2 kV, desolvation temperature of 350°C, source temperature of 100°C, and desolvation gas (N_2) at 400 L h^{-1}

3.2 Optical Characterization

In this section, we discuss the basics of the instruments used for the optical characterization of synthesized materials.

3.2.1 UV- Visible Spectroscopy

Ultraviolet-visible (UV-VIS) spectroscopy measures the transmission in the UV–visible-infrared region of the electromagnetic spectrum of thin films coated on substrates or solutions contained in cuvettes. Figure 3.4 shows the schematics of the dual-beam spectrometer. A typical spectrometer contains a light source such as deuterium lamp or xenon arc lamps that emit light in the wavelength between 300 nm and 2500 nm. Light is passed through a monochromator or prism to separate into component wavelengths and split into two beams of equal intensity using a beam splitter. One beam is then passed through a sample compartment and another beam is directed to the reference compartment that consist the blank solvent in the case of solution measurement or nothing for absolute thin film measurements. Detectors at each wavelength measure the intensity of these two beams and transmission ($T = I/I_0$) can be obtained in which I_0 and I are the intensity of reference beam and sample beam respectively, typically plotted against wavelength. Before measuring the transmission of the sample, it is necessary to perform an autozero of spectrometer.

During this step, the spectrometer is calibrated by measuring the intensity of the sample and reference beam to quantify the amount of light in each beam at every wavelength.

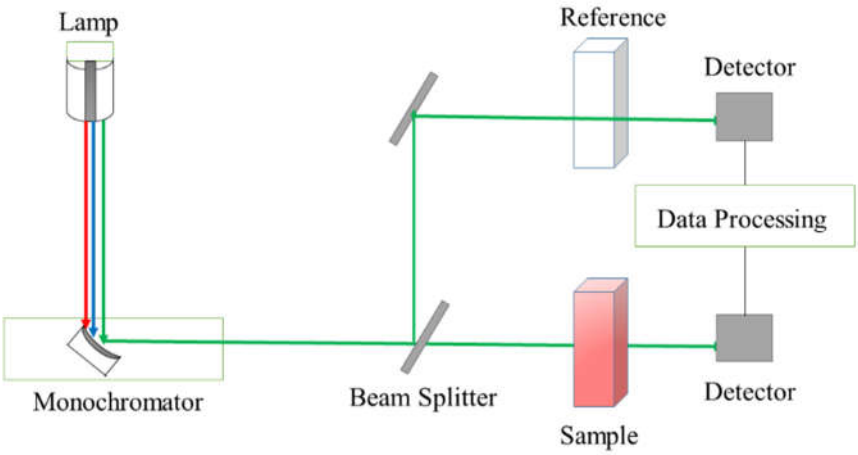

Figure 3.4 Simple schematic of a UV-VIS spectrometer

A blank solvent is placed in the reference compartment to separate the transmission of solute dissolved in the solution from the cuvette reflections. However, for thin film on glass substrates using a blank glass substrate as a reference should be avoided as the reflection from the glass/air interface cannot be properly separated by simple subtraction with thin films. From the measured transmission, absorbance *(A)* can be obtained using the equation A = -log (%T/100%). The absorbance can subsequently be converted to molar absorptivity as $\varepsilon = A/bC_s$ where b is the path length (1 cm) and C_s is concentration of the solution and high molar absorptivity indicates higher oscillator strength of the molecule. This molar absorptivity can then be utilized in the Beer-Lambert relationship. The absorption cut-off wavelength can be used to estimate the optical band gap which is often utilized to estimate the LUMO energy level of the molecules.

3.2.2 Spectroflurometry

Photoluminescence spectra and quantum yields of the materials used in this thesis are measured with a spectroflurometer. The spectroflurometer consists of a light source, an excitation

monochromator, a sample holder, an emission monochromator and a detector. Light from the source for example, xenon lamp is passed thorough an excitation monochromator to separate the component wavelengths. The light with a selected wavelength is then directed through a beam splitter, which reflect about 4 % of the incident light to the reference detector. This is necessary to correct the lamp output when varying excitation wavelength to account for differences in detector sensitivity. The transmitted light from the beam splitter is incident upon the sample, which may be a thin film, or a solution of molecules dissolved in a solvent. The emitted light from the sample is then passed through an emission monochromator before reaching detector, which is often a photomultiplier tube. Figure 3.5 shows a simple schematic of spectroflurometer.

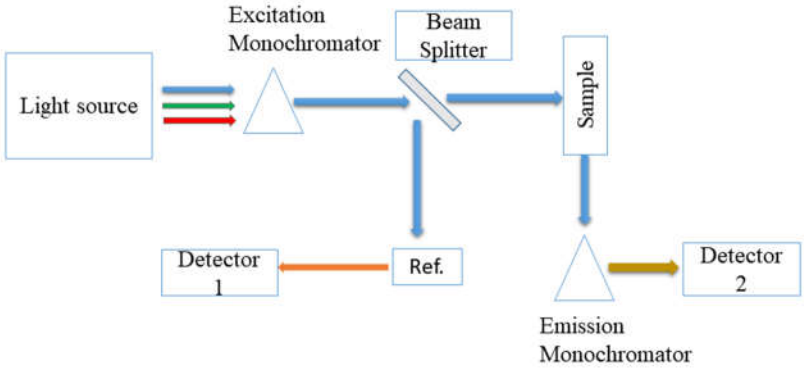

Figure 3.5 Simplified schematic of a spectroflurometer

The spectroflurometer used in this study is capable of recording both the emission and excitation spectra. An emission spectra is the wavelength distribution of an emission recorded at a single excitation wavelength. Conversely, an excitation spectrum is measured by setting a single emission wavelength upon scanning excitation wavelength. For both scans, filters are typically necessary on the emission side and excitation of spectroflurometer to reduce the influence of the background and to avoid false signals originating from wavelength doubling in the monochromator. Commonly used filters are made of molecules that absorb in specific wavelength or dielectric films and can be classified as long pass or short pass filters. While long pass filters allow any wavelength

above the wavelength cut off to be transmitted, short pass filters enable wavelength shorter than to be transmitted. For example, the nanoclusters developed in this thesis show absorption between 350 nm to 450 nm along with the photoluminescence above 650 nm. To measure PL spectra of these compounds, we typically excite the sample at 375 nm and use long pass filter with a cut off wavelength at or above 400 nm on the emission side to completely isolate the excitation signal.

3.2.2.1 Photoluminescence Quantum Yield (PLQY)

PLQY is an important figure of merit, which helps identifying the potential emitters for LEDs application. The higher the quantum yield, the better the efficiency of the fluorescent and phosphorescent emitter and is a prerequisite for fabricating LEDs with those materials. There are several approaches to measure the PLQY including relative and absolute methods. In a relative method, the quantum of yield of the sample is obtained by comparing the PL intensity of a standard with a known quantum yield and refractive index. However, this technique requires complete characterization of photoluminescence properties of the standard and the quantum yield should not vary in different solvents, gas environment, or concentration.[119] To overcome this, absolute quantum measurements have been introduced by utilizing an integrating sphere and are now the most reliable absolute QY measurement. An integrating sphere contains an inner surface coated with a highly scattering material with almost 100 % scattering efficiency with very little absorption. All the light that is emitted from the sample along with light that is waveguided and reflected undergo many scattering events within the sphere to create a uniform distribution throughout the sphere. The uniformly distributed light exits thorough a small aperture to reach a detector. A typical PLQY measurement set up is shown in Figure 3.6

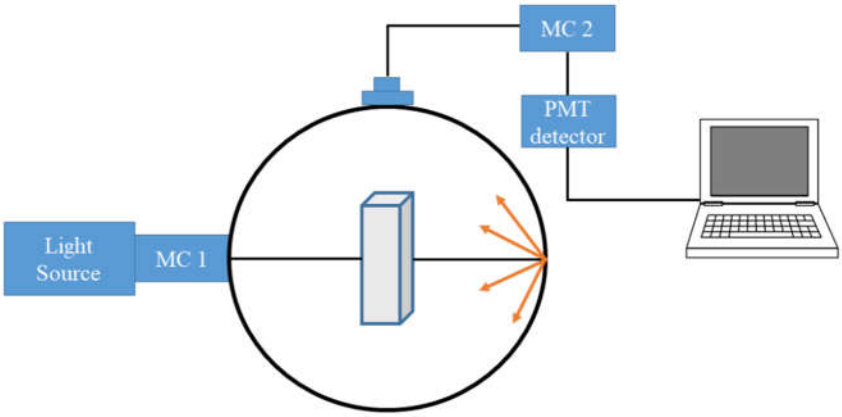

Figure 3.6 Simplified representation of quantum yield measurement where the sample is loaded in the integrating sphere for measuring quantum yield. Light is passed through monochromator 1 (MC1). The orange line indicates the emitted photons scattered inside the sphere before reaching the monochromator 2 (MC2)

The PLQY is obtained by the sequence of two emission measurements using the same configuration of spectroflurometer to cover the whole region of wavelength in which the luminescent molecule absorb and emit light. First, a measurement is performed with a blank solvent without the luminescent molecules to measure the total excitation intensity. Then the sample of interest is measured. Background excitations scan also performed with just the blank solvent for solution or bare substrates for thin films, which can be used to subtract the intensity of light around the luminescence region of the sample. Due to the need to record the signal in both the exciting and emitting regions, it is very difficult to utilize filters during these scans and therefore it is necessary to consider wavelength doubling in the design of the excitation wavelength. An example of scans for a sample and blank are given in Figure 3.7

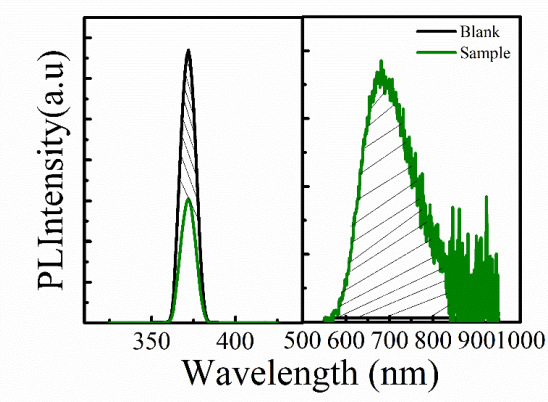

Figure 3.7 Example PL spectra of blank and sample Photoluminescence intensity of blank and sample measured using an integrating sphere at an excitation wavelength. The difference in the area under the excitation peak for bare substrates/ blank solvent and sample film/ solution corresponds to the number of absorbed photons and the area under the spectrum in the region where sample emits gives the number of emitted photons relative to the number of absorbed photons

By recording the change in the excitation intensity of background and sample, the quantum yield can be calculated using the equation 3.1,

$$QY = \frac{\upsilon_{em}(\lambda_{em}) \int \frac{\lambda}{\hbar c} I_{em}^{S} \, d\lambda}{\upsilon_{ext}(\lambda_{ext}) \int \frac{\lambda}{\hbar c} [I_{ext}^{B} - I_{ext}^{S}] d\lambda} \,, \tag{3.1}$$

where υ_{em} and υ_{ext} are the calibration factors at the wavelength ranges of emission and excitation light. I_{em}^{S} is the luminescence intensity of the sample; I_{ext}^{B} and I_{ext}^{S} are the excitation intensity of the blank and sample respectively.

There are a number of considerations for accurately measuring the QY of a sample. An excitation wavelength is chosen so that the solution of interest results absorption around 0.1 to avoid reabsorption losses that lower the effective quantum yield measured. Typically, the solution needs to be oxygen free which can be achieved using multiple freeze-pump thaw cycle or purging with dry nitrogen as oxygen quench the phosphorescence emission by forming singlet oxygen species resulting lower quantum yield. Note, that for these measurements the excitation wavelength should be carefully selected so that there is no potential for wavelength doubling or

the need for short- or long-pass filters. For the measurement to work correctly, both scans need to be made without such filters so that the absolute differences between the exciting intensity and the emission intensity are not skewed.

For consistency, the quantum yield of known standard fluorophores such as rhodamine 6G (QY = 0.95 in ethanol) or fluorescein (QY = 0.95 in 0.1M NaOH) are measured along with the sample of interest using the same experimental conditions as these materials have well characterized photoluminescence properties with a quantum yield.[120]

3.2.2.2 Luminescence Lifetime Measurements

Measuring the photoluminescence lifetime aids in identifying radiation process involved, for example distinguishing between fluorescence or phosphorescence mechanisms, defect quenching, etc. Fluorescence lifetimes are typically in the range of nanoseconds and phosphorescent lifetimes in the range of microseconds to milliseconds. Figure 3.8 shows the typical set up used for measuring lifetime of luminescent materials

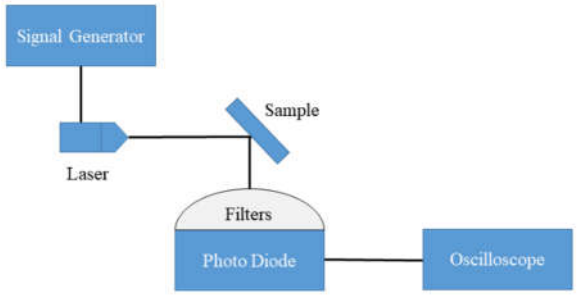

Figure 3.8 Simple schematic of the setup used for measuring photoluminescence lifetime

Both the lifetime of photoluminescence and electroluminescence processes are experimentally measured by exciting the sample with a 375 nm laser (response time of 1ns) modulated by a pulse generator. The emitted light is detected by the photodiode (PDA-36A) from Thorlabs (rise time of 14 ns) positioned at 45° to the sample. Dielectric filters can be installed at

the front of photodiode to isolate the excitation laser signal and various components of the emission spectra. The decay of photocurrent during each pulse is monitored by an oscilloscope (Agilent technologies DSO-X- 3032A oscilloscope (2 ns)) connected to the photodiode. The lifetime is determined by fitting the decay curve (Figure 3.9) to an monotonic exponential decay function shown below in the equation 3.2,

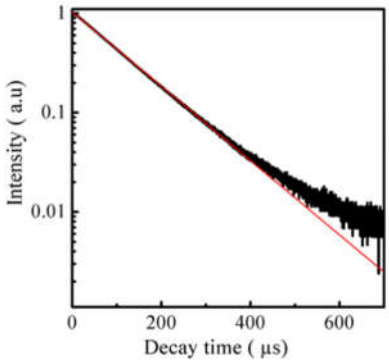

Figure 3.9 Example decay curve and the fitting (red) with a singlet decay constant representing a photoluminescence process with non-competing emission mechanisms.

$$I(t) = I_o e^{-\frac{t}{\tau}} + C\,, \tag{3.2}$$

where I_0 is the initial transient intensity, t is the time after the luminescence and C is a constant that accounts for the background signal.

3.3 Thin film Characterization.

3.3.1 Ultraviolet Photoelectron Spectroscopy (UPS)

UPS is a technique utilized to measure the HOMO level and work functions of molecular semiconductors films. Photons with energy between 10-45 eV are used to excite and eject electrons via the photoelectric effect. Figure 3.10 show the typical schematic of the UPS instrument. It consists of a source of fixed energy radiation, an electron energy analyzer, and an ultra-high vacuum environment. In this measurement, the kinetic energy (KE) of photoelectrons emitted is

converted to binding energy (BE) using the equation KE = $h\upsilon$-BE. In a typical laboratory measurement, photons with the energy 21.2 eV (He I) are produced by a gas discharge lamp filled with Helium gas. An electron energy analyzer uses an electric field between the two hemispherical surfaces to isolate the electrons according to their kinetic energy and measure the flux of emitted electrons. A high vacuum environment is necessary to prevent the gas phase collision of the emitted electrons.

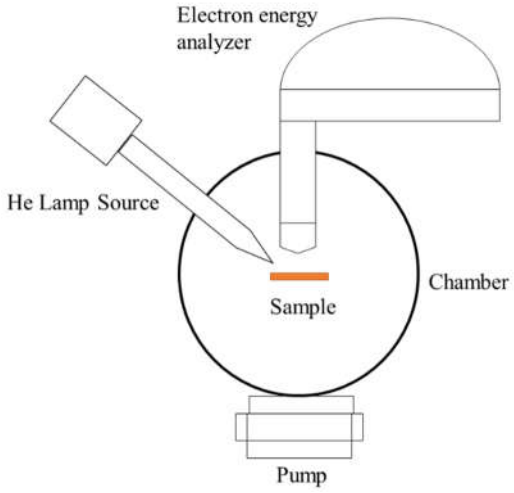

Figure 3.10 Simple schematic representation of a UPS instrument

Since UPS uses low energy photons, most core level electrons are not accessible and measurement is limited to the valence band region or HOMO levels for organic semiconductors. As a result, UPS is a surface sensitive measurement and the information depth is approximately 1-2 nm. In addition, the work function is strongly influenced by the variation in composition at the surface and atmospheric contamination; the materials are typically loaded inside the glove box in a specially designed capsule that is then subsequently loaded into the UPS chamber without exposure to air. During the measurement, the sample is biased with a voltage (20 V) to isolate the low energy cut off from the spectrometer response. Figure 3.11 shows the full UPS spectrum of and the zoomed in portion of the low binding energy region. The work function is measured by

subtracting the width of the photoelectron spectrum (highest binding energy cutoff to the lowest binding energy cut off), from the incident photon energy. The HOMO level is then obtained by summing the work function and the low binding energy cut off.[14]

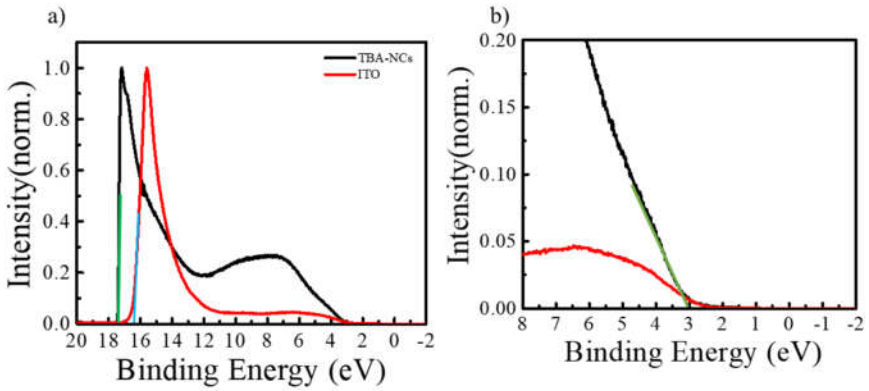

Figure 3.11 Work function and HOMO level measurement a) Complete binding energy normalized spectra of ITO and TBA-NCs corrected to known work function of ITO. b) Zoomed low binding energy portion of a) to calculate the HOMO energy level. For ITO, the work function is 21.2-16.4 = 4.8 eV, For TBA NC the work function 21.2-17.5 = 3.7 eV and the HOMO is 3.7+3 = 6.7 eV

3.3.2 Ellipsometry

Thin film thicknesses made via solution and thermal evaporation processes were measured using spectroscopic ellipsometry. Ellipsometry measures the change in polarization of light reflected or transmitted from a material. Figure 3.12 shows the typical ellipsometric instrumental configuration that consists of a light source, polarizer, sample, polarization analyzer and detector.

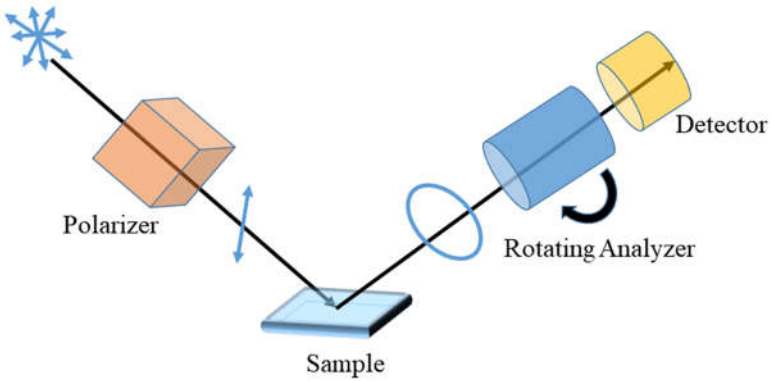

Figure 3.12 Schematic representation of ellipsometry instrument used for measuring thickness

During the measurement, the light source produces unpolarized light which then passed through a polarizer. The polarizer converts the un- polarized light to linearly polarized light which may be decomposed into p and s components. The light that is polarized parallel and perpendicular to the plane of incidence is known as p and s polarized respectively. The exiting light from the polarizer is directed towards the sample, the reflected light from the sample will be elliptically polarized with different s and p amplitudes and travel through the analyzer. The output of analyzer is detected by the detector that converts the light output to electronic signal and the amplitude of s and p polarization (r_s and r_p) of reflected light is normalized to their initial value. To accurately determine the polarization ratio, the angle of incidence is chosen close to the Brewster angle of the sample. The change of polarization is obtained in terms of ellipsometry parameters such as amplitude ratio (Ψ) and phase difference (Δ) according to the equation 3.3,

$$\rho = \frac{r_p}{r_s} = tan(\Psi)\, e^{i\Delta}, \tag{3.3}$$

A model analysis needs to be performed to obtain the optical constants (n,k) and thickness of the film (d) using ellipsometric parameters. First, a wavelength region is chosen in which the film is transparent (k =0) and n in that region can be determined using Cauchy-Urbah model. Next,

an iterative procedure is used in which ellipsometry parameters are calculated by changing the thickness and then compared with the experimentally measured parameters.[121]

3.4 Device Fabrication

Devices were fabricated using wet and dry processing techniques. Spin coating, ink-jet printing and doctor blading are examples of wet processing techniques, and vacuum thermal evaporation (VTE) and organic vapor phase deposition (OVPD) are examples of dry process techniques. In this work, all the devices were fabricated using VTE and spin coating.

Devices were fabricated on the prepatterned indium tin oxide (ITO) substrates (12 mm x 12 mm). Before fabricating devices, the substrates need to be free of dust and other contaminants and this can be achieved by a sequential cleaning process that consists of the following steps: substrates are sonicated for three minutes in soap, DI water, acetone followed by submerging in boiling isopropanol for three minutes. Then, the substrates are air dried and treated in oxygen plasma for 90 seconds. After plasma treatment, the substrates are transferred immediately to the glove box for subsequent thin films deposition.

3.4.1 Spin Coating

Spin coating offers a number of advantages such as easy setup, low initial cost, and enables fabrication of thin films that cannot be thermally evaporated. The main drawback in the spin coating technique is the low utilization of materials as the process wastes about 90-95% of the material that is spun off. Another challenge is finding orthogonal solvents so each new layer does not remove or alter the morphology of the bottom layer when fabricating multilayer devices.

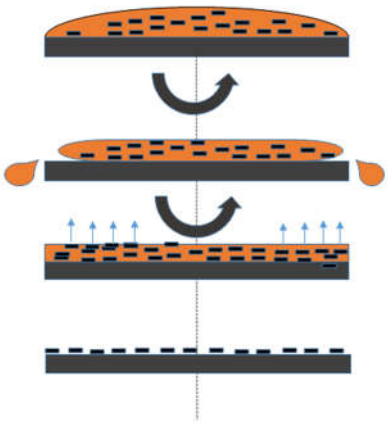

Figure 3.13 Diagram showing the steps involved in the spin coating process.

Figure 3.13 shows the typical steps involved in the fabrication of thin films using spin coating. First, a solution of organic material is made in a high vapor pressure organic solvent. Typical solvents used for spin coating process include: acetone, ethanol, chloroform, chlorobenzene, methanol, and dichloromethane. Cleaned substrates are mounted over the vacuum chuck in the spinner. The solution is then pipetted to cover the entire area of the substrate that is at rest (static) or spinning at a set speed (dynamic). The centrifugal forces dispense the solvent on the substrates into a thin liquid film. Upon solvent evaporation, thin solid films of organic materials are formed on the substrate. The important factors that control the thickness of the films are material concentration and solvent evaporation rate which in turn depending on the viscosity of solvents, vapor pressure, and ambient humidity. Generally the thickness varies as $1/\sqrt{\omega}$.[122] Where ω is the spin speed hence higher spin speeds and longer spin time results thinner films.

3.4.2 Vacuum Thermal Evaporation (VTE)

Thermal evaporation is a versatile technique that allows deposition of organic, inorganic and metal thin films. Figure 3.14 show a simple one source vacuum thermal evaporator in which the chamber is typically maintained at the pressure of 10^{-6} to 10^{-8} torr using the combination of rough and turbo pumps.

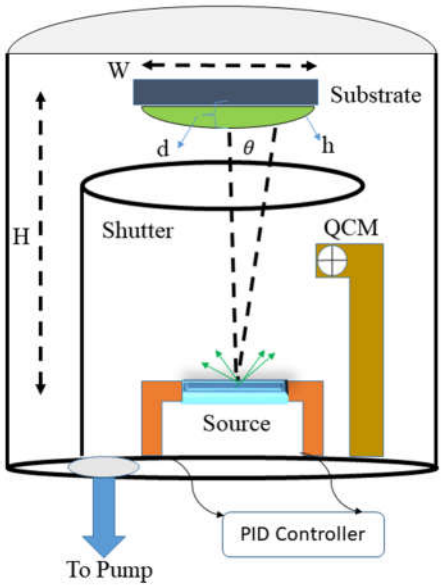

Figure 3.14 Schematic of a single source thermal evaporator.

Small molecular weight organic compound of interest is loaded into specialized boats made of tungsten or tantalum. The boat is heated via resistive elements allowing materials to evaporate. The flux of vapor is then travelled upwards and thin films are formed on the prepatterned ITO substrates positioned above the source. For a point source that give hemispherical evaporative flux, the thickness profile (h) can be obtained using the equation 3.4, [123]

$$h = d\cos^m \theta\,, \tag{3.4}$$

where d is the peak film thickness and m is the source dependent exponent. The thickness can be monitored using a quartz crystal monitors (QCMs) that are poisoned over the source that resonate at specific frequencies depending on the volume of thin film deposited. It is clear that to achieve uniform film thickness θ must be small that typically requires $W/H < 0.01$ and hence large chambers. Because of this geometrical constraints VTE process always results low materials utilization efficiency ~3 to 5 % . In addition, materials also deposited on the walls of the chamber that might lead to contamination of source materials and affect rate of evaporation. To improve

the utilization efficiency, modification of source boats such as linear and planar boats have been developed and substrates can also be linearly translated along with the source to maintain uniformity. Despite the low utilization, VTE process allow to fabricate good quality films with lower non uniformity in thicknesses.

The typical deposition rate used in the VTE process is 0.5 to 2 Å/s and can be controlled by adjusting current flow to the heating element using PID control. In addition, mechanical shutters are also used to control the thickness of individual layers. Deposition rate is calibrated using tooling factor (TF), which is the ratio of materials deposited over QCMs to that on the substrates. TF is measured prior to fabricating devices using an undoped Si as substrates. Thin films are grown with the thickness of 10 to 20 nm with an initial factor (TF_i). Actual thickness is measured using ellipsometry and final tooling factor (TF_f) is calculated using the equation 3.5

$$TF_f = \frac{\text{Actual thickness (nm)}}{\text{Grown Thickness (nm)}} \times TF_i \,, \tag{3.5}$$

3.5 Electrical Characterization of OLEDs

The performance of OLEDs can be characterized by luminous efficiency, wall plug efficiency, and external quantum efficiency. Optoelectronic characterization is performed by measuring three parameters: device current, voltage and luminescence current along with collecting EL spectrum of the device. These parameters will then be used to calculate OLEDs figures of merits. The measurement set up is shown in the Figure 3.15a where the device is loaded into a device holder and positioned in front of calibrated photodiode shown in Figure 3.15b.

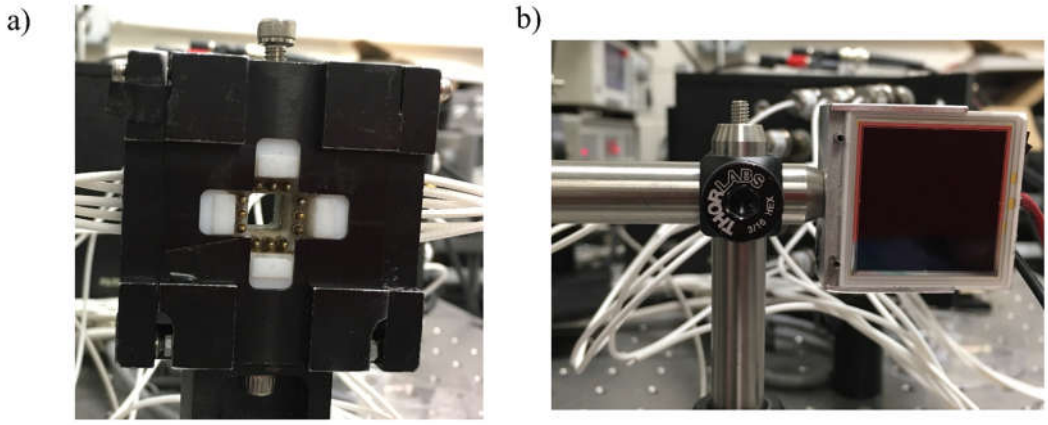

Figure 3.15 a) OLED testing setup where the device is loaded in the black holder b) calibrated Si photo diode that is then placed in front of the holder to collect the forward-emitted light.

The testing setup consists of a source meter, picoammeter, and a channel switcher. The source meter (Keithley 2480) sets the voltage of the devices and allow measurement of the current. The device current, voltage, and luminescence current are measured simultaneously by using a LabVIEW program with a channel switcher that enable automatic measurement of multiple pixels in the substrates. Typically the device current (I_{OLED} , mA) is converted to current density (J , mA/cm^2) and plotted with voltage (V) in a J-V plot. During these measurements only the forward emitted photons are collected. (Fig.3.16).

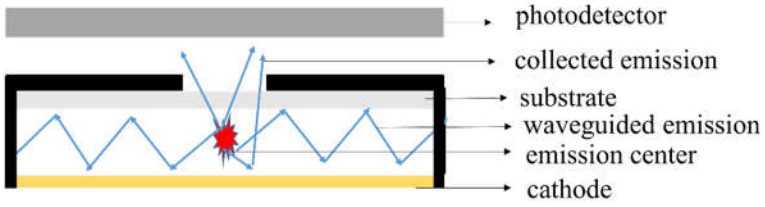

Figure 3.16 Forward emitted vs edge emitted light from the OLED device.

An example J-V-L plot is shown in the Figure 3.17a along with the EL spectrum of a device. (Figure 3.17b). To measure the OLED emission wavelength, a calibrated ocean optics spectrometer (USB 4000) is used to collect the EL spectrum of the devices. Calibration is

performed on the spectrometer using a standard blackbody source with a known color temperature. The intensity of lamp at each wavelength is measured using the spectrometer and a calibration factor is obtained by dividing the normalized intensity measured by the normalized intensity provided by the reference lamp spectra at each wavelength. Corrected spectra are obtained by dividing the actual intensity by the correction factor at each wavelength.

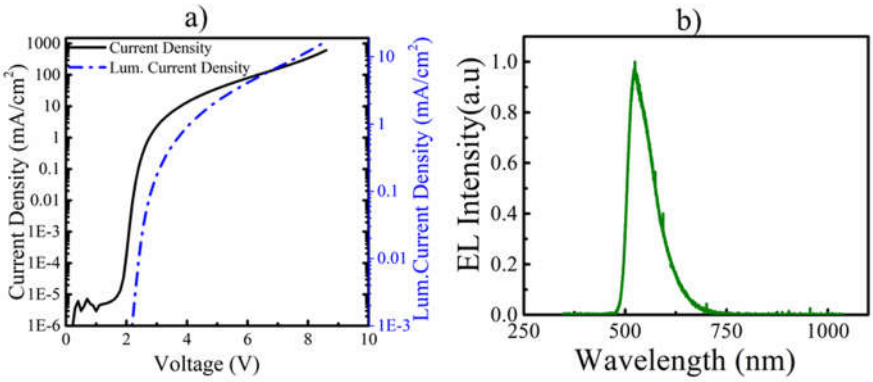

Figure 3.17 a) Device current and photocurrent measured by changing the applied voltage b) Example of EL spectrum of the device at a applied bias.

The photodiode does not directly give the optical power instead it outputs a photocurrent (I_{det}, mA) proportional to the optical power incident on the surface of the detector. The proportionality constant is referred as responsivity(R (λ)) and is measured in the unit of (A/W). The responsivity of the Si detector is shown in Figure 3.18a.

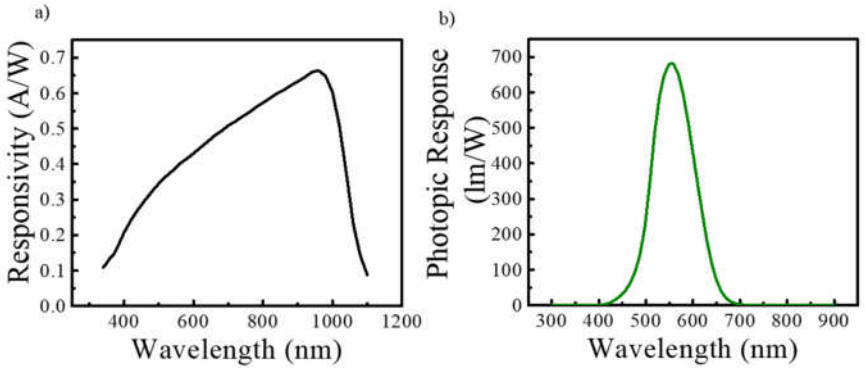

Figure 3.18 Responsivity of Si photodiode and photopic response of the human eye. a) Responsivity of the photodetector used in this thesis and b) the photopic response of human eye under daytime conditions.

For calculating optical power, we first calculate the responsivity of the average wavelength using the equation 3.6,

$$\overline{R} = \frac{\int R[\lambda] \times EL[\lambda]\, d\lambda}{\int EL[\lambda]\, d\lambda}, \tag{3.6}$$

The actual optical power (P_{opt}) can be calculated as a function of voltage as,

$$P_{opt} = I_{det} \times \frac{1}{\overline{R}}, \tag{3.7}$$

3.5.1 Luminous Power Efficiency

In photometry, radiant power measure the total power of emitted electromagnetic radiation and luminous power measure the contribution of total power emitted to produce visible light. The sensitivity of the human eye changes with wavelength. The response of human eye in the day light condition also known as photopic response ($\Phi[\lambda]$) is shown in the Figure 3.18b. As can be seen from the figure, the maximum sensitivity of human eye is achieved at a wavelength of 555 nm under day light conditions.

The SI unit of luminous power is the lumen (lm). Lumens are calculated by weighting the optical power at each wavelength with the luminosity function. Luminous power efficiency (η_p)

is expressed in the units of lm/W and defined as the ratio of luminous power to the electrical power given to OLEDs. Such a unit is only useful for visible light emission. Luminous power efficiency is calculated using the equation 3.8,

$$\eta_p = 683 \frac{lm}{W} \frac{\int \Phi[\lambda] \frac{I_{det}[\lambda]}{R[\lambda]} d\lambda}{I_{OLED}\, V}, \tag{3.8}$$

where, $\Phi[\lambda]$ is the spectral shape of the luminosity function. Another SI Unit for measuring the light output is candela and is defined as the power emitted from an area of unit m^2 per a given solid angle (sr) and typically brightness of displays expressed in candela. The units of candela (cd) and lumen are related by 1 cd = 1 lm/sr. For a Lambertian source that emits light with equal intensity into the half plane, 1 lm = π (1 cd).[124] Brightness is usually normalized to the surface area of emitting devices and reported in cd/m^2. This unit is referred to as a "nit" in the literature.

While the luminous power efficiency is the most important figure of merit to analyze OLEDs performance for lighting and displays designed for viewing with human eye, it is not a good metric to study the performance of NIR emitting OLEDs developed in this thesis as the human eye responsivity drops off beyond 700nm. Hence, additional metrics such as wall plug efficiency and external quantum efficiency are used to study the NIR emitting OLEDs.

3.5.2 Wall Plug Efficiency

Wall plug efficiency (WPE) is the ratio of the total optical power generated to the electrical power injected and can be calculated using the 3.9

$$Wall\ Plug\ Efficiency = P_{opt} \,/\, (I_{OLED} \times V)\,, \tag{3.9}$$

where, I_{OLED} is the device current and V is the voltage. As WPE is wavelength independent, it is a critical parameter for comparing efficiencies of both the visibly emitting and NIR OLEDs. In addition, WPE is a fundamental metric; it reflects the efficiencies of all the steps involved for light

generation in OLEDs and is useful to compare LEDs in terms of operating conditions such as temperature and voltage for application in solid-state lighting. In addition, WPE also allow us to evaluate efficiencies of different light extraction (outcoupling) techniques and help optimize the performance of LEDs.

3.5.3 External Quantum Efficiency (EQE)

To measure η_{EQE}, the photon flux in the forward viewing direction is measured and compared with the flux of electrons injected. While the actual photon flux is obtained by dividing the measured optical power by the energy of average wavelength photon of the EL spectrum, electron flux is obtained directly from the measured device current I_{OLED} being the number of charges per second (q/s) . The average emission wavelength ($\overline{\lambda}$) is obtained as

$$\overline{\lambda} = \frac{\int EL\,[\lambda] d\lambda}{\int \frac{1}{\lambda}\, EL\,[\lambda] d\lambda}, \tag{3.10}$$

Where *h* is the Plank's constant and c is the speed of light and η_{EQE} can be calculated using the equation 3.11,

$$\eta_{EQE} = \frac{q \int \overline{\lambda}\; I_{det}[\lambda]\; d\lambda}{hc\; I_{OLED} \int R\,[\lambda] d\lambda} \times 100\,\%, \tag{3.11}$$

Chapter 4 Mapping Recombination Profiles in Single-, Dual-, and Mixed-Host Phosphorescent Organic Light Emitting Diodes

Recombination dynamics of charge carriers in phosphorescent organic light emitting diodes (OLEDs) play an important role in performance metrics and device optimization even though very little is often known about these processes. In this chapter, we discuss a method developed to probe the recombination profile of OLEDs in-operando using spatially-positioned sensing layers. This method is used to investigate recombination in the emissive host and transport layer interfaces in a single emissive layer (EML) configuration and is extended to study the impact of double- and mixed-host EML architectures. We have identified the factors that control the recombination and overall device performances.

4.1 Introduction

Organic light emitting diodes have emerged as a leading display technology owing to their low power consumption, ultra-thin form factor, flexibility, fast response time, and excellent color-rendering properties. The advent of novel phosphorescent active materials has enabled internal quantum efficiencies to reach nearly 100% by utilizing both triplet and singlet excitons. This breakthrough has enabled peak forward emission external quantum efficiencies (EQEs) of more than 30% for green, red, and blue OLEDs.[125, 126] However, the efficiency of OLEDs typically decreases at higher brightness and current density due to the reduction of charge confinement and quenching through both bimolecular and exciton-polaron mechanisms.[69] To improve charge confinement in OLEDs, exciton blocking layers have been introduced [127] and bimolecular exciton quenching has been minimized by using phosphorescent emitters with a short exciton lifetime,[128, 129] reducing molecular aggregation[130] and broadening the exciton recombination zone (RZ).[68, 131, 132] Since the exciton lifetime and molecular aggregation are

material specific properties, RZ can be modified by changing the single emissive layer configuration (S-EML)[133] to either a double emissive layer (D-EML)[134, 135], a mixed emissive layer (M-EML)[136-139], or a graded emissive layer configuration (G-EML).[70, 140-144]

In conventional S-EML devices, a luminescent emitter is doped in a single host layer that typically exhibit predominant charge transport properties for either holes or for electrons. As a result, the RZ is often located at the interface between minority charge transport layer and the emissive layer with a very narrow RZ thickness.[133] In D-EML configurations, two host materials, each with their own propensity for particular charge carriers, have been explored as a method to expand the RZ zone even though it has been shown to remain relatively narrow.[134, 135] M-EML configurations in which the emitter is uniformly doped in the mixture of hole transport material (HTM) and electron transport material (ETM), have also been shown to improve exciton confinement and enhance performance metrics in some cases.[136-139] Building on the M-EML, further improvements in device performance have been demonstrated using G-EML architectures, in which the mixing ratio of hole and electron transport host materials are continuously (or linearly) modulated in the emissive layer by modifying the evaporation rate of each material during codeposition.[140, 141] Despite the complexities involved in the fabricating devices with M-EML, and particularly G-EML architectures over large areas, it is also shown that the mixing ratio of the host materials can dramatically influence the charge carrier mobilities thus affecting the performance and roll off characteristics.[143, 144] To avoid these complexities, single ambipolar host materials have been demonstrated that have good mobility for both holes and electrons as a potential route to modify recombination profiles.[69, 145-147] While all these emissive layer designs are shown to impact the device performance, questions still remain about

the factors that control recombination in those devices. Hence, experimental determination of the recombination profile in various emissive layer design can deepen the understanding of composition of host materials, impact of host mobilities, and the role of frontier orbital levels of the adjacent transport layers on the recombination dynamics and ultimately improve the performance of OLEDs at high brightness.

Experimental determination of the recombination profile can lead to improved performance for OLEDs. Charge confinement and RZ width in OLEDs have been studied by using: 1) sensing layers; 2) quenching layers; and 3) optical modelling. In sensing layer devices, the RZ was qualitatively explored by monitoring the electroluminescence (EL) spectrum of a sensor molecule as a function of position in the device architecture.[135, 136, 144, 148-151] Similarly, the presence/absence of quenching layers have been used as a qualitative monitor of device EL intensity as a function of position in the device.[152] In such devices, mapping of the RZ profile may be produced based on the assumption that EL intensity is proportional to local exciton density at the sensing layer/quenching layer location [70] The biggest challenge of utilizing the quenching approach is the necessary assumption of exciton diffusion, resonant energy transfer, or electron transfer, complicating interpretation in dilute doped systems. Alternatively, RZ profiles can be indirectly extracted by comparing the EL spectra measured at different angles with optical models derived based on microcavity effects,[153] or from variation of the host energetics.[154]

In this work, we adapt a method to probe the RZ profiles in OLEDs based on position-dependent luminescent sensing layers internally referenced to the primary emitter EL intensity. To test the generality of the method, a range of device architectures were developed using an *in-silico* approach to characterize potential charge injection barriers. Specifically, carbazole and triazine based hosts were predicted to exhibit preferential charge injection from the hole and electron

transport layers respectively. The sensor method was used to confirm preferential recombination at the minority carrier interface. The method was subsequently extended to systematically characterize the RZ in various architectures (S-EML, D-EML and M-EML). Our results show that although these structures have only a small impact on the peak quantum efficiency, they play a significant role in the roll-off and power efficiency characteristics of OLEDs at high current densities.

4.2 Experimental

Devices were fabricated using the device architecture described in Table 4.1.

Table 4.1 Device architecture used in this study

Devices	HTL	EML	ETL	Cathode
S-EML(E-host)	NPD (40 nm)	E-Host:$Ir(mppy)_3$ (10 vol.%,30 nm)	BTB (30 nm)	LiQ/Al (0.8/80 nm)
S-EML(H-host)	NPD (40 nm)	H-Host:$Ir(mppy)_3$ (10 vol.%,30 nm)	BTB (30 nm)	LiQ/Al (0.8/80 nm)
D1-EML (E-Host/H-Host)	NPD (40 nm)	E-Host:$Ir(mppy)_3$ (10 vol.%,15 nm) / H-Host:$Ir(mppy)_3$ (10 vol.%,15 nm)	BTB (30 nm)	LiQ/Al (0.8/80 nm)
D2-EML (H-Host/E-Host)	NPD (40 nm)	H-Host:$Ir(mppy)_3$ (10 vol.%,15 nm) / E-Host:$Ir(mppy)_3$ (10 vol.%,15 nm)	BTB (30 nm)	LiQ/Al (0.8/80 nm)
M-EML (E-Host: H-Host)	NPD (40 nm)	E-Host and H-Host:$Ir(mppy)_3$ (75:25, 50:50,25:75) (10 vol.%,30 nm)	BTB (30 nm)	LiQ/Al (0.8/80 nm)

Thin films were sequentially deposited onto the ITO substrate via thermal evaporation at 3×10^{-6} Torr: N,N'-bis(naphthalen-1-yl)-N,N'-bis(phenyl)-benzidine (NPD, Lumtec) as the hole transport layer (HTL); S-EML, D-EML, or M-EML host uniformly doped with tris[2-(p-tolyl)pyridine]iridium(III) ($Ir(mppy)_3$, Lumtec). The S-EML host layer either consisted of 3-(4-(9H-carbazol-9-yl)phenyl)-9-(4,6-diphenyl-1,3,5-triazin-2-yl)-9H–carbazole (E-host, Lumtec) or hole transport host 9,9'-diphenyl-9H ,9'H -3,3'-bicarbazole (H-host, Lumtec). The D1-EML host layers consist of E-host:$Ir(mppy)_3$/H-host:$Ir(mppy)_3$ and D2-EML host layers consist of H-host:Ir(mppy)3/E-host:$Ir(mppy)_3$. M-EML host layers consist of blended (E-host:H-host) with varying volume mixing ratio. This was followed by an electron transport layer (ETL) 4,4'-bis(4,6-diphenyl-1,3,5-triazin-2-yl)biphenyl (BTB, Lumtec) and a cathode consisting of 8-hydroxyquinolinolato-lithium (LiQ, supplied by The Dow Chemical Company) and Al. Sensing layer devices were made using platinum (II) octaethylporphyrin layer (Frontier Scientific) inserted at various positions by briefly halting layer growth. Electrical characterization of the devices were performed using a Keithley 2420 source meter and Keithley 6487 picoammeter. Forward emitted luminescence was measured using a calibrated large area Si photodetector (Hamamatsu) and electroluminescence spectra were collected using an ocean optics spectrometer (USB 4000). The photoluminescence quantum yield of doped films were measured using PTI Quantmaster spectroflurometer using 365 nm excitation wavelength under flowing nitrogen.

4.3 Results

To investigate the role of emissive layer architecture on recombination dynamics, we fabricated and optimized devices in S-EML, D-EML, and M-EML configurations. The calculated relative HOMO-LUMO energies of each molecule are shown in Figure 4.1a along with their chemical structures in Figure 4.1b.

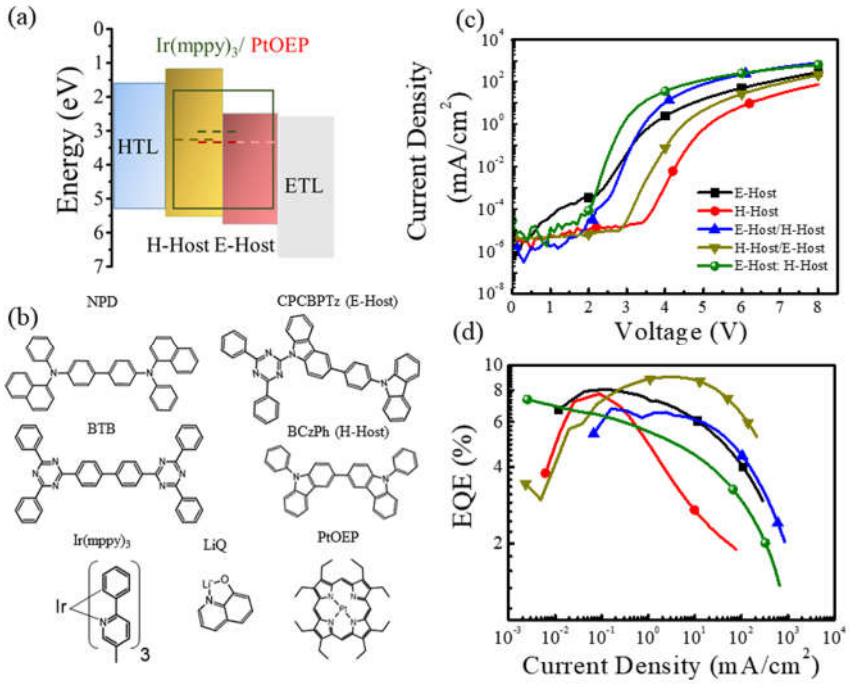

Figure 4.1 Performance of S-EML and D-EML and M-EML devices. Energy level diagram of the device architecture under flatband conditions, where the relative energy levels were obtained using density functional theory (B3LYP/6-31g*) and the triplet energy levels are marked as a dotted line. b) Molecular structures of materials used in this study. c) Current density (*J*) versus voltage (*V*) curves for S-EML devices made with E-host and H-host , D-EML devices consist of E-host/H-host or H-host/E-host, and M-EML devices made with mixture of E-host:H-host (3:1 vol.). d) Comparison of external quantum efficiency (*EQE*), vs. current density or brightness for the S-EML, D-EML and M-EML devices. The legend in Fig. 4.1c) applies to d).

4.3.1 Device Performance Optimization

Before probing recombination zone in the devices, the performance of the devices were optimized .The S-EML devices were optimized by changing the concentration of the dopant. The D-EML were fabricated by varying the order of the host molecules. Figures 4.2 and Figure 4.3 show the *J-V* characteristics, comparison of current density versus EQE and the comparison of power efficiency vs. current density for the S-EML devices made with E-Host and H-Host respectively. Based on the data, The optimum dopant concentration for better performances are 9 vol.% and 12 vol.% for the S-EML (E-Host) and S-EML (H-Host) devices respectively. Figure 4.4 show M-EML devices fabricated by varying volume-mixing ratio of hosts. The devices which

mixing ratio of (E-Host:H-Host,3:1) was found to produce optimum performances. The best performance of the devices are summarized in the Table 2

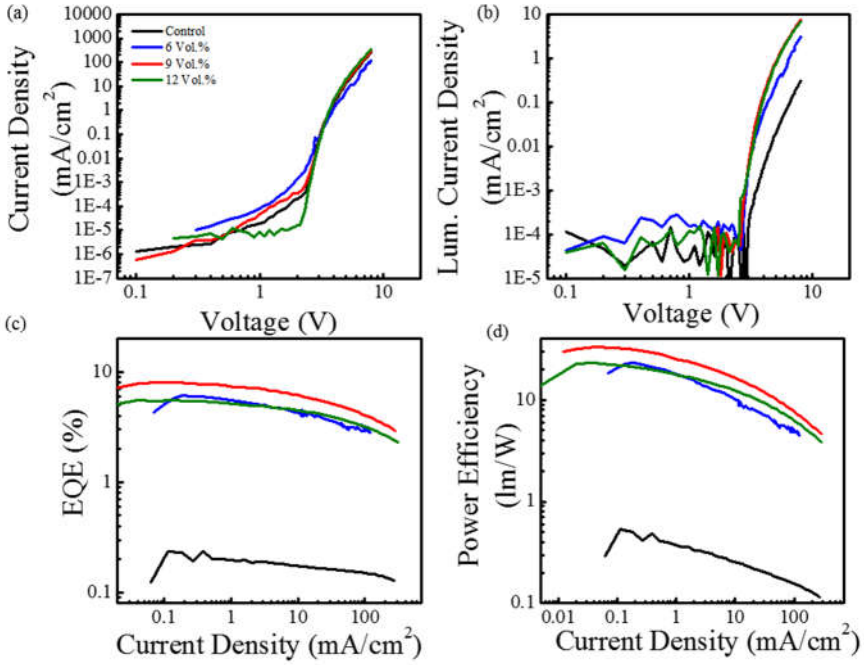

Figure 4.2 S-EML (E-Host) device optimization. Current density vs. voltage for the S-EML (E-Host) devices made with 6 vol.%, 9vol.%,and 12 vol.% along with the control devices that does not have $Ir(mppy)_3$ (same legend applies to b, c, and d). b) Comparison of luminescent current density vs. voltage, c) Comparison of EQE vs. current density and d) Power efficiency vs. current density for the devices

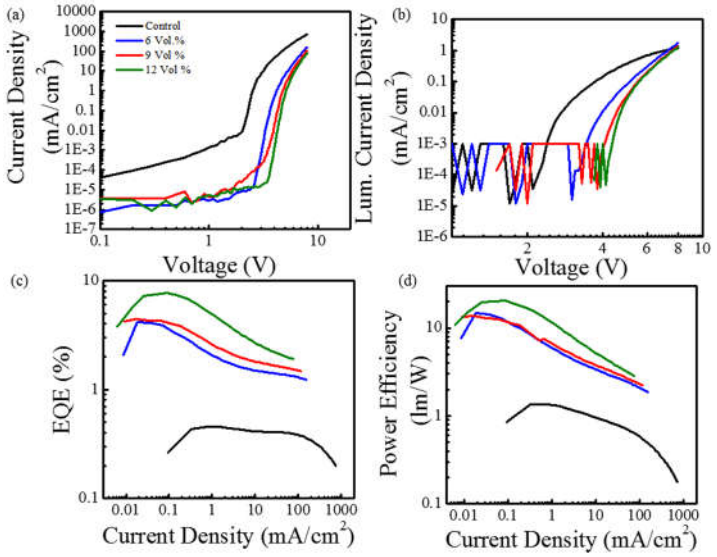

Figure 4.3 S-EML (H-Host) device optimization. a) Current density vs. voltage for the S-EML (H-Host) devices made with 6 vol.%, 9vol.%,and 12 vol.% along with the control devices that does not have $Ir(mppy)_3$ (same legend applies to b, c, and d). b) Comparison of luminescent current density vs. voltage, c) Comparison of EQE vs. current density and d) Power efficiency vs. current density for the devices.

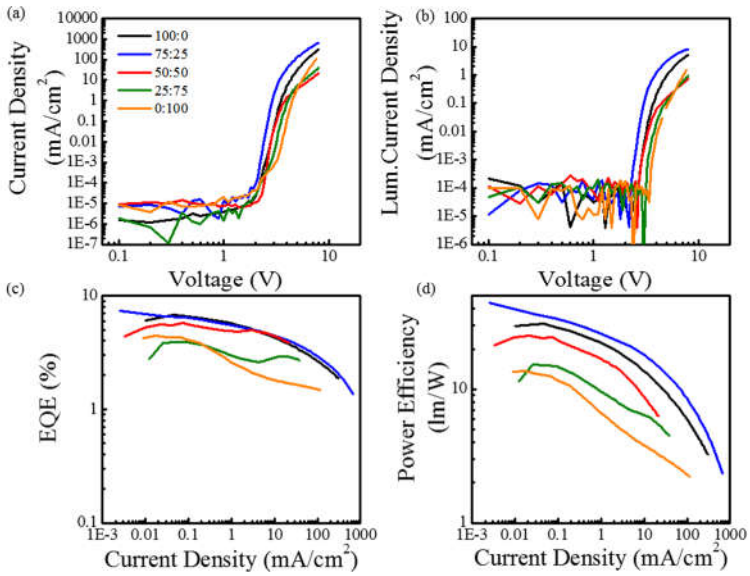

Figure 4.4 M-EML device optimization a) Current density vs. voltage for the M-EML (E Host: H Host) devices made with mixing ratio (100:0, 75:25,50:50, 25:75,0:100) (same legend applies to b, c, and d). b) comparison of luminescent current density vs. voltage, c) Comparison of EQE vs. current density and d) Power efficiency vs. current density for the devices

Table 4.2 Performance metrics of devices fabricated with various EML architectures

Devices	Opt. Turn on @1cd/m^2	Peak EQE (%)	Peak P.E (lm/W)	Peak C.E (Cd/A)	EQE @1000 cd/m^2 (%)
E-Host (S-EML)	2.8	8.2±0.9	25.5.±9.1	20.3±6.6	6.2±0.5
H-Host (S-EML)	4.4	7.5±0.7	20.4±5.1	14.9±5.8	2.3±0.8
E- /H-Host (D1-EML)	3.5	6.53±1.1	18.3±4.0	11.8±2.0	5.8±0.9
H- /E- Host (D2-EML)	3.7	8.5±0.4	23.8±3.6	15.4±0.8	7.6±0.3
E-Host:H-Host (M-EML)	2.3	6.6±0.7	39.1±4.1	14.4±1.4	4.4±0.8

In the S-EML devices, variation in performance follows the trend expected from the injection barriers of the hosts. As seen in Figure 4.1a, the E-host has a low energy barrier for electron injection from the ETL as compared with the H-host (0.1 eV and 1.4 eV, respectively). The large electron injection barrier likely leads to poor electron injection into the H-Host, resulting in greater charge imbalance and higher turn on voltage of the S-EML device. In D-EML devices, the order of host deposition was found to play a crucial role in EQE, luminance power and current efficiencies. The placement of an H-Host adjacent to the HTL led to improved current efficiency and power efficiency over devices where the E-host was deposited next to the HTL. Similar to the S-EML device with the H-host, the lower EQE and current efficiency in the E-host/H-host devices resulted from the large energy barrier to electron injection at the H-host/ETL interface. In contrast, improved EQE, current and power efficiencies in the H-host/E-host configuration may be attributed to efficient charge confinement at the H-Host/E-Host interface. Finally, improvements

in power efficiency and turn on voltage in M-EML devices likely resulted from the enhanced charge carrier transport and efficient carrier injection achieved by the mixing of the hosts.

To prove the enhanced charge transport in the M-EML devices, we fabricated hole only devices using S-EML consist of E-Host and H-Host and M-EML architecture. Hole mobilities were calculated using space charge limited current model.

4.3.2 Hole Mobility Analysis

To obtain space-charge-limited hole mobilities, we fabricated hole-only devices using the architecture: ITO/MoO_3(10 nm) / NPD (0.5 nm)/ Hosts (30 nm)/ NPD (0.5 nm) / MoO_3 (10 nm) / Al. Figure 4.5 shows the *J-V* characteristics of the hole only devices made with single and mixed host layers displaying good symmetry. Hole mobility was extracted by fitting *J-V* curves (Figure 4.5b) using the space charge limited current (SSLC) model. In SSLC regime (~2-6V in these devices), current density is related to the applied bias according to the equation 2.10. From the fitting, hole mobilities of host materials was obtained and listed in the Table 4.3

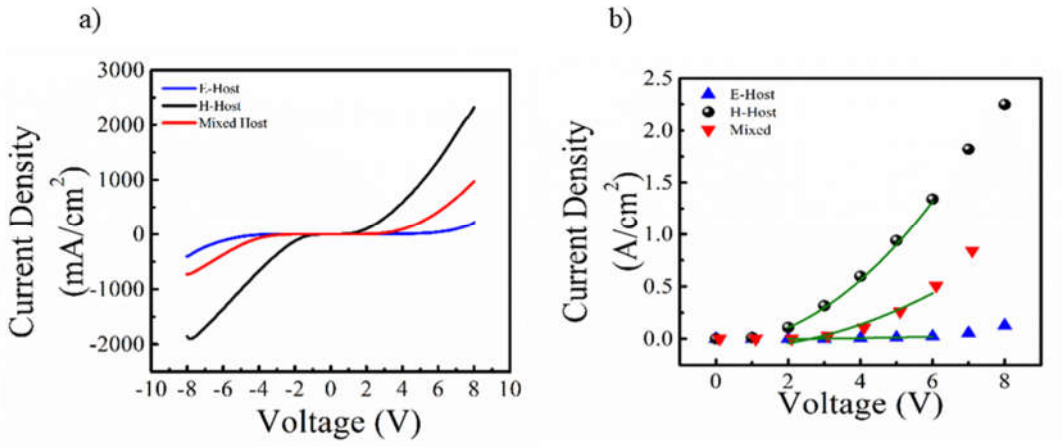

Figure 4.5 Hole mobility analysis J-V curves of the hole only devices made with the single and mixed host layers emphasizing the symmetric nature. b) Fitting of J-V curves of the single and mixed host hole only devices using the space charge limited current model

Table 4.3 Hole mobilities of host materials used in the study

Host	Hole Mobility ($cm^2/V.s$)
CPCBPTz (E-Host)	$6.2\pm0.5 \times 10^{-8}$
BCzPh (H-Host)	$2.8\pm0.1 \times 10^{-6}$
CPCBPTz :BCzPh (Mixed)	$2.2\pm0.1 \times 10^{-6}$

As can be seen from the Table 4.3, mixed host devices showed similar mobility to the H-Host devices and two orders of higher mobility than the E-Host.

4.3.3 Sensor Layer Method

To understand the role of host energy levels on device recombination dynamics, we employed a sensing layer approach. Recombination profiles in the S-EML devices were studied by positioning a sensing layer at various locations and measuring the fraction of sensor emission to the overall device emission at each position. After de-convoluting any overlap in the emitter

and sensor spectra, we integrate each peak area and normalized the sensor signal by the total device emission (*e.g.* from the data in Figure 4.7a and 4.7b) *via* Equation 4.1:

$$F_{Sensor} = \frac{\int \frac{I_{Sens}(\lambda)}{QY_{Sens}(\lambda)} d\lambda}{\int \left(\frac{I_{Sens}(\lambda)}{QY_{Sens}(\lambda)} + \frac{I_{Emit}(\lambda)}{QY_{Emit}(\lambda)} \right) d\lambda}, \quad (4.1)$$

where F_{sensor} is the fraction of sensor photon emission at each position, I_{Sens} and I_{Emit} are the intensity of sensor and emitter component emission respectively, and QY_{Sens} and QY_{Emit} are the quantum yield of the sensor and emitter that are measured to be 30 ± 3 % and 94 ± 5 %. Because the QY and emission peak width of the emitter and sensor are dissimilar, we normalized each signal to obtain the absolute fraction of emission at each sensor position. F_{sensor} is then proportional to the triplet exciton density in the primary emitter stemming from position dependent exciton generation and exciton migration on the host. Some contributions from long-range energy transfer between distant dopants may be present, which will broaden the F_{sensor} profile more than the intrinsic concentration profile, but is likely to be small for these dilute doped systems.[155, 156] To validate there is no long-range energy transfer involved between these dopants, we performed PL measurements by inserting an exciton blocking between the primary emitter and the sensor layer. Figure 4.6 shows PL intensity of $Ir(mppy)_3$ doped thin films made with H-Host with a exciton blocking layer example Bathocuproine (BCP) positioned at various thickness between the primary emitter and the sensor.

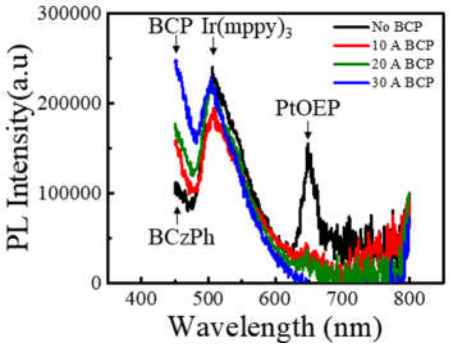

Figure 4.6 PL measurement with blocking layer. PL spectra recorded at 300 nm excitation of films made with and without BCP layer between the primary and sensor emitters.

The data clearly shows even at 10 A BCP thickness, there is no PL signal observed from the sensor and suggesting essentially no long-range energy transfer between the primary emitter and the sensor. Based on this data and the thickness variation seen in our deposition system, we estimate that the resolution of our technique to measure RZ width is around 1nm. We note that a value of F_{sensor} close to 1 has particular significance (all the emission is seen from the sensor) and implies a discrete position for exciton generation. Accordingly, typical values of F_{sensor} are expected in the range of 0-0.5 if recombination is distributed throughout the host (as opposed to discrete positions or interfaces). A significant benefit of this approach is the use of the primary emitter as an internal reference, negating the need for absolute intensity measurements.

4.4 Discussion

4.4.1 Recombination in S-EML Devices

Previous studies have shown that the RZ in S-EML devices is often present at transport and emissive layer interfaces, owing to charge imbalance or interface injection barriers.[157, 158] Figure 4.7a and 4.7b shows the comparison of S-EML device EL spectra recorded with and without the sensing layer being placed throughout the EML.

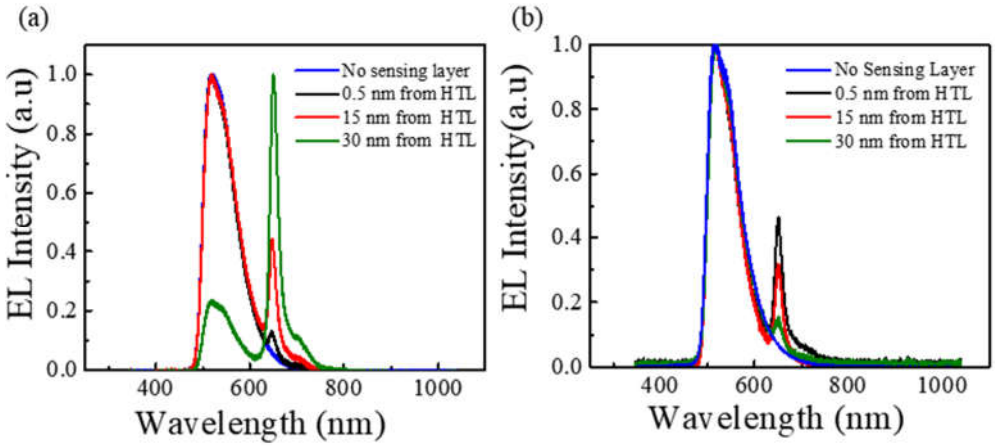

Figure 4.7 Probing RZ in S-EML devices. Comparison of EL spectra obtained at 6 V from a S-EML (H-host) device with sensing layer inserted at various position in the emissive layer b) Comparison of EL spectra obtained at 6 V from a S-EML (E-host) device with sensing layer inserted at various position in the emissive layer

The data clearly shows that the sensing layer EL peak, with a peak wavelength of 650 nm, is consistent with the optically excited PL of the sensor layer combined with the $Ir(mppy)_3$. Based on the 650 nm sensing peak intensity in S-EML made with the H-host and E-host, the majority of the recombination occurs at the H-Host/ETL and HTL/E-host interfaces respectively. For reference, a strong preference for recombination at the HTL interface in 4,4′-Bis(N carbazolyl)-1,1′-biphenyl (CBP) based green OLEDs has been indicated by the energy level modification studies of Matsushima *et al.*[154]

It is clear that the majority of recombination in these S-EML architectures occurs at the interface of the minority carrier transport and emissive layers. Subsequently, we evaluated the impact of the applied potential and device configuration on barrier-limited injection from the HTL and ETL. Figure 4.8 shows the fraction of sensor layer emission in the (a) E-host or (b) H-host devices as a function of position and bias.

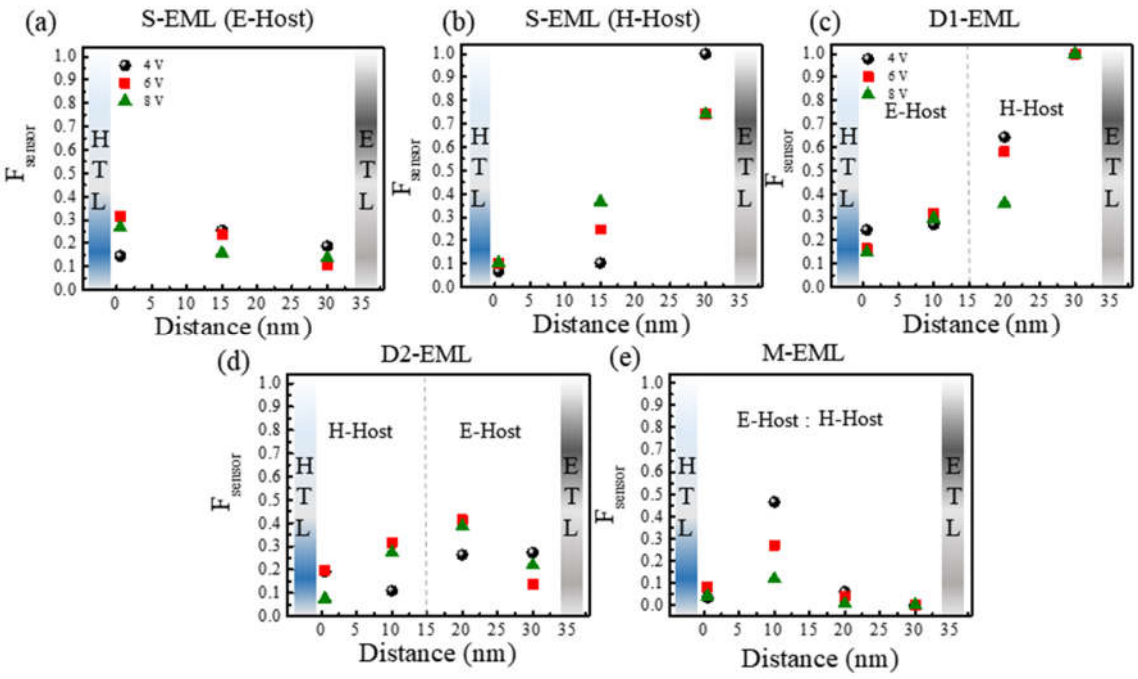

Figure 4.8 RZ profile in S-EML and D-EML and M-EML Devices. Extracted recombination profiles as a function of position and applied bias from the optimized a) S-EML (E-host), b) S-EML (H-host).c)D1-EML (E-host/H-host), d) D2-EML (H-host/E-host) e) M-EML (E-host:H-host) devices. The legend in Fig. 3a) applies to b).

The contribution of sensor emission in S-EML devices with the E-host was similar regardless of the position of sensing layer in the emissive layer and applied bias indicating that the RZ was well distributed throughout the emissive layer in the E-host, with a slight preference for recombination at the hole transport interface. Nonetheless, the relatively flat recombination profile is not surprising considering the molecular structure of the E-host constitute both the electron donating carbazole and electron withdrawing triazine moieties that can aid ambipolar conduction. This recombination profile also suggests good ambipolar injection that is likely a significant component of the reduced roll-off in the EQE and PE over the S-EML H-host. In contrast to the E-host devices, the S-EML H-host device shows a stronger spatial variation in the RZ along with a strong preferential recombination at the ETL interface. In fact, when the sensor layer was placed at the EML/ETL interface, only sensor emission is observed at lower biases ($F_{sensor} = 1$) indicating

that exciton generation is only occurring at this interface. This is attributed to the shallow LUMO of the H-host, leading to poor electron injection from the ETL. At higher bias conditions, a decrease in F_{sensor} is observed, consistent with electrons overcoming the EML/ETL barrier, and leading to RZ broadening. We hypothesize that the sharp RZ at the interface of EML/ETL for the H-host is a key factor in the increased EQE roll off for this device.

4.4.2 Recombination in D-EML Devices

Furthermore, the sensor layer method was extended to RZ analysis in D-EML and M-EML configurations. In D-EML host devices, RZ zone formation was reported to occur at the interface of hole and electron transport hosts.[158] However, in the D1-EML devices shown in Figure 4.8c (*i.e.* E-host adjacent to the HTL), the recombination zone peaked at the ETL interface, similar to the trend seen in the S-EML H-host devices. This data is consistent with the interpretation that an electron injection barrier between the H-host and the ETL dominates the recombination profile. Despite having similar recombination profiles, D1-EML (E-host/H-host) devices surprisingly showed better power efficiency metrics than the S-EML H-host devices. Moreover, the roll-off for the D1-EML was significantly improved over the S-EML H-host. This may be attributed to either an increase in RZ width in D1-EML compared with S-EML (H-Host) devices or from improved hole injection from the HTL to the E-Host into D1-EML devices. For devices based on the D2-EML configuration (*i.e.* reversed host order with H-host adjacent to the HTL) (Figure 4.8d), the RZ was found to peak near the H-Host and E-Host interface as expected for the typical D-EML configuration. D2-EML devices also exhibited improved power efficiency and lower EQE roll off than the D1-EML devices likely due to efficient charge injection from the favorable HOMO and LUMO levels of the H-host and the E-host, with respect to the charge transport layers.

4.4.3 Recombination in M-EML Devices

Previous work exploring the M-EML devices has suggested that the RZ is uniformly distributed throughout emissive layer.[144] However, in this study, the M-EML RZ was surprisingly found to peak near the center of the M-EML layer (Figure 4.8e). Without any clear indication for interface formation at the peak F_{sensor} location, this is type of behavior may be evidence of charge carrier mobility variation upon mixing of hosts. Additionally, host phase segregation may contribute, however is much less likely for the amorphous layers used in this study.

4.4.4 Role of Transport Layers

To understand the role of the transport layer on exciton formation and carrier leakage into charge transport layers, S-EML devices were fabricated with the sensor doped into the ETL and HTL layers. Figure 4.9 shows the EL spectrum at different bias from the devices made with sensor doped hole and electron transport layers.

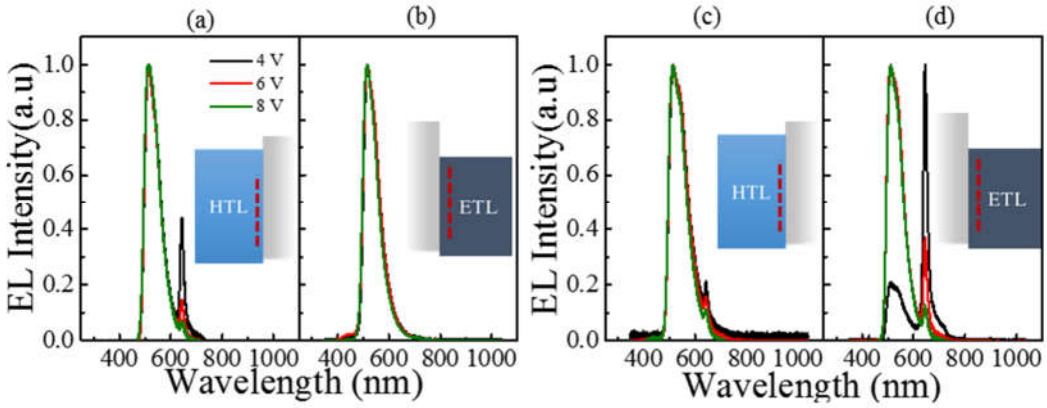

Figure 4.9 Role of Transport layers in device performance. Comparison of electroluminescence spectra obtained from doped hole and electron transport layer devices made with S-EML (E-host) (a,b) and S-EML (H-host) devices (c,d).

The EL spectra (Figure 4.9) clearly shows the presence of the sensor signal from the HTL layer in E-host devices. This result demonstrates the charge carrier leakage into transport layers if the RZ is pinned at the EML/transport layer interface. The absence of sensor signal from the ETL in the E-Host device indicates that the sensor signal observed from the HTL layer does not originate from long-range exciton transfer processes, as exciton transfer processes would be equally likely at both HTL and ETL interfaces. Conversely, in H-host devices, weak sensor emission observed from the HTL and strong sensor emission is observed from the ETL. Collectively, these observations explain that the charge leakage might be a key factor limiting the performance of OLEDs in this architecture.

4.4.5 Limitation of the Method

The sensor layer approach assumes that the EL spectra is proportional to the local triplet exciton density and all the generated triplet excitons are effectively utilized in the devices for light emission. It is important to note that at higher current densities exciton quenching processes such as triplet-triplet annihilation (TTA) and triplet-polaron annihilation (TPA) can play a role in the electroluminescence intensity of the devices made with an emitter that has a longer phosphorescent lifetime.[132] These quenching mechanisms strongly depend on the material properties such as frontier energy levels, triplet diffusion length and local exciton density in the devices. Since the host materials used in this study have higher triplet energy level (E-Host – 3.4 eV and H-Host – 3.3eV) and the dopants ($Ir(mppy)_3$- 3.0 eV and PtOEP – 3.4eV)[159], it is anticipated that the role of host-guest triplet quenching would be minimal in our study. Indeed, it has been reported previously that devices using $Ir(ppy)_3$ as a host, doped with low concentrations of PtOEP, have lower levels of TTA.[159-161] Considering the low current densities used to measure the EL, the dilute sensor concentration utilized, and the very weak long range transfer involved in the dopants

employed, the effect of TTA and TPA on the quantity Fsensor would likely be minimal in this study.

Another limitation would be the role of sensor on the overall charge transport and electrical performance of the devices. To use sensor layer to probe RZ zone, the sensor layer should not significantly affect the overall charge transport in the devices. In this study, the devices were fabricated with an extremely thin sensing layer (0.5 nm) with high photoluminescence efficiency. The variation of the *J-V* characteristics (Figure 4.10) and the turn on voltage (Figure 4.11) did not show any trend in the devices with and without sensing layer indicating that the sensor did not significantly affect the charge transport in our devices.

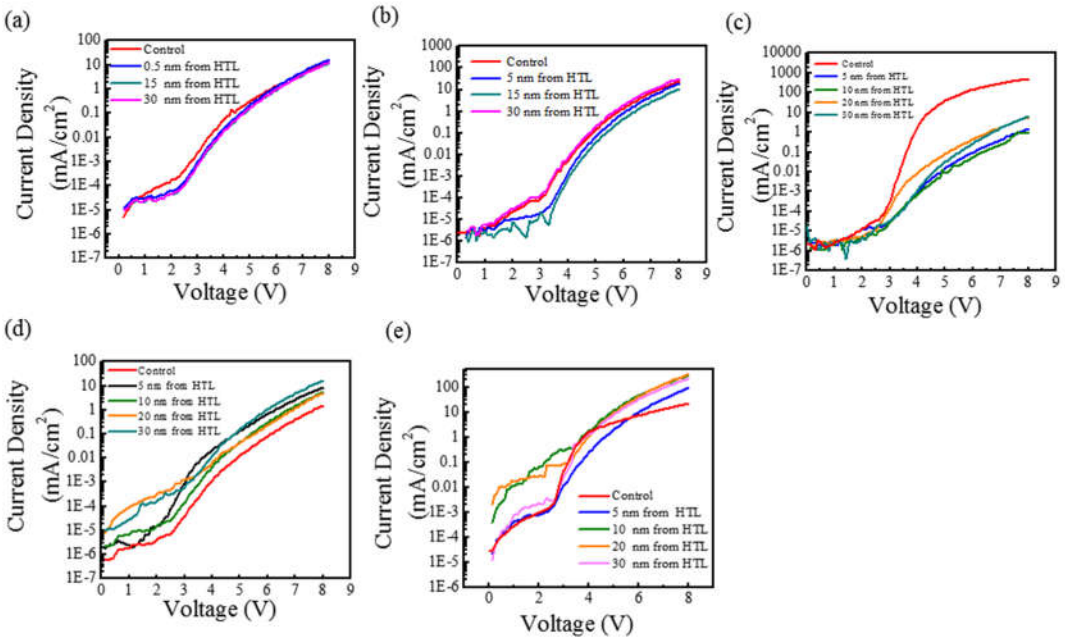

Figure 4.10 Current density comparison of device with sensing layers. Comparison of current density vs. voltage for the control devices (no sensing layer) with the devices made with sensing layer inserted at various position of a)S-EML (E-Host), b) S-EML(H-Host, c) D-EML(E-Host/H-Host) and d) D-EML(H-Host/E-Host) and (e) M-EML(E-Host:H-Host) devices

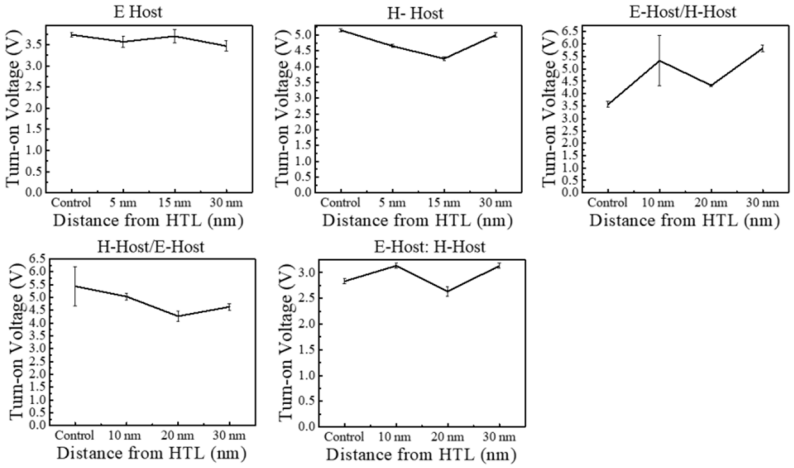

Figure 4.11 Comparison of turn on voltage of sensing layer devices. Turn on voltage measured at 1cd/m^2 brightness from the sensing layer positioned at different thickness of the emissive layer along with the control devices without the sensing layer

4.5 Conclusion

In summary, we have characterized the recombination profiles in various OLED architectures using an absolute EL sensor method. Changing the relative position of the embedded EL sensor provided insight into the recombination profile as well as the overall magnitude of recombination, carrier leakage, and bias dependence. We measured a range of recombination profiles for the E-host and the H-host S-EML devices. While the former had a recombination profile distributed throughout the emissive layer, the latter had the RZ pinned at the interface of the emissive and electron transport layers. Performance analysis indicates that devices with a broader recombination zone show lower EQE roll-off than devices that have the RZ pinned at the emissive and transport layer interfaces. Although the M-EML devices exhibited better optical turn-on and power efficiency metrics, devices suffered more significant EQE roll-off, possibly due to the narrow recombination zone widths. The unexpected RZ formation in M-EML devices highlights the need to further explore recombination profiles and carefully consider the impact of

relative energy levels (ΔHOMO and ΔLUMO) on carrier injection to rationally optimize complex OLED host configurations for high performance and high brightness.

Chapter 5 Phosphorescent Nanocluster Light Emitting Diodes

In this chapter, we demonstrate the first use of inorganic metal halide nanoclusters for application in OLEDs. These nanoclusters are abundant, inexpensive, and exhibit exceptionally high phosphorescent quantum yields that can lead to internal quantum efficiencies approaching 100%. Light emitting diodes are demonstrated with a range of core nanoclusters and nanocluster salts with varying cation substitution. External quantum efficiency of up to 2.5% for 800nm emission are demonstrated in an optically pumped device and 0.004% for an electrically pumped device. Based on luminescent transient dynamics and density functional theory (DFT) calculations we identify host quenching and exciton formation efficiency as key factors for improving electrically pumped devices. Theoretical calculations were performed to determine the nature of the phosphorescent emitting state in these nanoclusters, which involves a strong Pseudo Jahn Teller (PJT) distortion. We show with these initial demonstrations that these materials have a strong potential to replace organic phosphorescent molecules in both white and near-infrared light emitting diodes (LEDs) for low cost, and high efficiency applications, providing an exciting new paradigm of inorganic phosphorescent emitters.

5.1 Introduction

There has been growing interest in developing phosphorescent emitters without Pt and Ir (two of the least abundant materials on the planet) to enable their feasibility in low cost lighting applications while also pushing deeper into the near infrared for applications in electronics, telecommunications[162] and medical imaging.[163] To date, very few examples of phosphorescent emitters have been demonstrated for NIR emission [164] and no phosphorescent emitters are available for NIR emission without employing Pt and Ir. While various fluorescent

(ns) based emitters have been reported for near infrared light emitting diodes including rare earth lanthanides,[165, 166] organic fluorophore dyes,[167] low band gap polymers,[7, 168] colloidal quantum dots (mainly based on toxic Pb and Cd[169, 170]) Si,[171] $CuInS_2/ZnS$,[172] Au and Ag clusters,[173] and hybrid organic-inorganic perovskites [174] all suffer from the low overall potential of intrinsically limited internal quantum efficiencies.

To demonstrate a new platform of phosphorescent emitters with high abundance, high quantum yield, and the potential to span the visible and infrared spectral range, we have developed inorganic nanocluster emitters. These emitters are based on metal halide nanoclusters and nanocluster salts of the form M_6X_{12} and $A_2M_6X_{14}$, where M, X, and A are metal, halogen, and terminal cations, respectively. The distinctive structural differences between the core nanocluster, archetypical organic phosphors (e.g. fac-tris (2-phenylpyridine) iridium ($Ir(ppy)_3$) and semiconductor nanocrystals are highlighted in Figure 5.1.

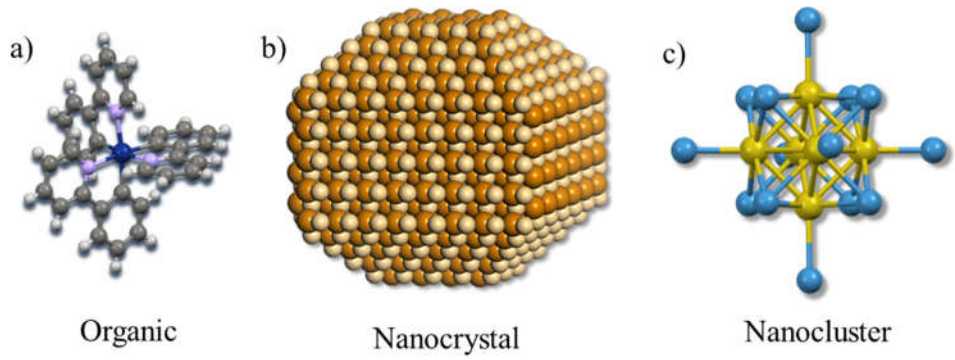

Figure 5.1 Nanocluster structure. Molecular structure comparison of archetypical A, phosphorescent organic molecule (e.g. fac-tris(2-phenylpyridine)iridium ($Ir(ppy)_3$) - blue atoms represent Ir, purple represent N atoms, dark grey represent C atoms, and light grey represent H atoms, B, nanocrystal (i.e. PbS), and C, hexanuclear metal halide nanoclusters (i.e. $(Mo_6Cl_{14})^{2-}$ where green atoms represent Mo^{2+} and blue atoms represent Cl^-).

We emphasize that nanocrystals are nanoscale crystalline ensembles of bulk semiconductors that allow for tunable properties through exciton confinement from diameter-control. However, these materials have also had challenges with stability due to an excess of dangling bonds and are highly sensitive to the diameter distribution that can change with parasitic reactions such as oxidation.[175] In contrast, nanoclusters are an inorganic molecular species, exactly defined in chemical composition and structure at the nanometer scale, analogous to organic molecules without organic bonding.

Among various nanoclusters, molybdenum halide nanoclusters are particularly interesting as they have a variety of structures[176] and their luminescence and phosphorescent properties have been exploited for oxygen sensor applications.[177] In earlier studies with these clusters, we outlined routes to achieving near-unity phosphorescent quantum yields, superior to those shown for colloidal quantum dot nanocrystals and NIR organic phosphors through cluster-cation-host interactions.[178] Here, we report the integration of molybdenum halide nanocluster salts into optically and electrically pumped nanocluster light emitting devices and demonstrate tunable emission by means of varying cation substitution. While the efficiency of the proof-of-principle electrically pumped devices are not fully optimized, optically pumped nanocluster device shows quantum efficiency of 2.5 % for peak emission at 800nm. We utilize both luminescent and electroluminescent transient dynamics to understand the nanocluster photophysics and analyze time-dependent density functional theory (TDDFT) calculations performed on the core cluster to gain insights about the nature of the phosphorescent emitting state. This demonstration of efficient inorganic nanocluster phosphorescence shows promising potential for developing this novel class of earth abundant and low-cost emitters for light emitting electronics and medical applications.

5.2 Experimental

5.2.1 *Synthesis of Mo_6Cl_{12} Nanocluster*

Molybdenum based nanoclusters are among the oldest known polynuclear clusters and were first reported in 1859.[179] Linus Pauling was actually the first to characterize the structure of these clusters and found that these clusters consist of octahedral Mo_6 units bearing eight face bridging inner halides and six terminal halides in the apical positions.[180] These apical halides are labile and can be readily switched to other ligands that can significantly improve the photochemical properties of the clusters.

Various procedures exist for synthesizing Mo_6Cl_{12}clusters. Nannelli et al developed a two-step procedure. In the first step, $MoCl_3$ is obtained from the reaction of $MoCl_5$ and Mo metal at 650° C. In the second step, dissociation of $MoCl_3$ at 650° C is carried out to yield Mo_6Cl_{12} and $MoCl_4$.[181] Dorman et al prepared Mo_6Cl_{12} in a single step by reducing $MoCl_5$ using Al at 200 ° C for 6 hours then at 450° C for 48 hours. The crude product is converted to chloromolybdic acid by treating with concentrated hydrochloric acid (HCl).[182] Koknat et al performed a reaction of $MoCl_5$ with Mo in the presence of NaCl at 720° C that resulted Mo_6Cl_{12}.[183] All these procedures require the use of quartz tubes as the temperature is not suitable for regular borosilicate glass and a substantial amount of time and labor is required to isolate the final product.

We adopted the procedure by Hay and used Bi as reductant as it is inexpensive and does not readily further reduce Mo_6Cl_{12} upon formation. Most importantly, it allowed the reaction displayed in the equation to be carried at lower temperature using a regular borosilicate glass tube. [184]

$$6MoCl_5 + 6Bi \rightarrow Mo_6Cl_{12} + 6BiCl_3 \quad (5.1)$$

Synthesis was carried out in a dual chamber (reaction chamber and receiver chamber) glass tube described in the Figure 5.2a, (8 cm length and 25 mm diameter) with a constriction between these chambers. A vacuum valve made of Teflon was attached to the receiver chamber to seal the tube upon loading in the glove box. The glass tube was then washed with acetone, oven dried at 200°C overnight, and cooled down under vacuum in the antechamber prior to loading the materials. The reactants $MoCl_5$ (99.6 % purity, Alfa Aesar) and bismuth powder (325 mesh, 99.5 % purity, Alfa Aesar) were used without any further purification. For a typical batch, 5 g of $MoCl_5$ and 3.825 g of Bi were mixed thoroughly using mortar and pestle and loaded into the end chamber of dual chamber tube using a long stem funnel in the glove box. It is important to keep the inner glass surface of tube free of contamination as it might affect the flame sealing process. The tube was closed, flame seal at the end of receiver chamber and placed horizontally in the tubular furnace. The temperature was ramped (125°C/hr.) to 250°C over 2 hours then to 375°C for 2 hours and maintained at 375°C for 60 hours. After 60 hours, the receiver chamber was moved out of furnace while heating was continued at 375°C for 12 hours. During this step, a white color byproduct $BiCl_3$ sublimed at the receiver chamber. After 12 hours, the furnace was cooled down and the products from the both chamber were homogenized by shaking multiple times and the ampule was placed inside the chamber with the receiver side of the ampule positioned out of furnace and heated to 350 °C for 2 hour and maintained at that temperature for 24 hours. The ampule was then cooled and broken at the constriction. A brown/olive green powders are collected from the reaction chamber.

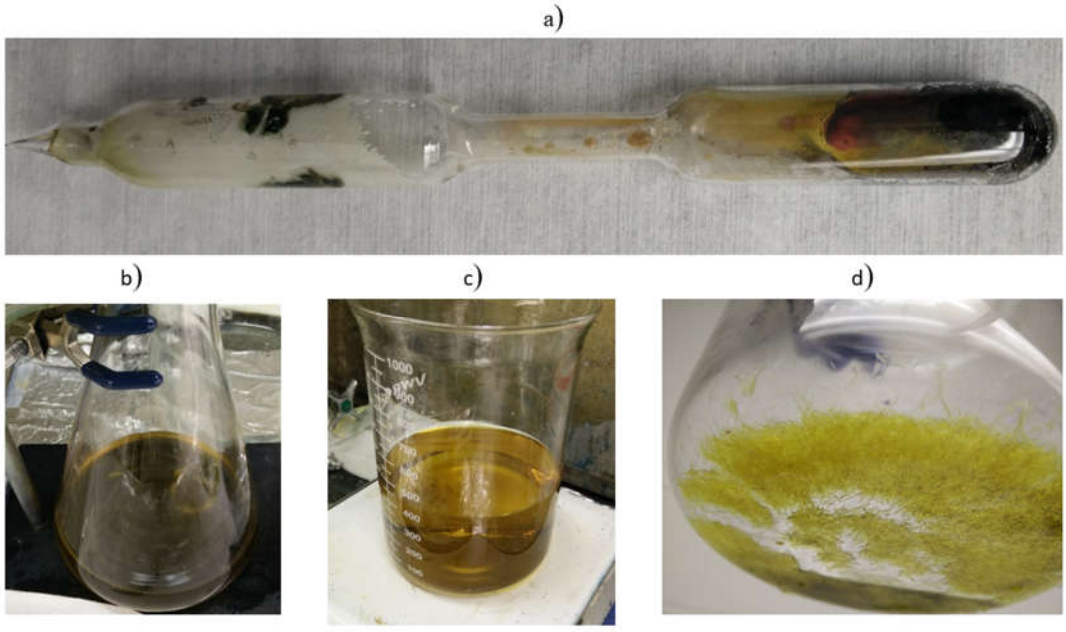

Figure 5.2 Synthesis of Mo_6Cl_{12} a) Double chamber tube used for the synthesis showing the product at the end chamber and the byproduct $BiCl_3$ at the receiver chamber b) Treatment of product in hot HCl c) filtrate that contains the dissolved Mo_6Cl_{12} d) Cooling down the solution in c) to yield crystals $(H_3O)_2[Mo_6(\mu_3 - Cl)_8Cl_6].6H_2O$

To isolate the Mo_6Cl_{12} , the brown and olive green powder obtained was then treated with 50 ml of hydrochloric acid in a 250 ml Erlenmeyer flask heated at 120 ° C for 6 hour with rapid stirring (Figure 5.2b) to completely dissolve the product according to equation

$$Mo_6Cl_{12} + 2HCl(aq) \rightarrow (H_3O)_2[Mo_6(\mu_3 - Cl)_8Cl_6].6H_2O \qquad (5.2)$$

The solution was filtered using medium porosity fritted glass funnel resulting yellow crystal of chloromolybdic acid and a black/grey unreacted Bi and $BiCl_3$. If the yellow crystals do not form during filtration, the solution might not be super saturated and the volume of solution needs to be reduced by evaporating the HCl. The yellow filtrate in the Figure 5.2 c was cooled down to room temperature and stored in the fridge overnight to produce more yellow/orange needle-like crystals. The solution was filtered using filter paper and crystals were dried in the desiccator upon P_2O_5 under vacuum for a day (Figure 5.2 d). To improve the purity of synthesized crystals, it is necessary to recrystallize the compound at least three times. For recrystallization, the yellow crystals were

re-dissolved in the hot HCl and the solution is filtered leaving the undissolved impurities in the filtrate. Filtered solution was then cooled to room temperature and eventually kept in the refrigerator for crystals growth.

5.2.2 Conversion of Chloromolybdic Acid to Mo_6Cl_{12}

Recrystallized samples of chloromolybdic acid were loaded in a small boat, positioned in the middle of a purification tube and heated slowly to 350°*C* over 2 hours under dynamic vacuum (1E-3 Torr) and maintained at 350°*C* for 24 hours resulting yellow/orange solid according to the equation 5.3,

$$(H_3O)_2[Mo_6Cl_{12}].6H_2O \rightarrow Mo_6Cl_{12} + 8H_2O + 2HCl \quad (5.3)$$

5.2.3 Synthesis of $(TBA)_2$ Mo_6 Cl_{14} and $K_2Mo_6Cl1_4$

Since Mo_6Cl_{12} can easily absorb moisture and exhibits color changes upon prolonged exposure to moisture, it is generally converted to more stable nanocluster salts. Tetrabutyl ammonium (TBA) salts of these clusters can be obtained by dissolving Mo_6Cl_{12} in 6 M HCl and adding tetrabutyl ammonium chloride in 1:2 molar ratio resulting immediate precipitation of the salt. The solution was filtered and the yellow precipitate was then dissolved in dichloromethane (DCM). Upon slow evaporation of the solvent, an orange color tetrabutylammonium salt of Mo_6Cl_{12} formed. A similar procedure can be used to synthesize potassium based salts in which KCl was added to the Mo_6Cl_{12} solution resulting in immediate precipitation. The precipitate was then dissolved in DCM, filtered and upon slow evaporation of solvent, orange crystals of $K_2Mo_6Cl_{14}$ formed. Alternatively, TBA and K based clusters can also be obtained using chloromolybdic acid as a starting material as described in the procedure.[185]

5.2.4 Device Fabrication

Patterned indium tin oxide (ITO) (20 ohm-sq.) substrates were degreased sequentially in soap, deionized water, and acetone for four minutes in a sonicating bath then rinsed in boiling isopropanol for four minutes followed by UV-ozone treatment. A 28 nm thick layer of poly(3,4-ethylenedioxythiophene):poly-(styrene sulfonate) (PEDOT-PSS) was spin-cast at 3000 rpm for 30 s onto the ITO as a hole-injection layer (HIL) and was annealed at 250°C for 30 min in a glovebox. A 37 nm hole transport layer of N, N′-Bis (3-methylphenyl)-N, N′-diphenylbenzidine (TPD) was spin-cast at 8000 rpm for 30 s using 5 mg/ml solution in chloroform. TPD films were cross-linked after spin coating by exposing to UV light (λ = 400 nm, 350 mW/cm^2) for 5 min. An emissive layer consists of 15 nm thick polyvinyl carbazole (PVK) and $(TBA)_2Mo_6Cl_{14}$ or $(H_3O)_2Mo_6Cl_{14}$ nanocluster. The mixture was spin-cast at 2000 rpm for 30 s using the ratio 1:0.1 by volume of PVK in chloroform (1.6 mg/ml) and nanocluster in toluene solutions (3 mg/ml) and baked at 110°C for 30 minutes in the glove box to remove the remaining solvent. A 30 nm thick electron transport layer (ETL) consisting of C_{60} and an 8.5 nm thick exciton blocking layer (EBL) consisting of bathocuproine (BCP) were subsequently thermally evaporated on the emissive layer at 3 x 10^{-6} Torr. A 100 nm thick Ag film was used as the cathode. Control devices were fabricated with an identical structure, but without the nanocluster to assure only nanocluster emission was observed. Electrically pumped devices were encapsulated using UV curable epoxy directly over the device.

Optically pumped devices were made from a commercially available UV diode with emission at 365 nm (Thorlabs), coated with a blended polymer film containing $(TBA)_2Mo_6Cl_{14}$. 4 mg of the $(TBA)^+$ nanocluster was dissolved in 1 ml of acetonitrile and 1 ml of poly (butyl methacrylate-co-methyl methacrylate. This blend solution was drop casted on a glass disk (0.5

inch dia.) and allowed to dry for 45 min under flowing nitrogen, then repeated seven times. The coated glass disc was positioned over the UV diode with a parabolic reflector.

5.2.5 Optical Characterization

Blended films consisting of PVK and $(TBA)_2Mo_6Cl_{14}$ or $(H_3O)_2Mo_6Cl_{14}$ nanoclusters were made by spin-casting a mixture (1:1) by volume of PVK in chloroform (16 mg/ml) and nanocluster in toluene solutions (3 mg/ml) at 2000 rpm for 30 s. The PL spectra and PL quantum yield of the blend films were measured using a PTI Quanta Master 40 spectroflurometer with excitation at 320 nm under nitrogen atmosphere. A 550 nm long pass filter was used for the PL measurement to prevent wavelength doubling. EL spectra of the electrically pumped devices were also measured using PTI Quanta Master 40 spectroflurometer.

5.2.6 Single Crystal Refinement

For single crystal XRD studies, yellow plate crystals were grown from solution with dimensions 0.40 x 0.37 x 0.17 mm and mounted on a nylon loop using very small amount of paratone oil. Data were collected using a Bruker CCD (charge coupled device) based diffractometer equipped with an Oxford Cryostream low-temperature apparatus operating at 173 K. Data were measured using omega and phi scans of 0.5° per frame for 5 s. The total number of images were based on results from the program COSMO where redundancy was expected to be 4.0 and completeness of 100% out to 0.83 Å. Cell parameters were retrieved using APEX II software and refined using SAINT on all observed reflections. Data reduction was performed using the SAINT software which corrects for Lp. Scaling and absorption corrections were applied using SADABS[186] multi-scan technique, supplied by George Sheldrick. The structures are solved by the direct method using the SHELXS-97 program and refined by least squares method on F2, SHELXL- 97[187], which are incorporated in OLEX2.[188] The structure of (TBA+) nanocluster

was solved in the space group P21/c (# 14) and the lattice constants were found (a = 22.3 Å, b = 11.7 Å, c = 22.3 Å). All non-hydrogen atoms are refined anisotropically. The structure of (H_3O+) nanocluster was solved in the space group C2/c (# 15) and the lattice constants were found (a = 17.3 Å, b = 9.1 Å, c = 18.5 Å). Hydrogens were calculated by geometrical methods and refined as a riding model for both clusters. The crystal used for the diffraction study showed no decomposition during data collection.

5.2.7 Electronic Structure Calculations

To understand the excited states in these nanoclusters, time-dependent density function theory calculations[189, 190] (TDDFT) were performed on isolated (Mo6Cl14)2- clusters. The ground state (S0) and first excited triplet state (T1) structures were optimized with the CAM-B3LYP functional[191] and LANL2DZ basis set and effective core potentials.[192] A larger basis created by adding polarization functions to the LANL2DZ basis set (f and d functions with ζ values of 1.043 and 0.750 on Mo and Cl, respectively) was employed to compute all reported energies. All calculations were done with the Q-Chem software package.[193] The computed absorption energy (2.72 eV) is in excellent agreement with the experimental absorption (2.74 eV) seen from higher thickness films of nanoclusters. The computed emission energy (1.32 eV) is slightly red shifted to the actual emission energy (1.64 eV) seen from both nanocluster devices. This small discrepancy is not unexpected given the facts that the surroundings (including counter ions) are neglected in these calculations and strong correlation effects in the ground state are not accounted for at the CAM-B3LYP level of theory. Calculations on the counterions were performed at the B3LYP level of theory[194, 195] with the 6-31+G* basis. Vertical electron affinities are computed as the difference between the computed energy of the cationic state and the neutral state at the optimized geometry of the cation.

Analysis of the natural transition orbitals (NTOs) for the highest singlet excited state (S_{24}) , absorbing lowest singlet (S_1), and emitting states (T_1) indicates large changes in the electronic structure associated with the various relaxation processes. S_{24} is of d-d character and delocalized over all of the metal centers. The S_{24} state is well described by a single electron excitation between the dominant NTO pair (amplitude 0.92, pictured in Figure 5.6, top right). Upon relaxation to S_1 the excitation is still of delocalized d-d character, but strong electron-hole correlation emerges, as indicated by the fact that the five most dominant NTO pairs are all of similar amplitude (0.38-0.53). The T_1 state has a similar strongly correlated d-d character at the S_0 minimum, but upon PJT relaxation the triplet excitation localizes to the most distorted metal center. There is a dramatic decrease in the degree of strong electron correlation, indicated by the emergence of a single dominant NTO pair with an amplitude greater than 0.99.

5.3 Results

The syntheses of the various nanoclusters are described in chapter 3. Both electrically and optically pumped light emitting devices were fabricated for two particular molybdenum (II) chloride nanocluster salts: $(H_3O)_2Mo_6Cl_{14}$ and $((C_4H_9)_4N)_2Mo_6Cl_{14}$. Optical characterization was performed on thin blended films of the hydronium $(H_3O)^+$ and tetrabutylammonium $(TBA)^+$ substituted hexanuclear molybdenum chloride nanoclusters. The results show that both of these nanoclusters exhibit similar photoluminescence (PL) emission centered at $\lambda = 750$ nm. PL quantum yields (QY) (Φ) of 16±2% and 45±1% were measured for $(H_3O)^+$ and$(TBA)^+$ nanoclusters in polyvinyl carbazole (PVK) blend films respectively. Interestingly, we note that the QY of the $(TBA)^+$ nanocluster is dramatically enhanced to >70% in a poly (butyl methacrylate-co-methyl methacrylate (PBMMA) highlighting the impact of host interactions on the luminescence properties of the nanoclusters. To demonstrate the application of nanoclusters as efficient emitters,

and to understand the role of cations in electroluminescence (EL), electrically pumped devices were fabricated employing $(H_3O)^+$ and $(TBA)^+$ substituted nanocluster using the device architecture shown in (Figure 5.3a).

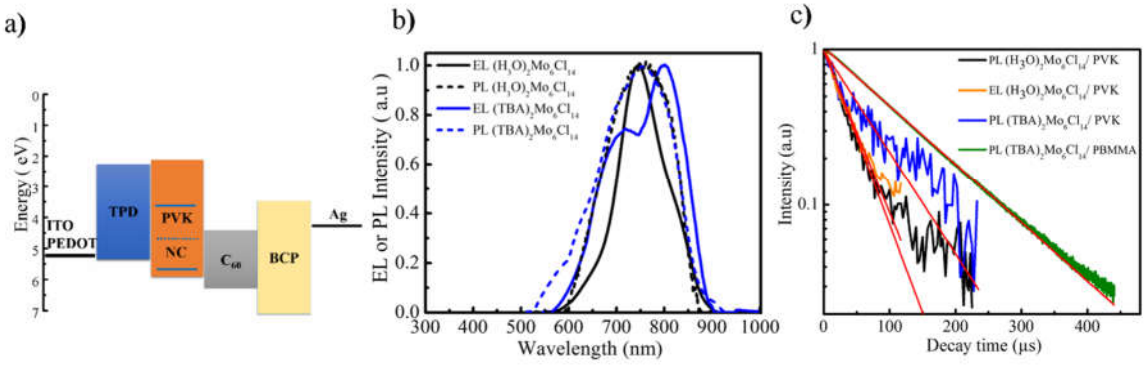

Figure 5.3 Nanocluster luminescence. a), NCLED device architecture. b) Comparison of the photoluminescence (dashed lines) and electroluminescence (solid lines) spectra of electrically pumped devices with $(H_3O)^+$ (black) and $(TBA)^+$ (blue) nanocluster salts. Inset shows schematic energy level diagram of the typical device architecture under flatband conditions where energy levels were obtained from literature or measured directly.[171, 196, 197] b, The PL transient response of $(H_3O)^+$ nanocluster (black) and $(TBA)^+$ nanocluster (blue) films in a PVK matrix, $(TBA)^+$ nanocluster (dark yellow) in a PBMMA matrix, and the EL transient response of electrically pumped $(H_3O)^+$ nanocluster device (green)

Additionally, we developed an optically pumped device in which an ultraviolet LED is coupled to the $(TBA)^+$ nanocluster/PBMMA film to efficiently produce NIR emission. In Figure 5.3b we compare the electroluminescence (EL) spectra for the devices with the PL spectra of $(H_3O)^+$ and $(TBA)^+$ nanocluster blended films. We note that the EL spectrum of the $(H_3O)^+$ nanocluster device peaks at 750 nm, in agreement with the PL spectrum. However, the EL spectrum for the $(TBA)^+$ nanocluster device is red shifted by approximately 40nm from its PL spectrum. To understand the origin of the luminescence, we measured the luminescent lifetime of the nanoclusters with transient PL decay. Figure 5.3c shows the transient PL response observed for the $(H_3O)^+$ and $(TBA)^+$ nanoclusters in PVK films and $(TBA)^+$ nanocluster in PBMMA films, as well as the EL transient decay for an electrically pumped $(H_3O)^+$ nanocluster device. Natural

luminescent lifetimes of 37±10 μs and 68±12 μs were obtained for the $(H_3O)^+$ and $(TBA)^+$ nanoclusters in PVK matrix respectively, while a lifetime of 138±38 μs was measured for the $(TBA)^+$ nanocluster in PBMMA host, similar to what has been measured previously in acetonitrile solutions.[198] While we were unable to measure transient of the $(TBA)^+$ nanocluster EL due to the low intensity, an EL lifetime of 28±3 μs was measured for the electrically pumped $(H_3O)^+$ nanocluster devices confirming electrophosphoresence. Figure 5.4a shows a comparison of current density (*J*) and luminescence current density (*L*) versus voltage (*V*) of the electrically pumped devices.

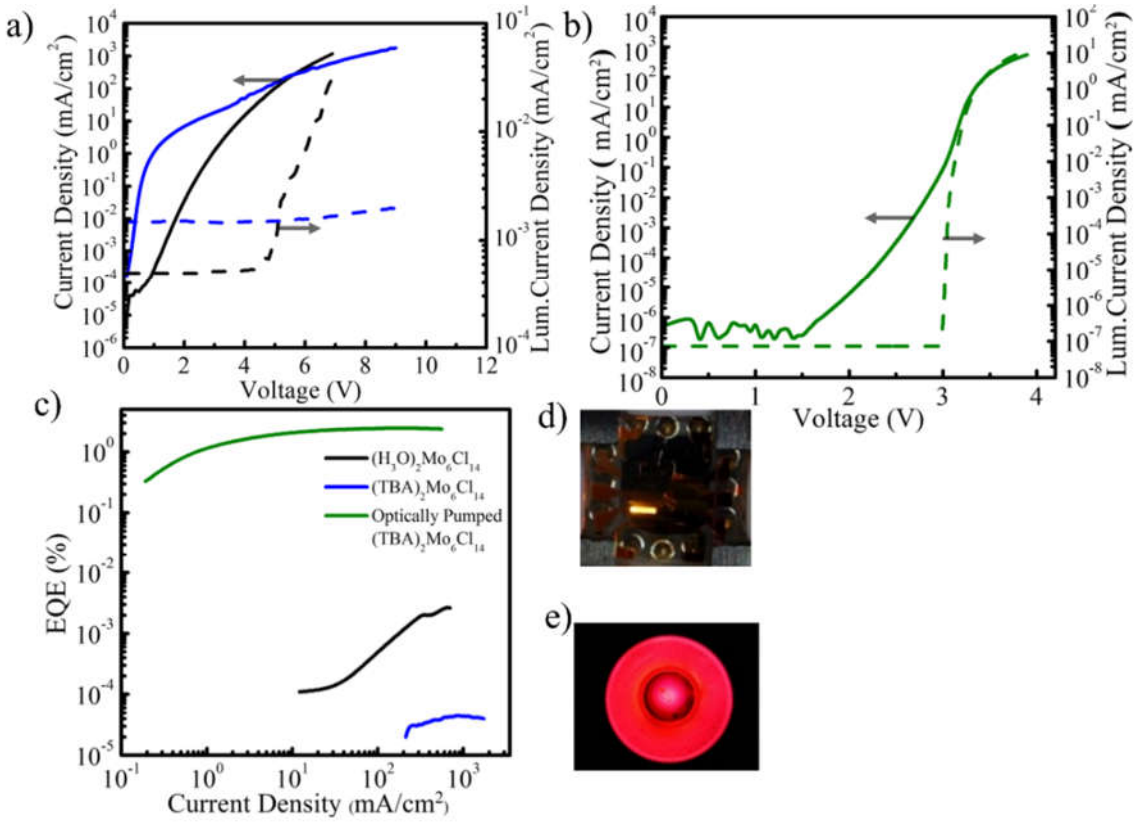

Figure 5.4 Nanocluster device performance. a), Current density, J, (solid lines) and luminescence current density, L, (dashed lines) versus voltage (V) curves for $(H_3O)^+$ (black) and $(TBA)^+$ (blue) electrically pumped devices. b), J-V (solid olive green line) and L-V (dashed olive green line) curves for optically pumped device. c), Comparison of EQE for the $(H_3O)^+$ (black) and $(TBA)^+$ (blue) nanocluster devices as well the optically pumped $(TBA)^+$ nanocluster devices (olive green). Note that the legend in Figure 3c applies for Figure 3a and 3b. D, Images of an

electrically pumped device fabricated using $(TBA)^+$ nanocluster (d) and optically pumped device fabricated with $(TBA)^+$ nanocluster (e)

The $(TBA)^+$ nanocluster device exhibit higher current densities and lower luminescence current densities than the $(H_3O)^+$ nanocluster device while both devices exhibit electrical turn on at 1.1 V and optical turn on at 4.5 V. Figure 5.4b shows *J-V-L* characterization of the optically pumped device, which has an optical turn on at 3.0 V. External quantum efficiencies (EQE) for the electrically and optically pumped devices are shown in (Figure 5.4c) where the maximum EQEs of (4.4±0.07) x 10^{-3}% and (5.0±0.1) x 10^{-5}% were obtained for electrically pumped $(H_3O)^+$ and $(TBA)^+$ nanocluster devices respectively, and a maximum EQE of 2.5±0.1% was demonstrated for the optically pumped $(TBA)^+$ device

To understand the dramatic variation in performance with cation substitution and to characterize the structure of the metal halide salts, single crystal structures were solved and used to determine the cation arrangement around the nanocluster as shown in Figure 5.5

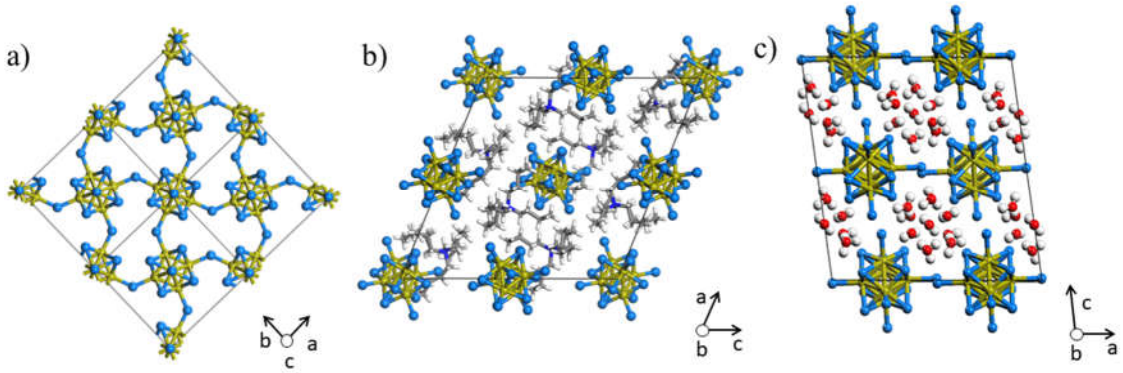

Figure 5.5 Nanocluster crystal structures a), Crystal structures for the $(TBA)^+$ nanocluster and B, $(H_3O)^+$ nanocluster. $MoCl_2$ representing packing along the c axis b) $(TBA)_2$ Mo_6Cl_{14} and c), $(H_3O)_2$ Mo_6Cl_{14} representing packing along the b axis

Density Functional Theory (DFT) calculations were performed to investigate the role of cations on the injection characteristics of the electrically pumped devices. Comparison of electron affinities of $(H_3O)^+$ and $(TBA)^+$ demonstrates that the barrier to tunneling of the electron through

$(TBA)^+$ is not only wider (due to the bulk of this counterion), but also significantly higher in energy than that of $(H_3O)^+$. TDDFT calculations were performed to understand the excited state properties of the nanoclusters. Figure 5.6 shows the schematic diagram of the optical excited state processes and the natural transition orbitals involved in the core nanocluster.

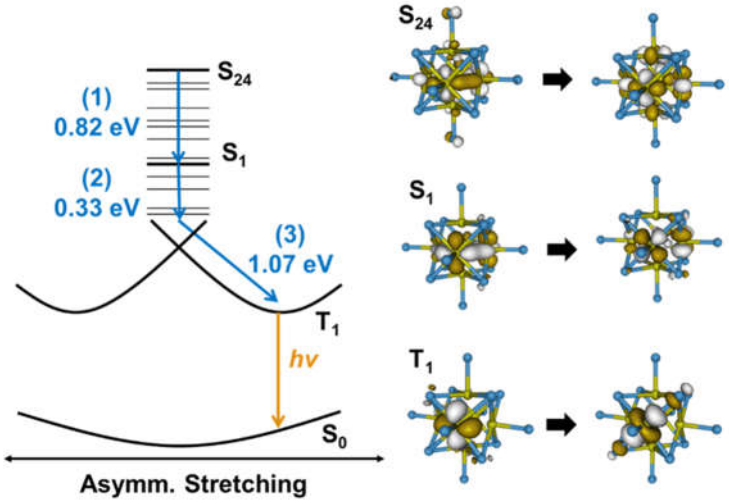

Figure 5.6 Theoretical relaxation processes in the nanoclusters. Schematic diagram showing the three relaxation processes with the energy contribution of each process computed at the TDDFT level of theory. (right) The largest amplitude NTO pair associated with S_{24} (top) and S_1 (middle) at the S_0 minimum structure, and that of T_1 at the T_1 relaxed structure (bottom).

5.4 Discussion

Optically pumped light emitting devices were fabricated to highlight the high PL efficiency of $(TBA)^+$ nanoclusters / PBMMA blend film. The EQE for the optically pumped device can be understood by the equation: $\eta_{ext-NC} = \eta_{ext} * \eta_A * \phi * \eta_{out}$, where η_{ext-NC} and η_{ext} is the EQE of the pumped devices and underlying UV diode (13±0.7%), η_A is the nanocluster absorption (95%), ϕ is PL quantum yield of $(TBA)^+$ nanoclusters/PBMMA film and η_{out} is the Outcoupling efficiency of the ensemble optical device. The $((TBA)^+$ nanoclusters/ PBMMA blend film showed PL quantum yield of > 70 % at λ= 320 nm excitation. However, at λ= 365 nm excitation (emitting wavelength of UV diode), the blend film showed PL quantum yield of 26%. The maximum

measured EQE of 2.5±0.1% in the optically pumped device suggests that there is roughly 22% loss in outcoupling in this configuration. To demonstrate electrophosphoresence from these hexanuclear molybdenum chloride nanocluster NIR emitters, electrically pumped devices were fabricated utilizing $(TBA)^+$ and $(H_3O)^+$ substituted nanoclusters in a thin PVK host. The absence of electroluminescence from the control devices confirms that the excitons are directly created on, and emitted from, the nanoclusters. The photophysical properties of nanoclusters in PVK and PBMMA matrix and the maximum EQE of electrically pumped devices are listed in Table 5.1.

Table 5.1 Photophysical data for $(H_3O)^+$ and $(TBA)^+$ nanoclusters blend films and the external quantum efficiency of electrically and optically pumped devices.

Cluster/Host	QY (%)	Lifetime (µs)	K_r (s^{-1})	K_{nr} (s^{-1})	Max EQE (%)
$(H_3O)_2Mo_6Cl_{14}$/PVK	16±2	37±10	5.0×10^3	26×10^3	$4.4\pm0.07 \times 10^{-3}$
$(TBA)_2Mo_6Cl_{14}$/PVK	45±1	68±2	7.2×10^3	8.8×10^3	$5.0\pm0.1 \times 10^{-5}$
$(TBA)_2Mo_6Cl_{14}$/PBMMA	70±4	138±38	6.1×10^3	2.6×10^3	2.5±0.1

[a] K_r – Radiative rate, K_{nr} - Non-radiative rate

5.4.1 Role of Guest-Host Interaction

The electrical device architecture is clearly not yet optimal comparing the emitted photon energy (~1.6 eV) to the optical turn on voltage (4.5 V). The EQEs of the electrically pumped devices are low compared to the expected values when the photoluminescence quantum efficiency of these nanoclusters and their phosphorescent nature are considered. To explain this non-ideal behavior, we turn to PL lifetime measurements. We find from these measurements that the lower EQE in the electrically pumped devices is partly due to the interactions between the host and the

nanocluster, which leads to quenching of excitons on the nanocluster. In contrast with the PL efficiency of the $(TBA)^+$ nanocluster, the EQE for the electrically pumped $(TBA)^+$ nanocluster is surprisingly lower than that of the $(H_3O)^+$ nanocluster. We estimate the radiative (K_r) and non-radiative decay rates (K_{nr}) from the QY and luminescence lifetime data for both nanoclusters. Based on this data, we can eliminate non-radiative quenching as the factor causing the lower than anticipated EQE in electrically pumped $(TBA)^+$ nanocluster devices as the non-radiative rate for $(TBA)^+$ nanocluster is an order of magnitude lower than $(H_3O)^+$ nanocluster in PVK.

To understand this unexpected trend we turn to the molecular arrangement of the cationic species around the core cluster. Analysis of XRD data reveals that while both cations are positioned around the core cluster, the $(TBA)^+$ cation provides a cage-like structure wrapped around cluster whereas the $(H_3O)^+$ cation covers only a smaller area. Various studies have pointed to the role of cations and surface ligands on photoluminescence and charge transport in colloidal nanocrystals.[199, 200] Thus, while the cage like arrangement of $(TBA)^+$ cations act to enhance the quantum yield of optical excitation by minimizing cluster-host and cluster-cluster interactions, it can also impede the charge transport into the nanoclusters. Interestingly, the $(TBA)^+$ nanocluster concentration dependence of quantum yield suggests that although the bulky cations minimize cluster-cluster interactions, they still allow for electronic interaction between nanocluster and the host. We have performed density functional calculations to investigate the barrier to an electron passing through the counterions. Electron affinities of 1.9 and 4.8 eV are found for electron attachment to the $(TBA)^+$ and $(H_3O)^+$ counterions, respectively, suggesting that the energetic barrier to transport through $(TBA)^+$ is dramatically higher than that of $(H_3O)^+$. Additionally, considering that (1) the $(TBA)^+$ counterion is much bulkier than $(H_3O)^+$ and (2) the rate of tunneling decays exponentially with distance, it is clear that the rate of tunneling from the

nanocluster through the counterions will be considerably faster for $(H_3O)^+$. We propose this tunneling barrier prevents efficient injection of carriers to luminescent core thus reducing the exciton formation efficiency and consequently lowering the quantum efficiency in the $(TBA)^+$ nanocluster devices compared with $(H_3O)^+$ nanoclusters devices. Thus, there is a sensitive interplay between minimizing the nanocluster-nanocluster and nanocluster-host interactions to maximize the quantum yield, while also allowing for efficient charge generation to maximize the quantum efficiency.

5.4.2 Role of Cation Arrangement

Typically, the efficiency of phosphorescent OLEDs drops off at high current and brightness. Several studies have shown that a lack of charge balance at lower current density and exciton quenching at higher current densities can be the dominant factors causing the EQE roll off in phosphorescent OLED devices.[69] However, in this case we do not observe significant EQE roll off from any of the devices, suggesting that exciton-exciton annihilation is not yet present. The exciton generation rate per molecule can be approximated by multiplying the maximum EQE of the pumped devices and with the corresponding current density. From this, we estimate the upper bounds rate of exciton generation of $4.5x10^2$ excitons/nanocluster-s in the optically pumped device. For the electrically pumped $(H_3O)^+$ nanocluster and $(TBA)^+$ nanocluster devices we estimate a rate of 85 excitons/nanocluster-s and 1.76 excitons/nanoclusters-s respectively, well below the limiting rate from the optical device. This analysis therefore suggests that these nanoclusters are capable of producing a large number of excited states and high brightness without exciton-exciton interactions up to current density of at least 6.3 A cm^{-2} and 210 A cm^{-2} in the $(H_3O)^+$ and $(TBA)^+$ nanocluster devices respectively.

5.4.3 Pseudo Jahn-Teller Distortion

To understand the fundamental excited states generated during optical excitation which are responsible for the photophysical properties of these nanoclusters, we performed theoretical calculations at the TDDFT level. We have identified the following excited state processes illustrated in Figure 5.6: (1) upon optical excitation to the lowest bright excited state (S_{24} in our calculations) electronic relaxation occurs to the lowest singlet excited state (S_1) occurs, lowering the energy by 0.82 eV (2) electronic relaxation within the singlet manifold is followed by intersystem crossing to the triplet manifold, with the lowest triplet excited state (T_1) falling 0.33 eV below S_1 at the Franck-Condon geometry, and (3) pseudo-Jahn-Teller (PJT) distortion on the lowest triplet state results in an additional 1.07 eV of relaxation. The relaxation energy on T_1 is the result of the high symmetry of the clusters, which is broken both globally and locally during PJT distortion. Analysis of the natural transition orbitals[201] (NTOs) from these TDDFT calculations indicates strong excitonic correlation effects in the S_1 and T_1 wave functions at the Franck-Condon point, that are relieved upon PJT relaxation. The unusually large energy associated with this geometric distortion explains both the broad emission band observed experimentally and suggests strategies for photophysical manipulation through asymmetrical modifications.

5.5 Conclusion

In summary, we have demonstrated luminescent devices utilizing an entirely new class of inorganic phosphorescent emitters based on metal halide nanocluster salts. Cation substitution is shown to strongly impact the electroluminescent efficiency and spectral properties of Mo-Cl based nanoclusters. Although the optically pumped devices fabricated from $(TBA)^+$ nanoclusters show NIR emission with a peak EQE of 2.5%, electrically pumped devices are found to be highly sensitive to host-guest interactions and exciton formation is pinpointed as the key limitation due

to cation arrangement in the nanoclusters that impacts tunneling and recombination dynamics. TDDFT calculations show that Pseudo Jahn Teller (PJT) distortion is operative in the phosphorescent emitting state of these nanoclusters. The high efficiency of the optically pumped device and the demonstration of electrically pumped devices employing these nanoclusters expands the catalogue for NIR phosphors that can be utilized in OLEDs and provides a new pathway for developing a unique class of inorganic phosphors for efficient and tunable electroluminescent device.

Chapter 6 Enhanced Electroluminescence Efficiency in Nanocluster Light Emitting Diodes through Apical Ligand Exchange

In this chapter, we report the application of molybdenum iodide nanocluster derivatives in highly efficient NCLEDs. Tunable emission in the devices is demonstrated by changing the apical ligands in the nanoclusters with a maximum external quantum efficiency > 1%. Improved electroluminescence efficiency (from 0.004% for Mo_6Cl_{14} demonstrated in the previous chapter) is shown to result from the combination of enhanced photoluminescence, carrier injection and recombination efficiencies in the heavier apical ligand substituted nanoclusters when paired with optimal hosts. These results highlight the promising potential of $[Mo_6I_{14}]^{2-}$ based nanoclusters for LEDs applications in the visible and near-infrared.

6.1 Introduction

Nanocluster light emitting diodes (NCLEDs) consisting of Ag or Au nanocluster have been reported with a maximum EQE of 0.1 %.[202] The lower efficiency in these devices is due to the poor exciton confinement and the florescent nature of these emitters.[173] Recently, Cu iodide based organic clusters with dual emissive characteristics have been reported. Despite lower photoluminescence efficiency, the devices showed peak EQE of 0.74 %.[203]

As an alternative to expensive metal NCs, we reported the integration of phosphorescent metal halide nanoclusters and nanocluster salts into optically and electrically pumped NCLEDs in Chapter 5.[204] Mo based nanoclusters consist of octahedral Mo_6 units bearing eight face bridging inner halides and six terminal halides in the apical positions.[180] These apical halides are labile and can be readily substituted to other ligands to significantly improve the photochemical properties of these clusters to make them attractive candidates for applications in catalysis,[205, 206] radiochemistry,[207] sensors,[177] intercalation chemistry,[208] and solar

concentrators.[178] In addition, switching the inner halides from chloride to iodide has also led to improvement in the photoluminescence properties of these nanoclusters. For example, $(TBA)_2[(Mo_6I_8)(C_3F_7COO)_6]$ and $(TBA)_2[(Mo_6I_8)(CF_3COO)_6]$ were shown to have phosphorescence quantum yields (PLQY) of 1.0 in oxygen free dry solvents,[209, 210] while the parent nanoclusters Mo_6Cl_{12} and Mo_6I_{12} have PLQY < 0.05 indicating the major role of apical ligands on the photoluminescence properties of these nanoclusters.

6.2 **Experimental**

6.2.1 Synthesis of Mo_6I_{12}

Double chamber quartz tube used for synthesizing Mo_6Cl_{12} were similarly used in this synthesis as well. In a typical batch, 1.0 g of MoI_3 (Chempur-Germany) was loaded into the end section of the dual chamber ampule inside the glove box. The ampule was flame sealed after pulling vacuum, laid flat in the tubular furnace and heated by setting the zone 1, 2, and 3 temperatures to O°C, 680 °C and 750 °C for 72 hours with a heating and cooling rate of 2°C/min. The reaction was carried out according to the equation 6.1. At the end of 72 hours, a red powder of Mo_6I_{12} is obtained along with the excess of iodine/starting material sublimed at the end of the tube as black crystals (Figure 6.1)

$$2MoI_3 \rightarrow 2\,MoI_2 + I_2 \tag{6.1}$$

6.2.2 Synthesis of $Cs_2Mo_6I_{14}$

The solubility of Mo_6I_{12} in common organic solvents is very limited; hence, Mo_6I_{12} was converted to $Cs_2Mo_6I_{14}$ and used as a precursor for the subsequent ligand exchange reaction.

$$6MoI_2 + 2\,CsI \rightarrow Cs_2Mo_6\,I_{14} \tag{6.2}$$

We adopted the procedure by Kiracki et al. In a typical reaction, 700 mg Mo_6I_{12} was thoroughly mixed with 173 mg of CsI (Sigma Aldrich) using a mortar and pestle and filled in a

single chamber 8 cm quartz ampule. The ampule was flame sealed under vacuum, placed in a furnace, and heated to 700 °C for 72 h with a heating and cooling rate of 2°C /min. resulting in a black/grey solid (Figure 6.1b). The ampule was opened in glove box, and the black solid was ground to reveal a burgundy colored $Cs_2Mo_6\ I_{14}$ powder. (Figure 6.1c)

6.2.3 Synthesis of $Cs_2Mo_6I_8(C_3F_5OO)_6$

In a typical procedure, 0.230 mg of $Cs_2Mo_6I_{14}$ was dissolved in 20 ml of dry, oxygen free acetone by stirring overnight at room temperature. Simultaneously, 0.245 mg of $Ag(C_2F_5OO)$ salt was dissolved in the dry, oxygen free acetone. Two solutions were mixed in a glove box or transferred using cannula to a Schlenk flask and stirred for 48 hours in dark at room temperature under argon (Figure 6.1d). After 48 hours, the mixture was filtered through a celite pad and orange/red solution was evaporated to dryness and stored in the glove box.

$$Cs_2Mo_6\ I_{14} + 6\ Ag(C_2F_5COO) \rightarrow Cs_2Mo_6\ I_8(C_2F_5COO)_6 + 6\ AgI \qquad (6.3)$$

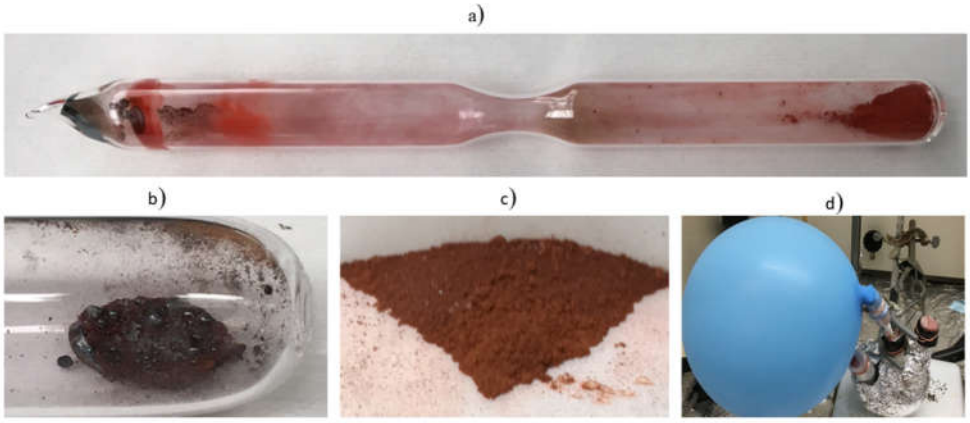

Figure 6.1 Synthesis of Mo-I clusters a) Double chamber quartz tube showing the product Mo_6I_{12} at the end chamber and unreacted reactant in the edge of the receiver chamber b) Black rock like $Cs_2Mo_6I_{14}$ c) Grinding the black rock revealed the burgundy color $Cs_2Mo_6I_{14}$ d) Set up used for performing ligand $(C_3F_5OO)_6^-$exchange in dark under Ar atmosphere.

6.2.4 Device Fabrication

Patterned indium tin oxide (ITO) (20 ohm-sq.) substrates were cleaned sequentially in soap, deionized water, and acetone for three minutes in a sonicating bath then rinsed in boiling

isopropanol for three minutes followed by UV-ozone treatment. A 40 nm thick layer of poly(3,4-ethylenedioxythiophene): poly-(styrene sulfonate) (PEDOT:PSS) was spin-cast at 6000 rpm for 30 s onto the ITO as a hole-injection layer (HIL) and was annealed at 125°C for 30 min. We adopted a guest/host architecture to fabricate the emissive layer in the NCLEDs. A range of hosts were surveyed as potential hosts for nanoclusters by testing their suitability in devices with 10 % nanocluster doping concentration including 3-bis(N-carbazolyl)benzene (mcp), 1,3-bis(triphenylsilyl)benzene (UGH-3), and 2,6-di(9H-carbazol-9-yl) pyridine) (Pyd-2Cz). While the devices made with mcp show a combination of nanocluster emission along with significant host emission, no nanocluster emission was observed from the UGH-3 devices. Pyd-2Cz devices were found to show nearly pure emission from the nanocluster with only small contributions from the host. Consequently, Pyd-2Cz was selected for further device optimization. An emissive layer (EML) consisting of 12-85 nm thick host matrix (Pyd-2Cz) doped with (2 wt.% - 15 wt. %) of nanoclusters was spin-cast at 3000 rpm for 30 s from a mixture of host and nanocluster dissolved separately in chlorobenzene and dry acetone. The EML was then heated at 70°C for 10 minutes in the glove box to remove the remaining solvent before substrates were loaded into an evaporation chamber. A 10 nm thick hole blocking layer (HBL) consisting of bis[2-(diphenylphosphino)phenyl] ether oxide (DPEPO), and an electron transport layer (ETL) 40 nm of 2,2′,2"-(1,3,5-benzinetriyl)-tris(1-phenyl-1-H-benzimidazole) (TpBi) were subsequently thermally evaporated on the emissive layer at 3 × 10-6 Torr. A LiF (0.8nm)/Al (80 nm) cathode film was evaporated over the ETL. Control devices were fabricated without the nanocluster in the emissive layer for comparison.

6.3 Results

6.3.1 Materials Characterization

X-ray powder diffraction, ^{19}F-NMR in acetone-d6, and mass spectrometry techniques were used to confirm the identity of the products. Figure 6.2 show powder diffraction patterns of Mo_6I_{12} and Figure 6.3 display the XRD pattern of $Cs_2Mo_6I_{14}$ .The pattern were found to be identical to the reported literature for these compounds.[211].

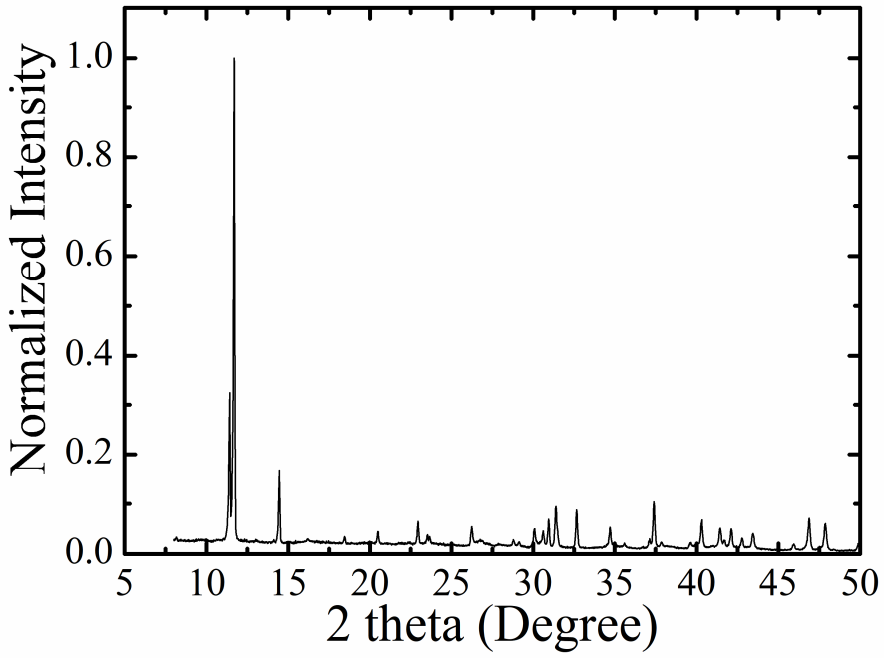

Figure 6.2 X-ray diffraction pattern of as synthesized Mo_6I_{12}

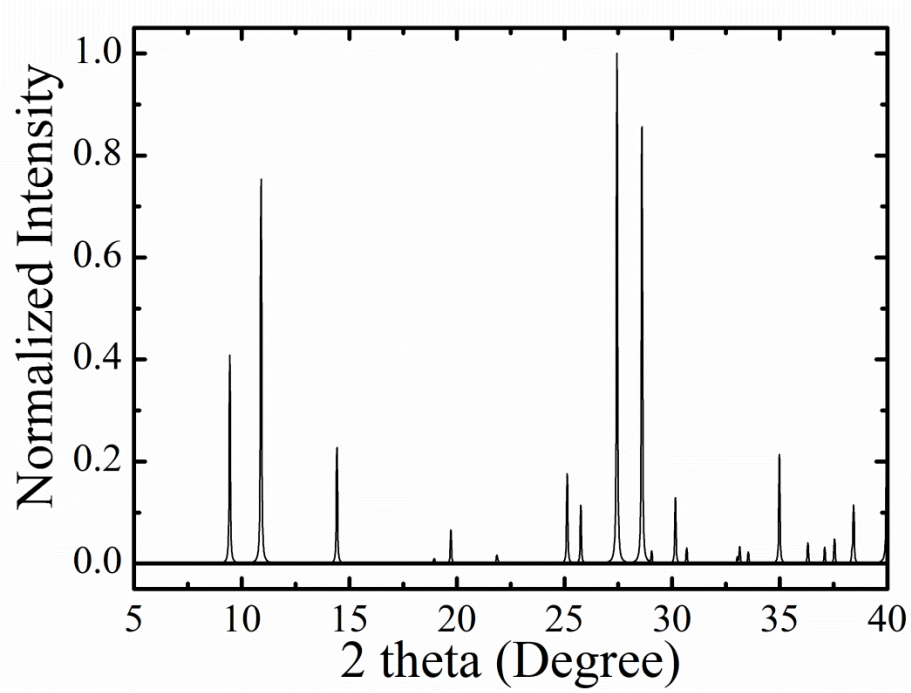

Figure 6.3 XRD pattern of $Cs_2Mo_6I_{14}$

^{19}F-NMR spectrum was recorded on the $Cs_2Mo_6I_8(C_3F_5OO)_6$ nanocluster solution in acetone-d6 to confirm the apical ligand exchange. Figure 6.4 shows NMR spectrum and the two peaks such as δ = -83 (3F) , -120 (2F) were identical to the reported literature.[212, 213] We also performed mass spectrometry analysis on the sample. Mass spectrum was recorded in the negative mode and it was found to be closely matched with the theoretical isotope model for that compound. Fig 6.5 shows mass spectrum of $Cs_2Mo_6I_8(C_3F_5OO)_6$.

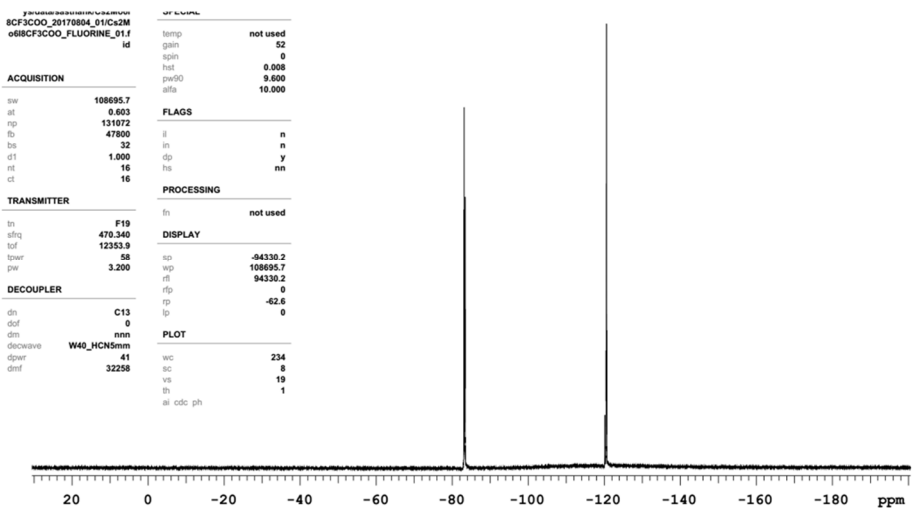

Figure 6.4 ^{19}F-NMR spectrum of $Cs_2Mo_6I_8(C_3F_5OO)_6$ in d6 acetone

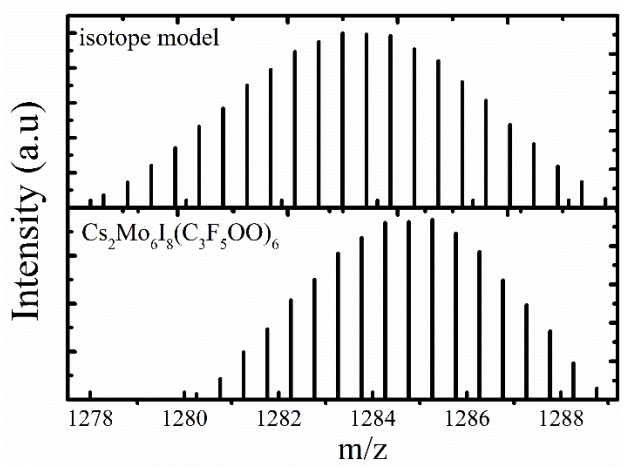

Figure 6.5 Mass spectrum of $Cs_2Mo_6I_8(C_3F_5OO)_6$ solution in the negative mode. Peaks are attributed to the $Mo_6I_8(C_3F_5OO)_6^{2-}$ ions with different isotopic composition.

6.4 Results

6.4.1 Optical Characterization

Figure 6.6 a-6.6 c displays the molecular structure of nanoclusters used in this study and Figure 6.6d shows the absorption and photoluminescence spectra of nanoclusters in dry acetonitrile solution. The inset illustrates the emission from a solution of $Cs_2Mo_6I_8(C_3F_5OO)_6$ positioned over a UV lamp (λ=365 nm).

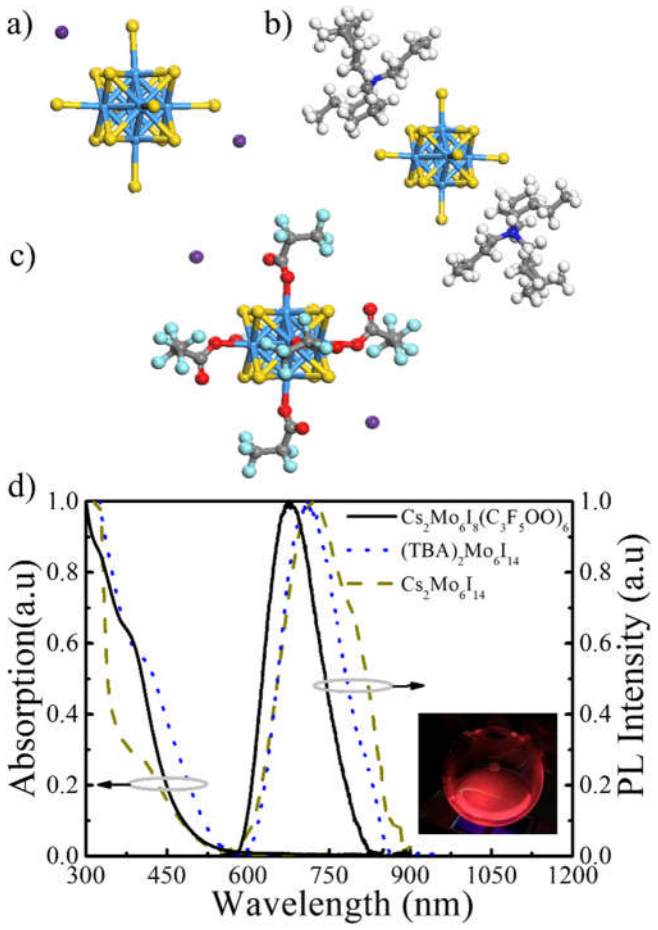

Figure 6.6 Molecular structures and optical characterization of a) $Cs_2Mo_6I_{14}$ b) $(TBA)_2Mo_6I_{14}$ and c) $Cs_2Mo_6I_8(C_3F_5OO)_6$ d) Normalized absorption and photoluminescence spectra of nanoclusters in acetonitrile for $Cs_2Mo_6I_{14}$ (long dash), $(TBA)_2Mo_6I_{14}$ (short dash), and Cs2Mo6I8(C3F5OO)6. The inset shows the photoluminescence of $Cs_2Mo_6I_8(C_3F_5OO)_6$ solution on a UV lamp.

We note that the absorption onset of $Cs_2Mo_6I_8(C_3F_5OO)_6$ is blue-shifted compared with $(TBA)_2Mo_6I_{14}$ and $Cs_2Mo_6I_{14}$. While the starting cluster $Cs_2Mo_6I_{14}$ and $(TBA)_2Mo_6I_{14}$ show similar PL peaks at λ=720 nm, $Cs_2Mo_6I_8(C_3F_5OO)_6$ has a blue shifted PL peak at λ=676 nm highlighting the effect of ligand substitution on the optical properties of the clusters. Based on the luminescence and transient absorption, previous studies revealed that the emission in these types of nanoclusters is attributed to the radiative relaxation of triplet states of-nanoclusters with long natural lifetime of >60 μs.[212] Photoluminescence quantum yields of 68±7% and 17±4 % are

measured for synthesized $Cs_2Mo_6I_8(C_3F_5OO)_6$ and $(TBA)_2Mo_6I_{14}$ respectively in dry, air-free acetonitrile, while the starting cluster $Cs_2Mo_6I_{14}$ showed a PLQY of 6±2%. The PL intensity of these nanoclusters significantly decreases in air due to the energy transfer to molecular oxygen and the formation of singlet oxygen species.[214] Consequently, the PLQY of $Cs_2Mo_6I_8(C_3F_5OO)_6$ and $(TBA)_2Mo_6I_{14}$ are reduced in air to 25 % and 8 % respectively.

6.4.2 Energy Level Measurement

Figure 6.7 shows the UPS spectra of the neat nanocluster films (205 nm) along with the reference ITO substrates.

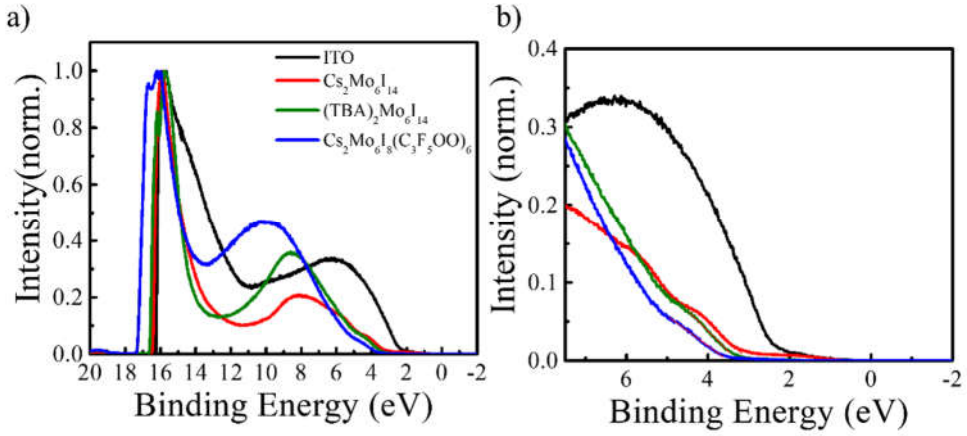

Figure 6.7 a) Full UPS spectra of neat nanocluster films b) Zoomed low binding energy portion of a). Figure a) legend applies to b)

While the starting cluster $Cs_2Mo_6I_{14}$ and $(TBA)_2Mo_6I_{14}$ exhibit HOMO energy levels of 8.2 eV and 7.8 eV respectively, $Cs_2Mo_6I_8(C_3F_5OO)_6$ nanocluster has shallower HOMO energy level (7.2 eV) indicating the strong role of apical ligands on the frontier energy levels of these nanoclusters. By adding phosphorescent bandgap to the HOMO energy level, triplet level for the direct electron injection to nanoclusters can be estimated. $Cs_2Mo_6I_8(C_3F_5OO)_6$ and $(TBA)_2Mo_6I_{14}$ nanocluster showed triplet levels of 5.3 eV and 6.1 eV respectively. Based on the energetics, we

anticipate that the $Cs_2Mo_6I_8(C_3F_5OO)_6$ cluster devices will have an improved electron and hole injection characteristics compared to $(TBA)_2Mo_6I_{14}$ nanoclusters.

6.4.3 Device Characterization

NCLED devices were fabricated based on the architecture shown in the Figure 6.8a with the *J-V-L* characteristics of the devices made with $Cs_2Mo_6I_8(C_3F_5OO)_6$ and $(TBA)_2Mo_6I_{14}$ shown in Figure 6.8 b

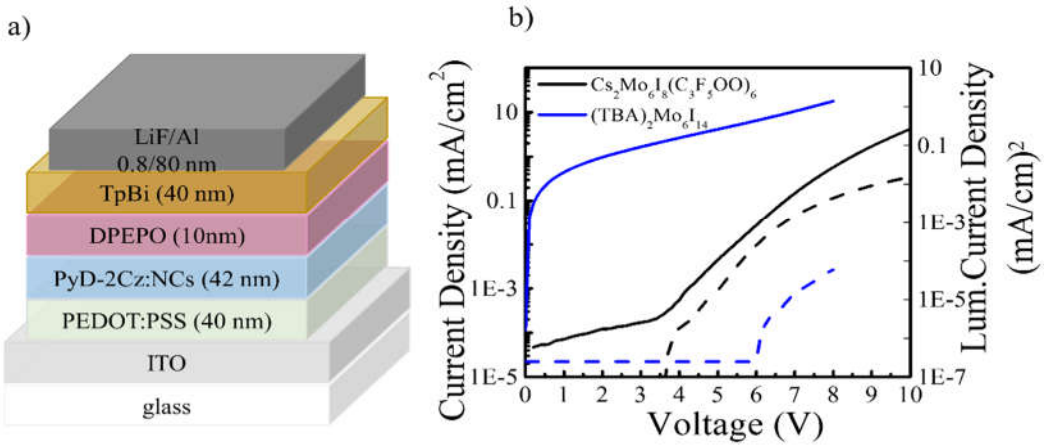

Figure 6.8 a) Schematic of the device architecture. b) J-V-L characterization of the representative NCLED devices made with $(TBA)_2Mo_6I_{14}$ and $Cs_2Mo_6I_8(C_3F_5OO)_6$.

While the devices with $Cs_2Mo_6I_8(C_3F_5OO)_6$ have typical diode characteristics and exhibit an optical turn on voltage of 3.7 V, the devices consisting of $(TBA)_2Mo_6I_{14}$ show large leakage currents with an optical turn-on voltage of 6 V. Figure 6.9 shows the comparison of the photoluminescence and electroluminescence spectra of the nanoclusters, and confirms that the electroluminescence predominantly arises from the nanoclusters along with (in some cases) a small component of host/exciplex emission (λ=500 nm). Various attempts were made to fabricate devices with $Cs_2Mo_6I_{14}$, but the devices showed no nanocluster emission. Figure 6.9b shows the EQE versus current density comparison of the optimized devices. $Cs_2Mo_6I_8(C_3F_5OO)_6$ devices

showed a maximum EQE of 1.1±0.2 % and $(TBA)_2Mo_6I_{14}$ devices showed a maximum EQE of (3.4±0.7) x 10^{-4} %. This is the highest EQE reported for any electrically driven nanocluster LED device.

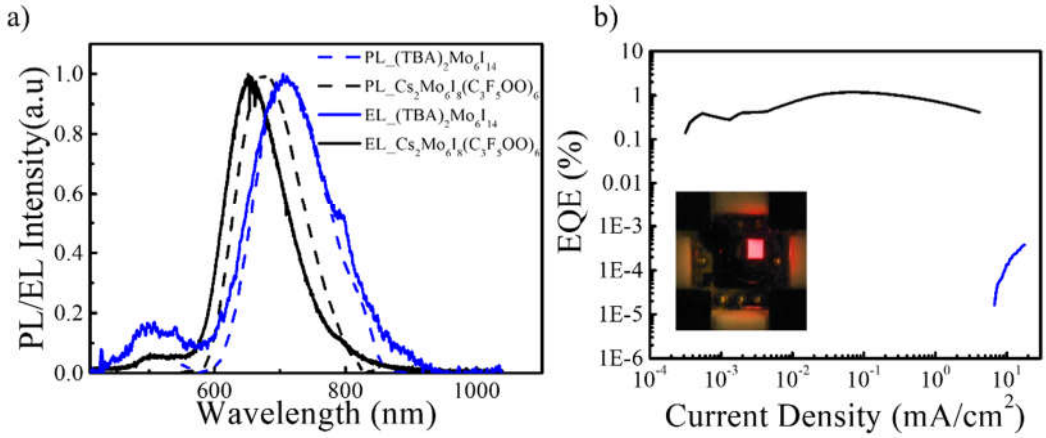

Figure 6.9 Electroluminescence and EQE of Mo-I nanocluster Comparison of electroluminescence (solid lines) and photoluminescence (dashed line) spectra of $(TBA)_2Mo_6I_{14}$ and $Cs_2Mo_6I_8(C_3F_5OO)_6$. b) Comparison of the quantum efficiency (EQE) vs. current density of $(TBA)_2Mo_6I_{14}$ and $Cs_2Mo_6I_8(C_3F_5OO)_6$ devices and the inset shows a photograph of the $Cs_2Mo_6I_8(C_3F_5OO)_6$ nanocluster NCLED.

6.4.4 Device Optimization

Optimization of the $Cs_2Mo_6I_8(C_3F_5OO)_6$ devices was performed by changing the emissive layer thickness and doping concentration in the devices. Figure 6.10 a-b shows a comparison of current density versus voltage and a comparison of the luminescence current density versus voltage of the devices. As the thickness of the emissive layer increased, the turn-on voltage is increased as expected and no EL emission is observed from the 85 nm thickness devices. Figure 6.10c shows the EQE comparison of devices as function of the host thickness leading to an optimum EML thickness of 42 nm.

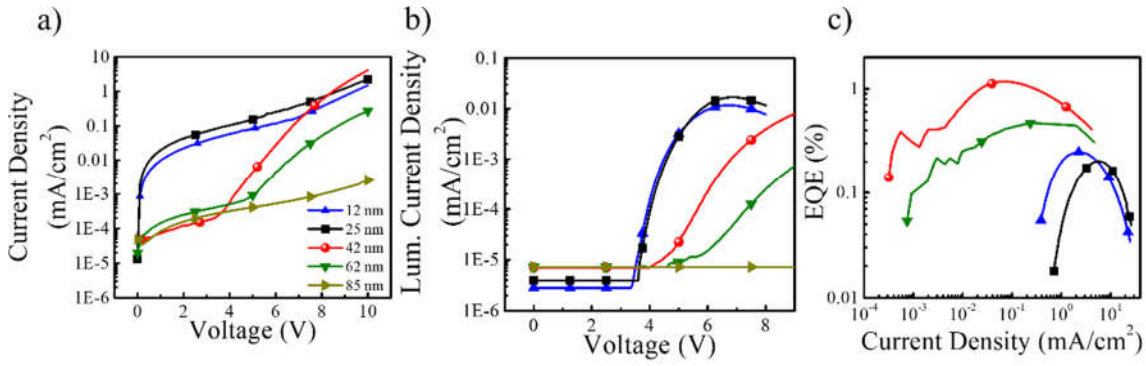

Figure 6.10 Emissive layer thickness dependent optimization. a) Comparison of current density vs. voltage b) luminescence current density vs. voltage and c) external quantum efficiency vs. current density comparison of the devices with $Cs_2Mo_6I_8(C_3F_5OO)_6$

Figure 6.11 shows the EL spectrum of devices fabricated with different doping concentrations in the emissive layer. Devices made with 2 wt.% and 5 wt.% of the nanocluster showed emission predominantly from the host. At concentration > 10 wt.%, the host emission is significantly decreased and the EL is attributed to the nanoclusters.

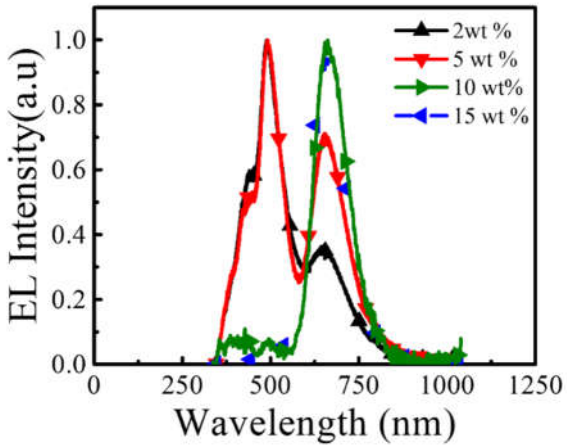

Figure 6.11 Electroluminescence spectra recorded at 6V for $Cs_2Mo_6I_8(C_3F_5OO)_6$ devices made with different doping concentration in the emissive layer.

6.5 Discussion

Previous work has highlighted that the cation substitution strongly affects the electroluminescence efficiency of $[Mo_6Cl_{14}]^{2-}$based clusters.[204] Despite higher PL quantum

yield, devices made with $(TBA)_2Mo_6Cl_{14}$ suffered poor exciton formation due to the cation arrangement in these nanoclusters. We have also seen a similar trend as the Cs cation showed drastically improved performance over the TBA cation substituted nanoclusters devices. Electroluminescence efficiency improvement in $Cs_2Mo_6I_8(C_3F_5OO)_6$ devices is partly due to the improved PLQY in this heavy ligand substituted cluster. Temperature dependent emission studies on $[Mo_6X_8(nC_3F_7COO)_6]^{2-}$ (X = Cl, Br, I) have revealed that the radiative rate constant for triplet state relaxation improved significantly due to the increased spin orbital coupling in the nanocluster with the heavier inner halides combined with a bulkier apical ligand.[215] Our calculations in $[MoCl_{14}]^{2-}$ revealed that the excited state geometry is severely distorted due to the Jahn-teller effect. While similar distortions are observed in $[Mo_6I_{14}]^{2-}$ nanoclusters, the substitution of heavier ligands stabilize the triplet state compared to the halide counterparts resulting in lower non-radiative rates and longer natural lifetimes.[212, 215]

To explore the mechanism of electroluminescence, excitation scans were recorded on 30 nm thick films of 10 wt.% nanocluster doped in PyD-2Cz at the PL emission wavelength (λ= 675 nm and 720 nm) for $Cs_2Mo_6I_8(C_3F_5OO)_6$ and $(TBA)_2Mo_6I_{14}$ nanoclusters respectively. Excitation scans are plotted in Figure 6.12 along with the excitation of PyD-2Cz at its peak PL wavelength (λ= 375 nm).

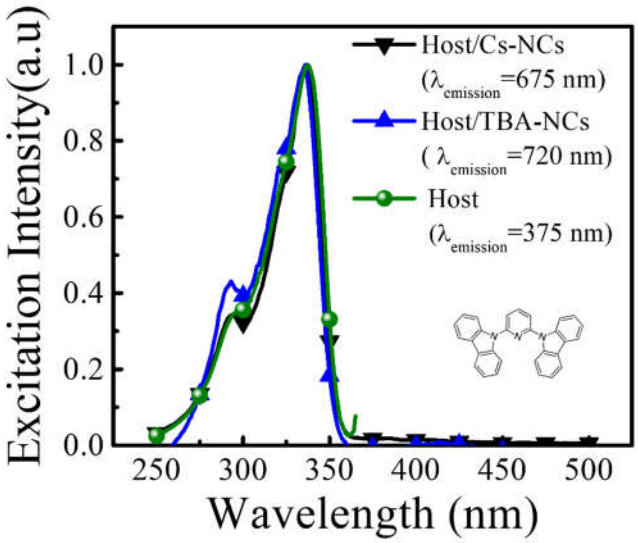

Figure 6.12 Photoluminescence excitations scans of host/nanocluster films recorded at the nanoclusters emission wavelength along with excitation of neat host film recorded at the host emission wavelength

The data clearly show the excitation signature of PyD-2Cz while measuring the emission of the nanoclusters. This suggests that there is energy transfer between the host and the nanoclusters likely stemming from Förster mediated transfer from the host singlet to the nanocluster singlet states but could also stem from Dexter mediated transfer from the host triplet to the nanocluster triplet state. Due to the presence of this energy transfer for both nanoclusters, it then suggests that while energy transfer can be present in these systems, it is not the dominant mechanism for nanocluster excitation given the significant performance variations seen in the EQE. Rather, it appears there are significant differences in the electrical injection efficiency between the two nanoclusters stemming from the different ligands. A similar steric effect was indicated in with $[Mo_6Cl_{14}]^{2-}$ where bulkier anions led to increases in PLQY but much lower quantum efficiency. To clarify the role of the host, we also fabricated devices using $(TBA)_2Mo_6Cl_{14}$ and the best devices still showed an EQE of 0.008% suggesting the variation in the host alone cannot explain the vastly improved quantum efficiency of the $Cs_2Mo_6I_8(C_3F_5OO)_6$ nanocluster. Other factors such

as charge injection and exciton formation appear to be the most critical factors to the enhanced efficiency in $[Mo_6I_{14}]^{2-}$. Large differences in EQE in the devices made with the two iodide based nanoclusters leads to the conclusion that ability to inject charge directly into the nanocluster is the most important mechanism for electroluminescence in these NCLEDs and that this process is impacted collectively by the surrounding cations (smaller is better), terminal ligands (heavier is better), and host selection.

6.6 Conclusion

In summary, we have demonstrated significantly enhanced electroluminescence from phosphorescent hexanuclear metal halide nanocluster salts. Devices made with heavier apical ligands show four-fold improvement in performance compared to halides and nearly three orders of magnitude improvement in previous demonstrations utilizing Mo-Cl based nanoclusters, suggesting a potential pathway for further enhancing NCLEDs. The improvement in these devices is attributed, in part, to the high photoluminescence efficiency of the $Cs_2Mo_6I_8(C_3F_5OO)_6$ clusters due to the presence of strong spin orbital coupling from the combination of heavier inner and apical ligands. In addition, we find that carrier injection efficiency and exciton formation efficiency into the nanocluster is the key limitation and can be overcome through combined pairings of host, cations, and apical ligands with aligned interactions from the host for efficient carrier injection directly into the nanocluster. Collectively, these improvements highlight the promising potential of phosphorescent metal halide nanocluster emitters.

Chapter 7 Conclusion and Future Work

This thesis is focused on developing i) a method to probe the recombination zone and explore phosphorescent emitters alternative to the widely used Pt and Ir complexes in OLEDs; and ii) a new platform for phosphorescent emitters based on nanoclusters. While this thesis highlighted a new paradigm for OLED emitters, there are number of opportunities to improve the efficiency of nanocluster light emitting diodes. Here we summarize the findings of this thesis research and describe various strategies that can be utilized to further improve the performance of NCLEDs.

7.1 Conclusion

The first part of this thesis is aimed at understanding the exciton generation profiles by developing a more quantitative method for such characterization. The generated exciton density is typically highest in the recombination zone and it is necessary to lower the exciton density so that annihilation of excitons can be prevented at higher current density to improve the EQE roll off and increase performance at higher brightness. One way to reduce the exciton density is by increasing the width of recombination zone in the devices. To achieve this, we first looked to understand where the recombination occurs and the factors that control the recombination in OLEDs. In Chapter 4 we described a method to probe recombination zone in various OLED architectures using a sensing layer embedded at various location of the devices. Our results showed that S-EML devices made with a host material that has a higher propensity for hole transport had the RZ pinned at the interface of the emissive and electron transport layers. However, S-EML devices made with ambipolar host materials had a recombination profile distributed throughout the emissive layer. Comparing the performance of the device, devices that had wider RZ resulted better performance such as low EQE roll off than the devices with RZ pinned at the interface. Unexpectedly, our M-

EML device showed very narrow RZ. Nevertheless, this work highlighted the impact of relative energy levels (Δ_{HOMO} and Δ_{LUMO}) on carrier injection and showed how recombination can be modified by adopting various emissive layer architecture in OLEDs.

In the second part of this thesis, we developed the first metal halide phosphorescent light emitting diodes that can replace organic emitters and extend emission in the near-infrared. Phosphorescent emitters that harvest both the singlet and triplet excitons for light emission have propelled OLEDs into the mass market. However, the current phosphorescent emitter catalog consist mainly of costly organometallic complexes of Pt and Ir. In chapter 5, we expanded the phosphorescent materials catalog for LEDs based on molybdenum halide nanoclusters and nanocluster salts that are inexpensive and abundant. We showed high photoluminescence quantum yield and demonstrated electrically and optically pumped luminescent devices. We found that cation substitution strongly influence the electroluminescent efficiency and spectral properties in these nanoclusters. While the optically pumped devices fabricated from $(TBA)^+$ nanoclusters show NIR emission with a peak EQE of 2.3%, the performance of electrically pumped devices are found to be much lower and do not reflect the high PLQY of these nanoclusters. EL transient studies indicate that the host-guest interactions and poor exciton formation is the key limitation due to cation arrangement in the nanoclusters that impacts tunneling and recombination dynamics. Theoretical calculations showed that Pseudo Jahn Teller (PJT) distortion is operative in the phosphorescent emitting state of these nanoclusters. These distortions are responsible for the broader PL spectrum of this nanocluster. We also believe these distortions might play a role in the radiative/non radiative rates in these nanoclusters.

In Chapter 6, we demonstrated electroluminescence from hexanuclear molybdenum iodide based nanocluster salts. Devices made with heavier apical ligands such as pentrafluropropionate

showed four-fold improvement in performance compared to lighter ligands, suggesting a potential pathway for further improving the performance of NCLEDs. The performance improvement in these devices is attributed, in part, to the improved photoluminescence of these Mo-I clusters due to the presence of strong spin orbital coupling present in the nanoclusters with heavier inner ligands combined with a bulkier apical ligands. In addition, we overcame the key limitation of previous work such as poor charge injection and exciton formation through combined pairing of host, cation, and apical ligands. We have unlocked an entirely new materials platform for light emitting diodes and accordingly, there is much still to learn and optimize with these systems.

7.2 Future Work

In this section, we highlight additional strategies that can be used to further improve the efficiency of NCLEDs.

7.2.1 Approaches to Improve NCLEDs Performance

7.2.1.1 Host Materials

Selecting and developing host materials with suitable energy levels for nanocluster emission is challenging as the HOMO energy level in these nanocluster is often very deep (~6.5 – 7 eV). It is important to choose host materials with suitable triplet energy level so that the back energy transfer from emitter to host can be prevented. In addition, organic hosts utilized in this work typically shows low carrier mobilities and a large difference between hole- and electron-mobilities. This dissimilarity in mobilities leads to recombination preferably at the interface of emissive and transport layers that leads to poor device performance such as high roll off and lower lifetime [216]. To promote broader recombination, host materials with good mobilities for both charge carriers needs to be developed. Recently, there has been growing interest to use bipolar host materials that consist both donor and acceptor groups separated by steric groups with good

hole and electron mobilities. These host materials have been successfully used to incorporate blue, green and red emitting and resulted huge improvement in the efficiency of OLEDs and could be applicable in NCLEDs.[145] Looking ahead, the development of suitable inorganic hosts could provide a way to eliminate the organic layers altogether and enable higher brightness operation.

7.2.1.2 Enhancing Luminescence by Antenna Effects

Carboxyl ligands with strong absorption bands in the near UV spectrum are shown to transfer the absorbed energy to core metal atom via ligand to metal charge transfer (LMCT) which enhanced the quantum efficiency of the core cluster.[217] It would be compelling to explore if similar types of energy transfer from ligand to core cluster are possible through electrical excitation. This will also help to avoid using host materials for energy transfer, which will simplify the device fabrication process as this guest/host architecture require some optimization in finding the suitable dopant concentration for optimum performance.

7.2.1.3 Exploring Other Nanocluster Compositions

Along with molybdenum, tungsten, and rhenium based nanoclusters have also shown attractive photophysical properties. For example, the $[W_6X_{14}]^{2-}$ series exhibit peak emission at 690 nm with similar quantum yield in solution (~ 50 %).[218] Interestingly, the life time of these cluster is (50 µs) compared with (120 µs) of the $[Mo_6X_{14}]^{2-}$ series and hence, a lower triplet-triplet (TTA) annihilation is anticipated in these class of materials during electrical excitation as TTA scales with life time of emitter.[159] Hexanuclear rhenium based cluster in the form: $A_4[Re_6Q_8L_6]$, where A = Cs or K , Q=S or Se and L = OH or CN or halides or organic ligands also shown to have attractive photoluminescence properties.[219] Future studies can be directed to the synthesis of tungsten based nanoclusters with similar apical ligands developed in this thesis that could similarly result in high quantum yields.

7.2.1.4 Cations and Apical Ligands Optimization

We have identified that the cations in these nanocluster play a significant role in the electroluminescence process. Our results indicate that the Cs^+ cation showed better performance than to the TBA^+ cation due to the reduced hindrance for charge injection. Hence, future work should explore different cations that can be substituted to the nanoclusters. Single charge cations such as Ca^+, Ti^+ and Cu^+ or doubly charged cations such as Cu^{2+} or Co^{2+} can be substituted to the core cluster.

In addition, we also highlighted the strong role of apical ligands on the performance of the NCLEDs. It would be interesting to see how the heavy ligands vary with different sizes for example $(CF_3COO)^-$ and $(C_3F_7COO)^-$ can affect the device performance. Additional ligand exchange and cation exchange reactions with the core cluster might help further optimization of device performance.

7.3 Transparent Luminescent Solar Concentrators (TLSCs)

Significant potential exist for capturing the UV portion (~10% on an energy scale) of the solar spectrum for energy production. Previous work in our lab has focused on using $[Mo_6X_{14}]^{2-}$ based nanoclusters that exhibit large Stokes shift combined with high PL quantum efficiency for solar concentrator applications.[178] The $[Mo_6I_{14}]^{2-}$ based nanocluster developed in this thesis also show a similar Stokes shift with better PLQY than the Cl-based clusters. By employing I-based clusters in TLSCs we can further enhance the efficiency of the transparent solar concentrators. These devices can be made in large areas at affordable cost while preserving the aesthetic appeal when mounting them over large buildings and mobile electronics. Looking ahead, because the triplet emission is roughly half the energy of the singlet bandgap there is also a great opportunity

to explore the possibility of observing/exploiting singlet fission to double the efficiency of the TLSC.

7.4 Epitaxial Growth

Epitaxy is the lattice matched growth of single-crystal materials. Epitaxial growth is widely used in nanotechnology and semiconductor fabrication as it offer ways to make affordable, high quality crystals. LEDs comprise of inorganic compound semiconductors such as AlGaAs (red), AlInGaP (yellow-green, InGaN (blue) have benefited tremendously from the development of the epitaxial growth methods namely molecular beam epitaxy (MBE), metal-organic vapor phase epitaxy (MOVPE). Similarly, epitaxy can be used to grow organic single crystals that can be integrated into organic electronics devices. Epitaxy method hold promise to fabricate high performance organic-opto electronic devices as the devices made with organic single crystals showed markedly improved performance compared to amorphous, disordered organic semiconductors.[220, 221]. Depending on the substrate choice, epitaxy can be broadly classified as homo-epitaxy and hetero-epitaxy. In homoepitaxy, the substrate and the growth materials are the same crystalline material (example Si on Si) and in heteroepitaxy substrate and growth materials are different (example Si on sapphire). In our lab, we were interested in identifying epitaxial growth mechanisms of metal halides such as NaCl using in situ reflection high-energy electron diffraction (RHEED). After demonstrating such homoepitaxy of NaCl, we wanted to test if LEDs could be developed with such epitaxial growth (assuming we could eventually electrically dope NaCl). To investigate this possibility we grew OLEDs utilizing vapor-deposited NaCl as a host, co-evaporated with dilute $Ir(ppy)_3$ as the emitter in an OLED device. The complete architecture of the devices is as follows: ITO/MoO_3(150Å)/ NaCl:$Ir(ppy)_3$(6vol.%, 200Å)/LiQ (8Å)/Al (800Å) where $Ir(ppy)_3$ is fac-tris(2-phenylpyridine)iridium and LiQ is 8-

hydroxyquinoline lithium. Two control devices were fabricated simultaneously using the same architecture but just with the host (NaCl) and with a widely used host materials 4,4′ -Bis(N-carbazolyl)-1,1′ -biphenyl (CBP).

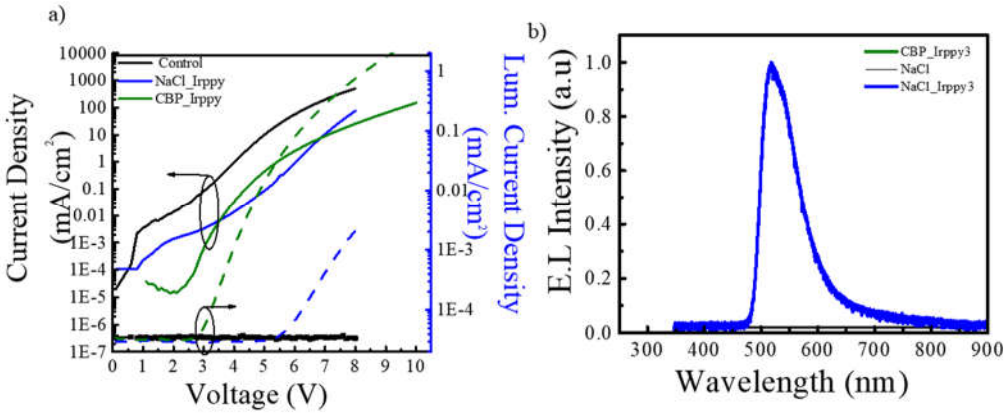

Figure 7.1 NaCl Host OLEDs. *J-V-L* characteristics of the devices made with NaCl and NaCl_Ir(ppy)$_3$ and CBP_Ir(ppy)$_3$ as emissive layers and b) EL spectra of the devices

Figure 7.1a shows a comparison of current density (*J*) and luminescence current density (*L*) vs voltage (*V*) characteristics of the control devices and the device with Ir(ppy)$_3$ doped NaCl. Figure 7.1b shows the electroluminescence (EL) spectrum of the doped NaCl device, which is consistent with the EL for the conventional devices made with CBP host architecture. The absence of luminescence current in the control devices made with just NaCl and the similarity of EL spectrum between the NaCl: Ir(ppy)$_3$ and CBP:Ir(ppy)$_3$ demonstrates that the emission in the doped NaCl devices originates only from the dopant. The un-optimized NaCl host devices showed lower EQE (0.005 %), which may be due to higher electron and hole injection barriers to NaCl. Further optimization such as varying thickness, doping % of emitter and adding blocking layers to prevent the exciton leakage in the devices is necessary. Nevertheless, this work highlights the application of metal halides such as NaCl as a potential host for making OLEDs that could eventually translate into “epitaxial” OLEDs.[222]

7.5 Si Nanocrystal based LEDs

Semiconductor nanocrystals are also promising candidates for LEDs as they are non-toxic and abundant, and can complement nanoclusters by extending deeper into the NIR than the nanoclusters (900nm-1000nm). They also offer unique properties such as size dependent emission with high PLQYs up to 50%.[170] Although bulk silicon shows poor photoluminescence properties because of the indirect bandgap, silicon nanocrystal (Si NCs) with a size less than 5 nm show intense room temperature PL from the quantum confinement effect. Utilizing surface passivation, the PLQY of Si NCs has improved tremendously.

We have performed preliminary work using these Si NCs synthesized by non-thermal plasma techniques and functionalized Si NCs with a ligand 1-dodecene.[223] In a typical surface passivation reaction, Si nanocrystals were dissolved in 1:5 vol. mixture of 1-dodecene and mesitylene using ultra sonication for 30 mins. This solution was then transferred to a Schlenk flask using cannula transfer and refluxed about three hours under nitrogen atmosphere resulting a clear orange solution as shown in the Figure 7.2b indicating the end of functionalization. It is important to minimize the oxygen exposure to the as synthesized Si NCs and also during the passivation reaction as the oxidized samples present difficulties undergoing surface passivation.

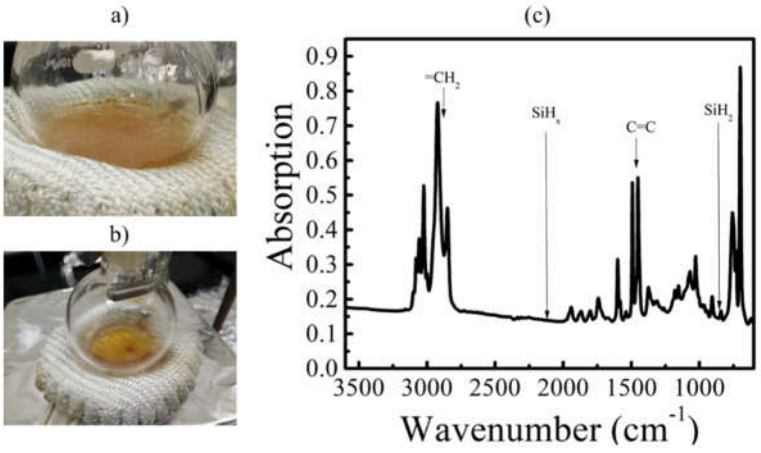

Figure 7.2 a) Functionalization of Si NCs. Si NCs dissolved in 1-dodecene and mesitylene before functionalization b) Clear Si NCs solution after functionalization c) FTIR absorption of functionalized Si NCs thin films showing the absence of SiH_2 and SiH_x peaks and the presence of ligands on the nanocrystals surface suggesting the completion of hydrosilation reaction.

After three hours, the solvent is completely evaporated under vacuum and functionalized particles are dissolved in chloroform or hexane. Fourier transform infrared (FTIR) absorption measurements in Fig 7.2 c shows the absence of SiH_x and SiH_2 peaks and the presence of $=CH_2$ and C=C peaks of the 1 dodecene indicating the successful surface coverage of Si NCs by the organic ligands.[224]

We have devices with the functionalized Si nanocrystals using the architecture ITO/ ZnO (30nm) / Si NCs (38 or 60 nm) / TAPC (20nm) / MoO_3 (10 nm) / Al (80 nm) to show the electroluminescence of Si NCs. Control devices were fabricated without the Si NCs for comparison. Figure 7.3a shows the *J-V* characteristics of the control as well as the SiNCs layer devices. While the control devices showed a large leakage, the SiNCs devices showed diode like behavior. Figure 7.3b shows the luminescent current density versus voltage characteristics of the devices. The optical turn on voltage of the devices was found to be 2.0 V and 3.1 V for the 38 nm and 60 nm EML devices. No luminescence was observed from the control device suggesting the electroluminescence stems from the SiNCs.

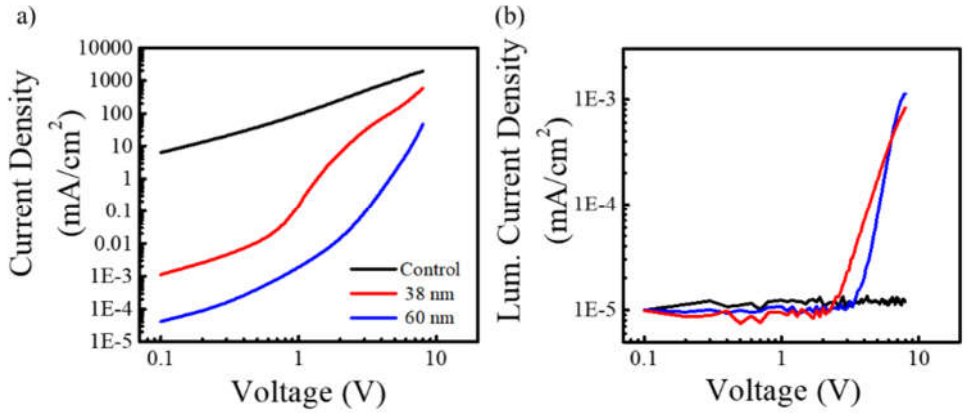

Figure 7.3 SiNCLED Devices. *J-V* and *L-V* characteristics of the Si NC devices made with 38 and 60 nm EML

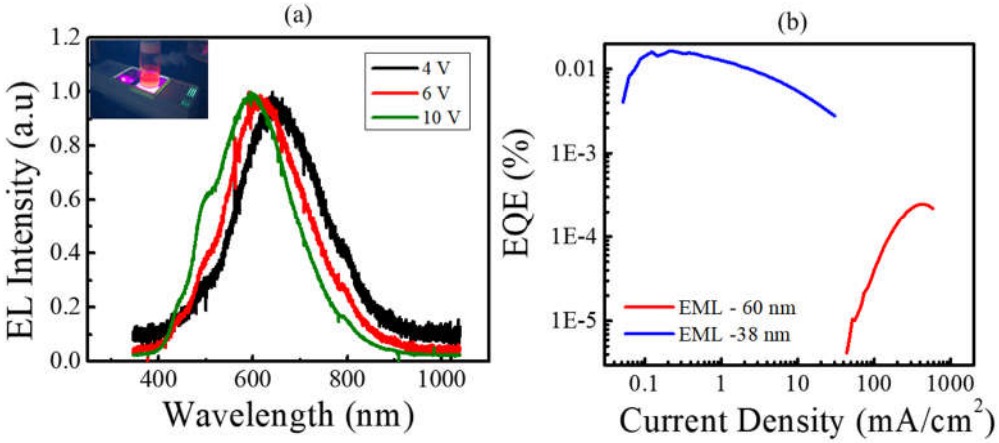

Figure 7.4 SiNCLED Performance. EL spectra of SiNCs devices recorded at different applied bias and inset shows the PL of Si NCs solution on a UV bench top lamp. b) EQE comparison of the devices made with 38 nm and 60 nm EML

EL spectra was recorded for SiNCs device made with 60 nm EML at different applied bias and the inset show the photoluminescence of Si NCs solution on a UV lamp. A maximum EQE was of 0.02 % was measured. While this is substantially lower than the highest reported EQE of 10 % for SiNCs, similar PLQY obtained in our lab encourages to continuously explore suitable LED architecture.

Further improvement in the Si NCs LEDs can be made by identifying the best transport layers to be used in the conventional architecture. In addition, optimization of spin coating process for Si NC layer is also needed to obtain films with good morphology. Poor morphology could stem from the free ligands surrounding the Si NCs in addition to the surface anchored ligands and hence more optimization is needed to completely remove the free ligands from the Si NCs after passivation.

APPENDICES

APPENDICES

APPENDIX A – Electroluminescence spectra of sensing layer devices

Electroluminescence spectra obtained from a sensing layer inserted at various positions of optimized S-EML(E-Host), S-EML(H-Host), D-EML devices with E-Host/H-Host or H-Host/E-Host and M-EML devices consisting of a 3:1 vol. mixture of E-Host:H-Host (Figure A1 to A5).

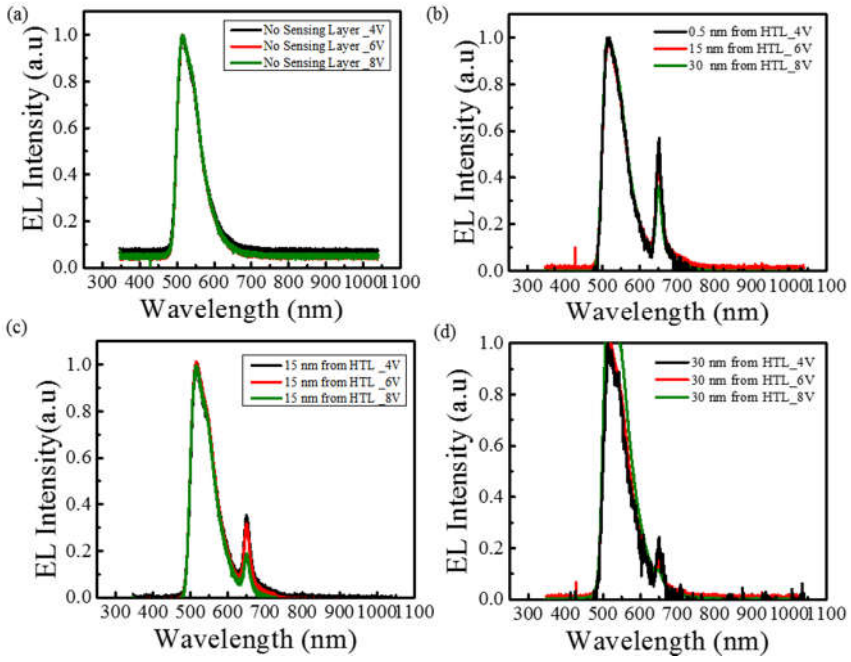

Figure A1 Comparison of EL spectra obtained at different bias from sensing layer inserted at various distance in the emissive layer of S-EML (E-Host) devices a) Control devices that does not have sensing layer, b) sensing layer inserted at 0.5 nm c) 15 nm and d) 30 nm from hole transport layer (HTL).

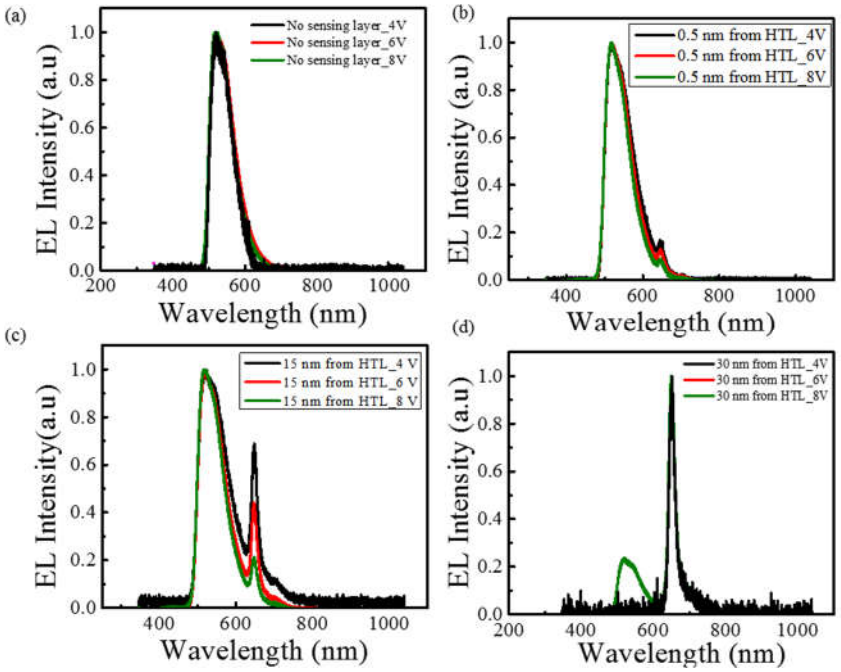

Figure A2 Comparison of EL spectra obtained at different bias from sensing layer inserted at various distance in the emissive layer of S-EML (H-Host) devices a) Control devices that does not have sensing layer, b) sensing layer inserted at 0.5 nm c) 15 nm and d) 30 nm from hole transport layer (HTL).

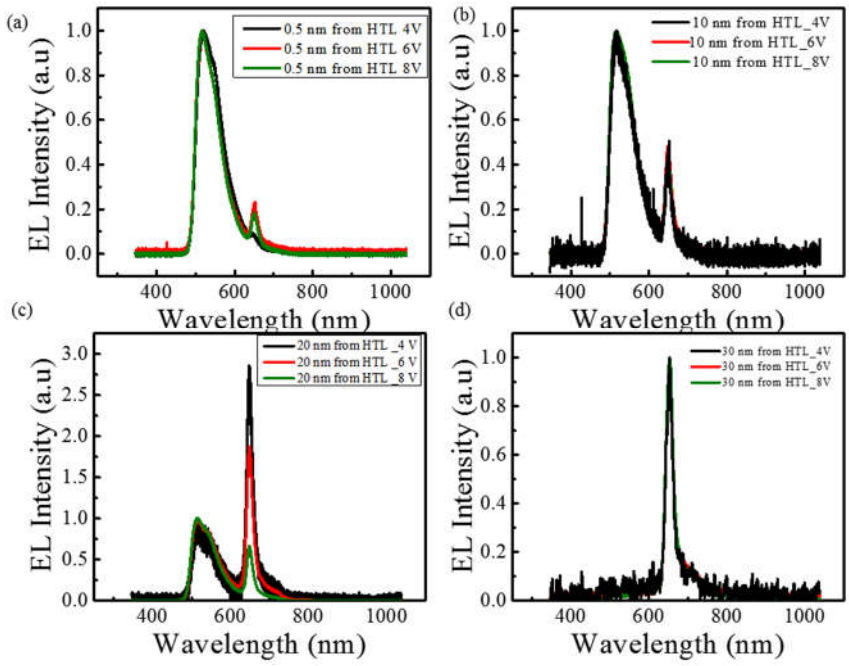

Figure A3 Comparison of EL spectra obtained at different bias from sensing layer inserted at various distance in the emissive layer of D-EML (E-Host/H-Host) devices. a) Sensing layer inserted at 0.5 nm b) 10 nm, c) 20 nm, and d) 30 nm from the hole transport layer.

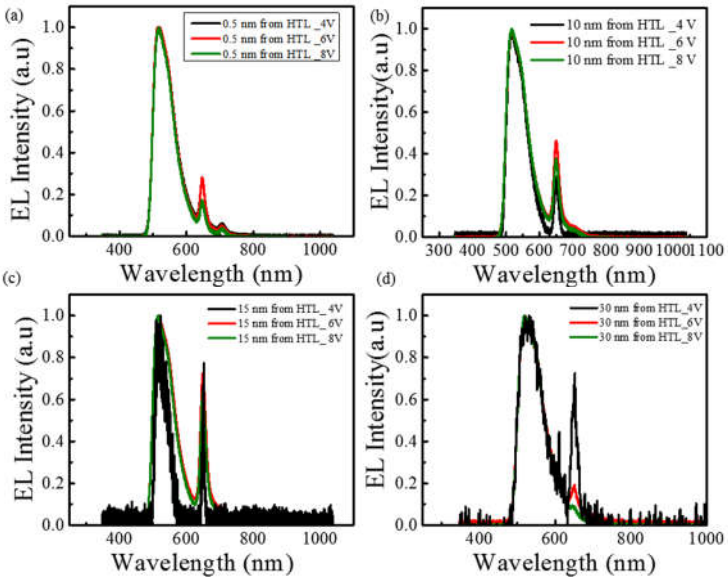

Figure A4 Comparison of EL spectra obtained at different bias from sensing layer inserted at various distance in the emissive layer of D-EML (H-Host/E-Host) devices. a) Sensing layer inserted at 0.5 nm b) 10 nm, c) 20 nm, and d) 30 nm from the hole transport layer

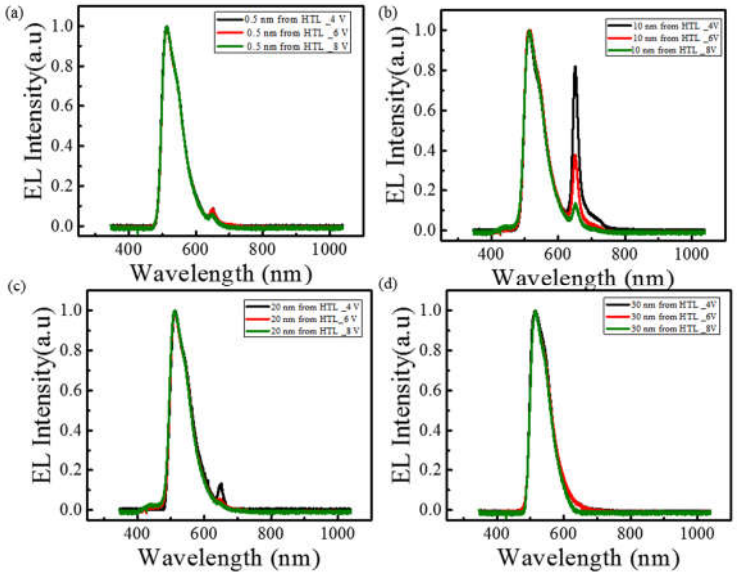

Figure A5 Comparison of EL spectra obtained at different bias from sensing layer inserted at various distance in the emissive layer of M-EML (H Host :E Host) devices. a) Sensing layer inserted at 0.5 nm b) 10 nm, c) 20 nm, and d) 30 nm from the hole transport layer

APPENDIX B – Energy level calculation of the Molecules used in chapter 4

Correlation of HOMO energy values (Table B1) obtained from B3LYP calculation vs. experimental HOMO values obtained from UPS spectroscopy and cyclic voltammetry along with the molecules used for the performing correlation (Figure B1). Correlation of HOMO energy values obtained from B3LYP vs. correlated HOMO values of the molecules used in this study. (Figure B2)

Computational Methodology

The ground-state (S_0) configurations of a set of organic and organometallic compounds were computed using Density Functional Theory (DFT) with hybrid functional (B3LYP)[194] and 6-31g* basis set.[225] For Ir atom, modified LANL2DZ basis set is chosen for the core electrons and effective core potential (lanl2dz) is used describe the valence electron. The energies of the highest occupied molecular orbital (HOMO) and the lowest unoccupied molecular orbital (LUMO) were obtained from the S_0 geometry. The vibrational analysis on these geometries were performed and the lack of imaginary frequencies helped to ascertain the minima in the potential energy surface (PES). All calculations were performed using G09 suite of programs.[226]

Using the above methodology, the HOMO energies of a set of molecules are computed; the molecular structures of these molecules are shown in Figure B1 A). The computed HOMO energies are compared with oxidation potentials (measured using cyclic voltammetry) and ionization potentials (measured using ultraviolet photoelectron spectroscopy (UPS)) in Figure B1 (B).[227] The computed HOMO energies correlate with both oxidation potentials and ionization potentials. Furthermore, the slope of the linear fit between computed HOMO and measured UPS energies is close to 1.0. Similar correlation also exist between computed LUMO energy and energies estimated using IPES measurements.[228] Therefore, the computed frontier orbital

energies are used to predict the relative difference between HOMO and LUMO energies if the molecules.

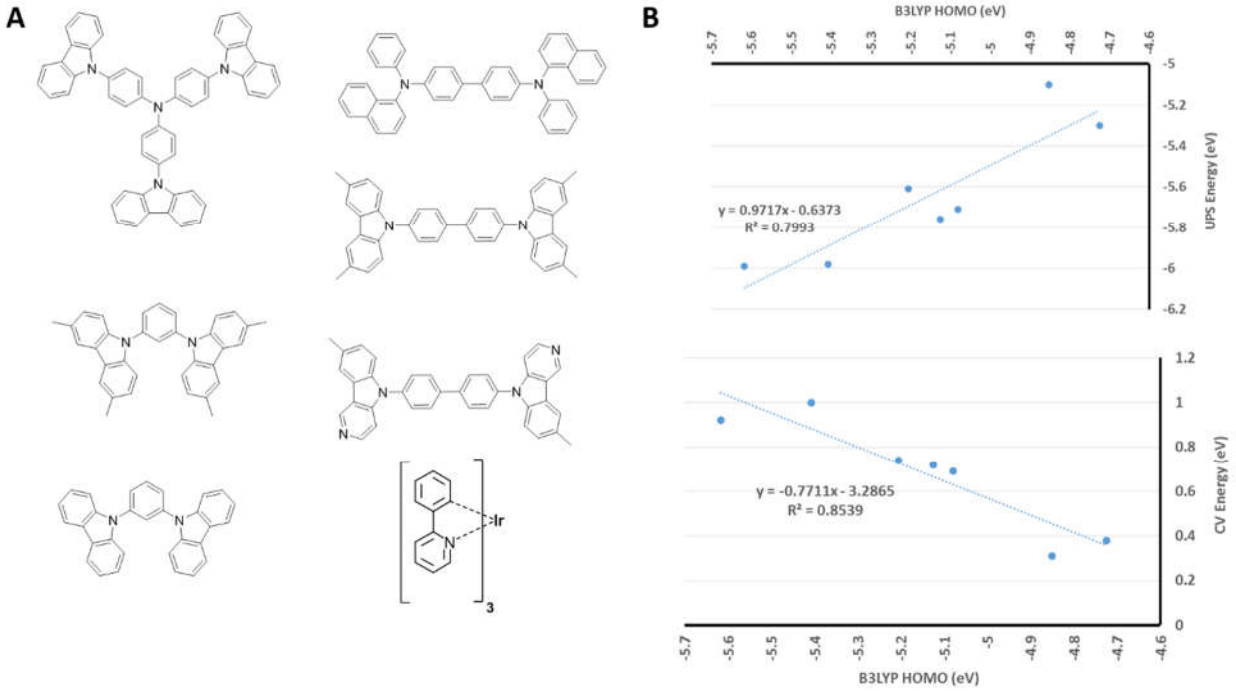

Figure B1 a) Molecular structures of compounds used to develop the correlation between computed HOMO energies and experimental measurements; b) Correlation between computed HOMO energy level obtained from DFT calculations (B3LYP/6-31g* method) and experimental HOMO energy, measured using UPS and CV.

Table B1 lists the computed frontier orbital energies of NPD (HTL), CPCBPTz (E-Host), BCzPh (H-Host) and BTB (ETL). Δ_{HOMO} is used to predict the injection barrier for holes between HTL and the adjacent layers; larger barrier indicates poorer injection. Similarly, Δ_{LUMO} is used to predict the injection barrier for electrons between ETL and the adjacent layer; larger barrier indicates poorer injection of electrons from ETL. Table B1: Energies of frontier orbitals of HTL, E-host, H-host, ETL and $Ir(mppy)_3$; Δ_{HOMO} and Δ_{LUMO} are computed w.r.t HTL and ETL respectively.

Materials	E_{HOMO} (eV)	E_{LUMO} (eV)	Δ_{HOMO} (eV)	Δ_{LUMO} (eV)
HTL	-4.72	-1.13	-	1.01
E-Host	-5.26	-1.99	-0.54	0.15
H-Host	-4.97	-0.67	-0.25	1.47
ETL	-6.18	-2.14	-1.46	-

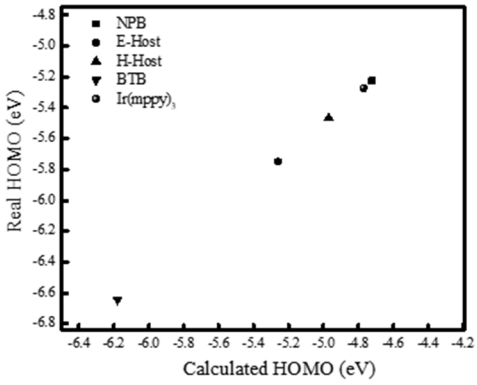

Figure B2 Correlation of the HOMO energy level obtained from DFT calculation with B3LYP functional vs. real HOMO energy values for the molecules

List of Publications

1. Padmanaban S. Kuttipillai, Pei Chen, Chenchen Yang, M. Bates, Richard R. Lunt, “Enhanced Electroluminescence Efficiency in Nanocluster Light Emitting Diodes through Apical Ligand Exchange” (in review)

2. Padmanaban S. Kuttipillai, Sukrit Mukhopadhyay, Anatoliy Sokolov, Kenneth L. Kearns, W. H. Hunter Woodward, Richard R. Lunt, “Mapping Recombination Profiles in Single-, Dual-, and Mixed-Host Phosphorescent Organic Light Emitting Diodes” Organic Electronics 57 (2018) 28–33

3. Dianyi Liu, Qiong Wang , Christopher J. Traverse , Chenchen Yang , Margaret Young , Padmanaban S. Kuttipillai , Sophia Y. Lunt , Thomas W. Hamann , Richard R. Lunt “ Impact of Ultrathin C 60 on Perovskite Photovoltaic Devices” ACS Nano, 2018, 12 (1), pp 876–883

4. Lili Wang, Pei Chen, Non Thongprong, Margaret Young, Padmanaban S. Kuttipillai, Kai Sun, Phillip M. Duxbury, Richard R. Lunt “Unlocking the Epitaxy of Inorganic Halide Perovskites” Adv. Mater. Interfaces 2017, 4, 1701003.

5. Pei Chen, Padmanaban S. Kuttipillai, Lili Wang, and Richard R. Lunt, “Homoepitaxial Growth of Metal Halide Crystal Investigated by Reflection High-Energy Electron Diffraction” Scientific Reports 7, 40542, (2017).

6. Padmanaban S. Kuttipillai, Yimu Zhao, Christopher J. Traverse, Benjamin G. Levine, Richard R. Lunt, “Phosphorescent Nanocluster Light Emitting Diodes” Advanced Materials 2016,28 (2), 316-319

List of Patents

7. Richard R Lunt, Padmanaban Sasthan Kuttipillai, “Nanocluster Based Light Emitting Diodes” Issued US Patent, US20150069366 A1, Michigan State University

BIBILIOGRAPHY

BIBLIOGRAPHY

1. Forrest, S.R., *The road to high efficiency organic light emitting devices.* Organic Electronics, 2003. **4**(2): p. 45-48.

2. Sasabe, H. and J. Kido, *Development of high performance OLEDs for general lighting.* Journal of Materials Chemistry C, 2013. **1**(9): p. 1699-1707.

3. Forrest, S.R. and M.E. Thompson, *Introduction: organic electronics and optoelectronics.* Chemical Reviews, 2007. **107**(4): p. 923-925.

4. Brütting, W., *Introduction to the physics of organic semiconductors*. 2006: Wiley Online Library.

5. Vincett, P., et al., *Electrical conduction and low voltage blue electroluminescence in vacuum-deposited organic films.* Thin solid films, 1982. **94**(2): p. 171-183.

6. Tang, C.W. and S. VanSlyke, *Organic electroluminescent diodes.* Applied Physics Letters, 1987. **51**(12): p. 913-915.

7. Baigent, D.R., et al., *Polymer electroluminescence in the near infra-red.* Synthetic Metals, 1995. **71**(1–3): p. 2175-2176.

8. Yersin, H., *Triplet emitters for OLED applications. Mechanisms of exciton trapping and control of emission properties.* Transition Metal and Rare Earth Compounds, 2004: p. 1-26.

9. Adachi, C., et al., *Nearly 100% internal phosphorescence efficiency in an organic light-emitting device.* Journal of Applied Physics, 2001. **90**(10): p. 5048-5051.

10. Baldo, M., et al., *Highly efficient phosphorescent emission from organic electroluminescent devices.* Nature, 1998. **395**(6698): p. 151-154.

11. Baldo, M., et al., *Very high-efficiency green organic light-emitting devices based on electrophosphorescence.* Applied Physics Letters, 1999. **75**(1): p. 4-6.

12. Pode, J.-H.K.a.R., *High Efficiency Red Phosphorescent Organic Light-Emitting Diodes with Simple Structure, Organic Light Emitting Diode - Material, Process and Devices* 2011.

13. Kalyani, N.T. and S. Dhoble, *Organic light emitting diodes: Energy saving lighting technology—A review.* Renewable and Sustainable Energy Reviews, 2012. **16**(5): p. 2696-2723.

14. Park, Y., et al., *Work function of indium tin oxide transparent conductor measured by photoelectron spectroscopy.* Applied Physics Letters, 1996. **68**(19): p. 2699-2701.

15. Tokito, S., K. Noda, and Y. Taga, *Metal oxides as a hole-injecting layer for an organic electroluminescent device.* Journal of Physics D: Applied Physics, 1996. **29**(11): p. 2750.

16. Kim, W., et al., *Molecular organic light-emitting diodes using highly conducting polymers as anodes.* Applied Physics Letters, 2002. **80**(20): p. 3844-3846.

17. Lin, H.-W., et al., *Solution-processed hexaazatriphenylene hexacarbonitrile as a universal hole-injection layer for organic light-emitting diodes.* Organic Electronics, 2013. **14**(4): p. 1204-1210.

18. Shi, S., et al., *Solution-processable graphene oxide as an efficient hole injection layer for high luminance organic light-emitting diodes.* Journal of Materials Chemistry C, 2013. **1**(9): p. 1708-1712.

19. Han, T.-H., W. Song, and T.-W. Lee, *Elucidating the crucial role of hole injection layer in degradation of organic light-emitting diodes.* ACS applied materials & interfaces, 2015. **7**(5): p. 3117-3125.

20. Cao, Y., et al., *Ultrathin layer alkaline earth metals as stable electron-injecting electrodes for polymer light emitting diodes.* Journal of Applied Physics, 2000. **88**(6): p. 3618-3623.

21. Hung, L., C.W. Tang, and M.G. Mason, *Enhanced electron injection in organic electroluminescence devices using an Al/LiF electrode.* Applied Physics Letters, 1997. **70**(2): p. 152-154.

22. Zheng, X., et al., *Efficiency improvement of organic light-emitting diodes using 8-hydroxy-quinolinato lithium as an electron injection layer.* Thin Solid Films, 2005. **478**(1): p. 252-255.

23. Liu, Z., O. Salata, and N. Male, *Improved electron injection in organic LED with lithium quinolate/aluminium cathode.* Synthetic metals, 2002. **128**(2): p. 211-214.

24. Adachi, C., K. Nagai, and N. Tamoto, *Molecular design of hole transport materials for obtaining high durability in organic electroluminescent diodes.* Applied Physics Letters, 1995. **66**(20): p. 2679-2681.

25. Huang, F., et al., *Crosslinkable hole-transporting materials for solution processed polymer light-emitting diodes.* Journal of Materials Chemistry, 2008. **18**(38): p. 4495-4509.

26. Kulkarni, A.P., et al., *Electron transport materials for organic light-emitting diodes.* Chemistry of materials, 2004. **16**(23): p. 4556-4573.

27. Meerheim, R., et al., *Ultrastable and efficient red organic light emitting diodes with doped transport layers.* Applied Physics Letters, 2006. **89**(6): p. 061111.

28. Walzer, K., et al., *Highly efficient organic devices based on electrically doped transport layers.* Chemical reviews, 2007. **107**(4): p. 1233-1271.

29. Tao, Y., C. Yang, and J. Qin, *Organic host materials for phosphorescent organic light-emitting diodes.* Chemical Society Reviews, 2011. **40**(5): p. 2943-2970.

30. Ku, S.-Y., et al., *High-luminescence non-doped green OLEDs based on a 9, 9-diarylfluorene-terminated 2, 1, 3-benzothiadiazole derivative.* Journal of Materials Chemistry, 2009. **19**(6): p. 773-780.

31. Wang, Q., et al., *A Non-Doped Phosphorescent Organic Light-Emitting Device with Above 31% External Quantum Efficiency.* Advanced Materials, 2014. **26**(48): p. 8107-8113.

32. Peng, T., et al., *A phosphorescent material with high and balanced carrier mobility for efficient OLEDs.* Chemical Communications, 2011. **47**(11): p. 3150-3152.

33. Segal, M., et al., *Excitonic singlet-triplet ratios in molecular and polymeric organic materials.* Physical Review B, 2003. **68**(7): p. 075211.

34. Nakanotani, H., et al., *High-efficiency organic light-emitting diodes with fluorescent emitters.* Nature communications, 2014. **5**: p. 4016.

35. Yang, X., X. Xu, and G. Zhou, *Recent advances of the emitters for high performance deep-blue organic light-emitting diodes.* Journal of Materials Chemistry C, 2015. **3**(5): p. 913-944.

36. Ide, N., et al., *Photoluminescence properties of facial-and meridional-Ir (ppy) 3 thin films.* Thin Solid Films, 2006. **509**(1-2): p. 164-167.

37. Endo, A., et al., *Efficient up-conversion of triplet excitons into a singlet state and its application for organic light emitting diodes.* Applied Physics Letters, 2011. **98**(8): p. 42.

38. Volz, D., *Review of organic light-emitting diodes with thermally activated delayed fluorescence emitters for energy-efficient sustainable light sources and displays.* Journal of Photonics for Energy, 2016. **6**(2): p. 020901-020901.

39. Adamovich, V.I., et al., *New charge-carrier blocking materials for high efficiency OLEDs.* Organic electronics, 2003. **4**(2): p. 77-87.

40. Ikai, M., et al., *Highly efficient phosphorescence from organic light-emitting devices with an exciton-block layer.* Applied Physics Letters, 2001. **79**(2): p. 156-158.

41. Brütting, W., et al., *Device efficiency of organic light-emitting diodes: Progress by improved light outcoupling.* physica status solidi (a), 2013. **210**(1): p. 44-65.

42. Tsujimura, T., *OLED display fundamentals and applications*. 2017: John Wiley & Sons.

43. Parthasarathy, G., et al., *A metal-free cathode for organic semiconductor devices.* Applied Physics Letters, 1998. **72**(17): p. 2138-2140.

44. Kim, H.-K., et al., *Plasma damage-free sputtering of indium tin oxide cathode layers for top-emitting organic light-emitting diodes.* Applied Physics Letters, 2005. **86**(18): p. 183503.

45. Hofmann, S., et al., *Top-emitting organic light-emitting diodes: Influence of cavity design.* Applied Physics Letters, 2010. **97**(25): p. 278.

46. https://commons.wikimedia.org/wiki/File:LG%EC%A0%84%EC%9E%90, E.B.C.E.B.A.E.E.E.E.A.

47. https://commons.wikimedia.org/wiki/File:Samsung_Galaxy_S6_edge%2B.jpg,.

48. https://commons.wikimedia.org/wiki/File:EL-Light_(OLED)_1.jpg,

49. https://commons.wikimedia.org/wiki/User:Darkweasel94/Clocks/2015_December_21-31.

50. Schadt, M. and W. Helfrich, *Voltage-dependent optical activity of a twisted nematic liquid crystal.* Applied Physics Letters, 1971. **18**(4): p. 127-128.

51. Mentley, D.E., *State of flat-panel display technology and future trends.* Proceedings of the IEEE, 2002. **90**(4): p. 453-459.

52. Birnstock, J., et al., *Screen-printed passive matrix displays based on light-emitting polymers.* Applied Physics Letters, 2001. **78**(24): p. 3905-3907.

53. Stewart, M., et al., *Polysilicon TFT technology for active matrix OLED displays.* IEEE transactions on electron devices, 2001. **48**(5): p. 845-851.

54. Stewart, R.G. and A.C. Ipri, *Active matrix organic light emitting diode (amoled) display pixel structure and data load/illuminate circuit therefor*. 1999, Google Patents.

55. Available from: https://www.eia.gov/tools/faqs/faq.php?id=99&t=3.

56. Schubert, E.F. and J.K. Kim, *Solid-state light sources getting smart.* Science, 2005. **308**(5726): p. 1274-1278.

57. https://energy.gov/eere/ssl/downloads/solid-state-lighting-2016-rd-plan. *Solid State Lighting 2016 R&D Plan*. 2016; Available from: https://energy.gov/eere/ssl/downloads/solid-state-lighting-2016-rd-plan.

58. Available from: http://oled.com/ Accessed on 03/23/2018.

59. Park, J., D. Shin, and S. Park, *Large-area OLED lightings and their applications.* Semiconductor Science and Technology, 2011. **26**(3): p. 034002.

60. Laaperi, A., *OLED lifetime issues from a mobile-phone-industry point of view.* Journal of the Society for Information Display, 2008. **16**(11): p. 1125-1130.

61. Popovic, Z.D. and H. Aziz, *Reliability and degradation of small molecule-based organic light-emitting devices (OLEDs).* IEEE Journal of selected topics in quantum electronics, 2002. **8**(2): p. 362-371.

62. Burrows, P., et al., *Reliability and degradation of organic light emitting devices.* Applied Physics Letters, 1994. **65**(23): p. 2922-2924.

63. McElvain, J., et al., *Formation and growth of black spots in organic light-emitting diodes.* Journal of Applied Physics, 1996. **80**(10): p. 6002-6007.

64. Ke, L., et al., *Degradation and failure of organic light-emitting devices.* Applied physics letters, 2002. **80**(12): p. 2195-2197.

65. Sasabe, H., et al., *3, 3'-Bicarbazole-Based Host Materials for High-Efficiency Blue Phosphorescent OLEDs with Extremely Low Driving Voltage.* Advanced Materials, 2012. **24**(24): p. 3212-3217.

66. Scholz, S., et al., *Degradation mechanisms and reactions in organic light-emitting devices.* Chemical reviews, 2015. **115**(16): p. 8449-8503.

67. Aziz, H., et al., *Degradation mechanism of small molecule-based organic light-emitting devices.* Science, 1999. **283**(5409): p. 1900-1902.

68. Murawski, C., K. Leo, and M.C. Gather, *Efficiency roll-off in organic light-emitting diodes.* Advanced Materials, 2013. **25**(47): p. 6801-6827.

69. Giebink, N. and S. Forrest, *Quantum efficiency roll-off at high brightness in fluorescent and phosphorescent organic light emitting diodes.* Physical Review B, 2008. **77**(23): p. 235215.

70. Erickson, N.C. and R.J. Holmes, *Investigating the Role of Emissive Layer Architecture on the Exciton Recombination Zone in Organic Light-Emitting Devices.* Advanced Functional Materials, 2013. **23**(41): p. 5190-5198.

71. Yersin, H., et al., *The triplet state of organo-transition metal compounds. Triplet harvesting and singlet harvesting for efficient OLEDs.* Coordination Chemistry Reviews, 2011. **255**(21): p. 2622-2652.

72. Mladenovski, S., et al., *Integrated optical model for organic light-emitting devices.* Journal of Applied Physics, 2011. **109**(8): p. 083114.

73. Schmidt, T.D., et al., *Efficiency analysis of organic light-emitting diodes based on optical simulations.* IEEE Journal of Selected Topics in Quantum Electronics, 2013. **19**(5): p. 1-12.

74. Smith, L.H., et al., *Light Out-Coupling Efficiencies of Organic Light-Emitting Diode Structures and the Effect of Photoluminescence Quantum Yield.* Advanced Functional Materials, 2005. **15**(11): p. 1839-1844.

75. Bathelt, R., et al., *Light extraction from OLEDs for lighting applications through light scattering.* Organic Electronics, 2007. **8**(4): p. 293-299.

76. Möller, S. and S. Forrest, *Improved light out-coupling in organic light emitting diodes employing ordered microlens arrays.* Journal of Applied Physics, 2002. **91**(5): p. 3324-3327.

77. Nakamura, T., et al., *Thin-film waveguiding mode light extraction in organic electroluminescent device using high refractive index substrate.* Journal of applied physics, 2005. **97**(5): p. 054505.

78. Mladenovski, S., et al., *Exceptionally efficient organic light emitting devices using high refractive index substrates.* Optics Express, 2009. **17**(9): p. 7562-7570.

79. Reineke, S., et al., *White organic light-emitting diodes with fluorescent tube efficiency.* Nature, 2009. **459**(7244): p. 234.

80. Sun, Y. and S.R. Forrest, *Enhanced light out-coupling of organic light-emitting devices using embedded low-index grids.* Nature photonics, 2008. **2**(8): p. 483.

81. Kim, J.B., et al., *Highly Enhanced Light Extraction from Surface Plasmonic Loss Minimized Organic Light-Emitting Diodes.* Advanced Materials, 2013. **25**(26): p. 3571-3577.

82. Frischeisen, J., et al., *Light extraction from surface plasmons and waveguide modes in an organic light-emitting layer by nanoimprinted gratings.* Optics express, 2011. **19**(101): p. A7-A19.

83. Flämmich, M., et al., *Oriented phosphorescent emitters boost OLED efficiency.* Organic Electronics, 2011. **12**(10): p. 1663-1668.

84. Kim, S.Y., et al., *Organic Light-Emitting diodes with 30% external quantum efficiency based on a horizontally oriented emitter.* Advanced Functional Materials, 2013. **23**(31): p. 3896-3900.

85. Brütting, W., *Physics of organic semiconductors*. 2006: John Wiley & Sons.

86. Köhler, A. and H. Bässler, *Electronic processes in organic semiconductors: An introduction*. 2015: John Wiley & Sons.

87. Atkins, P. and J. De Paula, *Elements of physical chemistry*. 2013: Oxford University Press, USA.

88. Koopmans, T., *Über die Zuordnung von Wellenfunktionen und Eigenwerten zu den einzelnen Elektronen eines Atoms.* Physica, 1934. **1**(1-6): p. 104-113.

89. Schwoerer, M. and H.C. Wolf, *Organic molecular solids*. 2007: John Wiley & Sons.

90. Frenkel, J., *On the transformation of light into heat in solids. I.* Physical Review, 1931. **37**(1): p. 17.

91. Wannier, G.H., *The structure of electronic excitation levels in insulating crystals.* Physical Review, 1937. **52**(3): p. 191.

92. Zhu, X.-Y., Q. Yang, and M. Muntwiler, *Charge-transfer excitons at organic semiconductor surfaces and interfaces.* Accounts of chemical research, 2009. **42**(11): p. 1779-1787.

93. Pope, M. and C.E. Swenberg, *Electronic processes in organic crystals and polymers*. 1999: Oxford University Press on Demand.

94. Kasha, M., *Characterization of electronic transitions in complex molecules.* Discussions of the Faraday society, 1950. **9**: p. 14-19.

95. Yersin, H., *Highly efficient OLEDs with phosphorescent materials*. 2008: John Wiley & Sons.

96. Salas Redondo, C., et al., *Interplay of Fluorescence and Phosphorescence in Organic Biluminescent Emitters.* The Journal of Physical Chemistry C, 2017. **121**(27): p. 14946-14953.

97. Fox, M., *Optical properties of solids*. 2002, AAPT.

98. Lax, M., *The Franck-Condon Principle and Its Application to Crystals.* The Journal of Chemical Physics, 1952. **20**(11): p. 1752-1760.

99. Turro, N.J., *Modern molecular photochemistry*. 1991: University science books.

100. Förster, T., *Zwischenmolekulare energiewanderung und fluoreszenz.* Annalen der physik, 1948. **437**(1-2): p. 55-75.

101. Wong, K.F., B. Bagchi, and P.J. Rossky, *Distance and orientation dependence of excitation transfer rates in conjugated systems: beyond the Förster theory.* The Journal of Physical Chemistry A, 2004. **108**(27): p. 5752-5763.

102. Dexter, D.L., *A theory of sensitized luminescence in solids.* The Journal of Chemical Physics, 1953. **21**(5): p. 836-850.

103. Simmons, J., *Richardson-Schottky effect in solids.* Physical Review Letters, 1965. **15**(25): p. 967.

104. Simmons, J.G., *Poole-Frenkel effect and Schottky effect in metal-insulator-metal systems.* Physical Review, 1967. **155**(3): p. 657.

105. Arkhipov, V., et al., *Charge injection into light-emitting diodes: Theory and experiment.* Journal of Applied Physics, 1998. **84**(2): p. 848-856.

106. Helander, M., et al., *Band alignment at metal/organic and metal/oxide/organic interfaces.* Applied Physics Letters, 2008. **93**(19): p. 412.

107. Scott, J.C., *Metal–organic interface and charge injection in organic electronic devices.* Journal of Vacuum Science & Technology A: Vacuum, Surfaces, and Films, 2003. **21**(3): p. 521-531.

108. Bässler, H. and A. Köhler, *Charge transport in organic semiconductors*, in *Unimolecular and supramolecular electronics I*. 2011, Springer. p. 1-65.

109. Yuan, Y., et al., *Ultra-high mobility transparent organic thin film transistors grown by an off-centre spin-coating method.* Nature communications, 2014. **5**: p. 3005.

110. Brütting, W., S. Berleb, and A.G. Mückl, *Device physics of organic light-emitting diodes based on molecular materials.* Organic electronics, 2001. **2**(1): p. 1-36.

111. Lampert, M.A., *Volume-controlled current injection in insulators.* Reports on Progress in Physics, 1964. **27**(1): p. 329.

112. Troisi, A. and G. Orlandi, *Charge-transport regime of crystalline organic semiconductors: diffusion limited by thermal off-diagonal electronic disorder.* Physical review letters, 2006. **96**(8): p. 086601.

113. Burrows, P. and S. Forrest, *Electroluminescence from trap-limited current transport in vacuum deposited organic light emitting devices.* Applied Physics Letters, 1994. **64**(17): p. 2285-2287.

114. Mark, P. and W. Helfrich, *Space-charge-limited currents in organic crystals.* Journal of Applied Physics, 1962. **33**(1): p. 205-215.

115. Langevin, P., *Recombinaison et mobilites des ions dans les gaz.* Ann. Chim. Phys, 1903. **28**(433): p. 122.

116. Hall, R.N., *Electron-hole recombination in germanium.* Physical review, 1952. **87**(2): p. 387.

117. Shockley, W. and W. Read Jr, *Statistics of the recombinations of holes and electrons.* Physical review, 1952. **87**(5): p. 835.

118. Kuik, M., et al., *Trap-assisted recombination in disordered organic semiconductors.* Physical review letters, 2011. **107**(25): p. 256805.

119. Ishida, H., et al., *Recent advances in instrumentation for absolute emission quantum yield measurements.* Coordination chemistry reviews, 2010. **254**(21-22): p. 2449-2458.

120. Brouwer, A.M., *Standards for photoluminescence quantum yield measurements in solution (IUPAC Technical Report).* Pure and Applied Chemistry, 2011. **83**(12): p. 2213-2228.

121. Woollam, J.A., et al. *Overview of variable-angle spectroscopic ellipsometry (VASE): I. Basic theory and typical applications*. in *Optical Metrology: A Critical Review*. 1999. International Society for Optics and Photonics.

122. Flack, W.W., et al., *A mathematical model for spin coating of polymer resists.* Journal of Applied Physics, 1984. **56**(4): p. 1199-1206.

123. Kennard, E.H., *Kinetic theory of gases, with an introduction to statistical mechanics.* 1938.

124. Forrest, S.R., D.D. Bradley, and M.E. Thompson, *Measuring the Efficiency of Organic Light-Emitting Devices.* Advanced Materials, 2003. **15**(13): p. 1043-1048.

125. Udagawa, K., et al., *Simultaneous Realization of High EQE of 30%, Low Drive Voltage, and Low Efficiency Roll-Off at High Brightness in Blue Phosphorescent OLEDs.* Advanced Optical Materials, 2016. **4**(1): p. 86-90.

126. Kim, K.H., et al., *Phosphorescent dye-based supramolecules for high-efficiency organic light-emitting diodes.* Nat Commun, 2014. **5**: p. 4769.

127. Baldo, M.A., et al., *Very high-efficiency green organic light-emitting devices based on electrophosphorescence.* Applied Physics Letters, 1999. **75**(1): p. 4.

128. Han, L., et al., *The reduced triplet-triplet annihilation of electrophosphorescent device doped by an iridium complex with active hydrogen.* Applied Physics Letters, 2008. **93**(15): p. 153303.

129. Yang, D., et al., *A very high efficiency electrophosphorescent device doped with short triplet lifetime phosphor using multi-recombination zones.* Journal of Physics D: Applied Physics, 2010. **43**(10): p. 105101.

130. Reineke, S., et al., *Improved High-Brightness Efficiency of Phosphorescent Organic LEDs Comprising Emitter Molecules with Small Permanent Dipole Moments.* Advanced Materials, 2010. **22**(29): p. 3189-3193.

131. Erickson, N.C. and R.J. Holmes, *Engineering Efficiency Roll-Off in Organic Light-Emitting Devices.* Advanced Functional Materials, 2014. **24**(38): p. 6074-6080.

132. Reineke, S., K. Walzer, and K. Leo, *Triplet-exciton quenching in organic phosphorescent light-emitting diodes with Ir-based emitters.* Physical Review B, 2007. **75**(12): p. 125328.

133. Jeon, S.K. and J.Y. Lee, *Direct monitoring of recombination zone shift during lifetime measurement of phosphorescent organic light-emitting diodes.* Journal of Industrial and Engineering Chemistry, 2015. **32**: p. 332-335.

134. He, G., et al., *High-efficiency and low-voltage p-i-n electrophosphorescent organic light-emitting diodes with double-emission layers.* Applied Physics Letters, 2004. **85**(17): p. 3911.

135. Lee, J., J.-I. Lee, and H.Y. Chu, *Investigation of double emissive layer structures on phosphorescent blue organic light-emitting diodes.* Synthetic Metals, 2009. **159**(14): p. 1460-1463.

136. Hsiao, C.-H., J.-H. Lee, and C.-A. Tseng, *Probing recombination-rate distribution in organic light-emitting devices with mixed-emitter structure.* Chemical Physics Letters, 2006. **427**(4-6): p. 305-309.

137. Kim, S.H., J. Jang, and J.Y. Lee, *Relationship between host energy levels and device performances of phosphorescent organic light-emitting diodes with triplet mixed host emitting structure.* Applied Physics Letters, 2007. **91**(8): p. 083511.

138. Kim, S.H., et al., *Stable efficiency roll-off in phosphorescent organic light-emitting diodes.* Applied Physics Letters, 2008. **92**(2): p. 023513.

139. Lee, J.-H., et al., *Mixed host organic light-emitting devices with low driving voltage and long lifetime.* Applied Physics Letters, 2005. **86**(10): p. 103506.

140. Erickson, N.C. and R.J. Holmes, *Highly efficient, single-layer organic light-emitting devices based on a graded-composition emissive layer.* Applied Physics Letters, 2010. **97**(8): p. 083308.

141. Liu, S.W., X.W. Sun, and H.V. Demir, *Graded-host phosphorescent light-emitting diodes with high efficiency and reduced roll-off.* AIP Advances, 2012. **2**(1): p. 012192.

142. Lindla, F., et al., *Highly efficient yellow organic light emitting diode based on a layer-cross faded emission layer allowing easy color tuning.* Applied Physics Letters, 2009. **95**(21): p. 308.

143. Erickson, N.C. and R.J. Holmes, *Relating charge transport and performance in single-layer graded-composition organic light-emitting devices.* Journal of Applied Physics, 2011. **110**(8): p. 084515.

144. Yook, K.S. and J.Y. Lee, *Recombination zone study of phosphorescent organic light-emitting diodes with triplet mixed host emitting structure.* Journal of Industrial and Engineering Chemistry, 2010. **16**(2): p. 181-184.

145. Chaskar, A., H.F. Chen, and K.T. Wong, *Bipolar host materials: a chemical approach for highly efficient electrophosphorescent devices.* Advanced Materials, 2011. **23**(34): p. 3876-3895.

146. Cui, L.S., et al., *Benzimidazobenzothiazole-Based Bipolar Hosts to Harvest Nearly All of the Excitons from Blue Delayed Fluorescence and Phosphorescent Organic Light-Emitting Diodes.* Angewandte Chemie International Edition, 2016. **55**(24): p. 6864-6868.

147. Zhao, Y., et al., *New Benzimidazole-Based Bipolar Hosts: Highly Efficient Phosphorescent and Thermally Activated Delayed Fluorescent Organic Light-Emitting Diodes Employing the Same Device Structure.* ACS applied materials & interfaces, 2016. **8**(4): p. 2635-2643.

148. Ingram, G.L., C. Nguyen, and Z.-H. Lu, *Long-Range Energy Transfer and Singlet-Exciton Migration in Working Organic Light-Emitting Diodes.* Physical Review Applied, 2016. **5**(6): p. 064002.

149. Tang, C.W., S.A. VanSlyke, and C. Chen, *Electroluminescence of doped organic thin films.* Journal of Applied Physics, 1989. **65**(9): p. 3610-3616.

150. Lam, J., et al., *Selective doping of multilayer organic light emitting devices.* Journal of Vacuum Science & Technology A: Vacuum, Surfaces, and Films, 2000. **18**(2): p. 593-596.

151. Beierlein, T., et al., *Investigation of internal processes in organic light-emitting devices using thin sensing layers.* Synthetic metals, 2003. **138**(1): p. 213-221.

152. Wünsche, J., et al., *Measurement of triplet exciton diffusion in organic light-emitting diodes.* Physical Review B, 2010. **81**(24): p. 245201.

153. Van Mensfoort, S., et al., *Measuring the light emission profile in organic light-emitting diodes with nanometre spatial resolution.* Nature Photonics, 2010. **4**(5): p. 329-335.

154. Matsushima, T., K. Goushi, and C. Adachi, *Charge-carrier injection characteristics at organic/organic heterojunction interfaces in organic light-emitting diodes.* Chemical physics letters, 2007. **435**(4): p. 327-330.

155. Cheon, K. and J. Shinar, *Förster energy transfer in combinatorial arrays of selective doped organic light-emitting devices.* Applied physics letters, 2004. **84**(7): p. 1201-1203.

156. Kawamura, Y., et al., *Intermolecular interaction and a concentration-quenching mechanism of phosphorescent Ir (III) complexes in a solid film.* Physical review letters, 2006. **96**(1): p. 017404.

157. Brunner, K., et al., *Carbazole compounds as host materials for triplet emitters in organic light-emitting diodes: tuning the HOMO level without influencing the triplet energy in small molecules.* Journal of the American Chemical Society, 2004. **126**(19): p. 6035-6042.

158. Kang, J.-W., et al., *Low roll-off of efficiency at high current density in phosphorescent organic light emitting diodes.* Applied physics letters, 2007. **90**(22): p. 223508.

159. Baldo, M. and S. Forrest, *Transient analysis of organic electrophosphorescence: I. Transient analysis of triplet energy transfer.* Physical Review B, 2000. **62**(16): p. 10958.

160. Luo, Y. and H. Aziz, *Correlation Between Triplet–Triplet Annihilation and Electroluminescence Efficiency in Doped Fluorescent Organic Light-Emitting Devices.* Advanced Functional Materials, 2010. **20**(8): p. 1285-1293.

161. van Eersel, H., et al., *Effect of Förster-mediated triplet-polaron quenching and triplet-triplet annihilation on the efficiency roll-off of organic light-emitting diodes.* Journal of Applied Physics, 2016. **119**(16): p. 163102.

162. Tessler, N., et al., *Efficient near-infrared polymer nanocrystal light-emitting diodes.* Science, 2002. **295**(5559): p. 1506-1508.

163. Lim, Y.T., et al., *Selection of quantum dot wavelengths for biomedical assays and imaging.* Molecular Imaging, 2003. **2**(1): p. 50-64.

164. Graham, K.R., et al., *Extended conjugation platinum (II) porphyrins for use in near-infrared emitting organic light emitting diodes.* Chemistry of Materials, 2011. **23**(24): p. 5305-5312.

165. Eliseeva, S.V. and J.-C.G. Bünzli, *Lanthanide luminescence for functional materials and bio-sciences.* Chemical Society Reviews, 2010. **39**(1): p. 189-227.

166. Katkova, M.A. and M.N. Bochkarev, *New trends in design of electroluminescent rare earth metallo-complexes for OLEDs.* Dalton Transactions, 2010. **39**(29): p. 6599-6612.

167. Stender, B., et al., *Optoelectronic processes in squaraine dye-doped OLEDs for emission in the near-infrared.* Advanced Materials, 2013. **25**(21): p. 2943-2947.

168. Yang, R., et al., *Deep-red electroluminescent polymers: synthesis and characterization of new low-band-gap conjugated copolymers for cight-emitting diodes and photovoltaic devices.* Macromolecules, 2004. **38**(2): p. 244-253.

169. H Sargent, E., *Infrared quantum dots.* Advanced Materials, 2005. **17**(5): p. 515-522.

170. Shirasaki, Y., et al., *Emergence of colloidal quantum-dot light-emitting technologies.* Nature Photonics, 2013. **7**(1): p. 13.

171. Cheng, K.-Y., et al., *High-efficiency silicon nanocrystal light-emitting devices.* Nano Letters, 2011. **11**(5): p. 1952-1956.

172. Pons, T., et al., *Cadmium-free CuInS2/ZnS quantum dots for sentinel lymph node imaging with reduced toxicity.* ACS Nano, 2010. **4**(5): p. 2531-2538.

173. Niesen, B. and B.P. Rand, *Thin Film Metal Nanocluster Light-Emitting Devices.* Advanced Materials, 2014. **26**(9): p. 1446-1449.

174. Tan, Z.-K., et al., *Bright light-emitting diodes based on organometal halide perovskite.* Nature Nanotechnology, 2014. **9**: p. 687-692.

175. Fu, H. and A. Zunger, *InP quantum dots: Electronic structure, surface effects, and the redshifted emission.* Physical Review B, 1997. **56**(3): p. 1496.

176. Cuny, J.r.m., et al., *95Mo solid-state nuclear magnetic resonance spectroscopy and quantum simulations: synergetic tools for the study of molybdenum cluster materials.* Inorganic Chemistry, 2012. **52**(2): p. 617-627.

177. Ghosh, R.N., et al., *Fiber-optic oxygen sensor using molybdenum chloride cluster luminescence.* Applied Physics Letters, 1999. **75**(19): p. 2885-2887.

178. Zhao, Y. and R.R. Lunt, *Transparent Luminescent Solar Concentrators for Large-Area Solar Windows Enabled by Massive Stokes-Shift Nanocluster Phosphors.* Advanced Energy Materials, 2013. **3**(9): p. 1143-1148.

179. Blomstrand, W., *Ueber unorganische Haloidverbindungen, die sich wie Radicale verhalten.* Advanced Synthesis & Catalysis, 1859. **77**(1): p. 88-119.

180. Brosset, C., *The structure of complex compounds of bivalent molybdenum. III. X-ray analysis of the structure of the chloro acid in alcohol solution.* Arkiv. Kemi, 1949. **1**: p. 353.

181. Nannelli, P., et al., *Molybdenum (II) halides.* Inorg. Synth, 1970. **12**: p. 170.

182. Dorman, W. and R. McCarley, *Chemistry of the polynuclear metal halides. XII. Preparation of molybdenum and tungsten M6X84+ clusters by reduction of higher halides in molten sodium halide--aluminum halide mixtures.* Inorganic Chemistry, 1974. **13**(2): p. 491-493.

183. Koknat, F., et al., *Convenient synthesis of the hexanuclear molybdenum (II) halides Mo6Cl12 and Mo6Br12· 2H2O.* Inorganic and Nuclear Chemistry Letters, 1980. **16**(5): p. 307-310.

184. Hay, D.N., et al., *Facile reduction of early transition metal halides with nonconventional, mild reductants. 6. A new, lower-temperature, solid-state synthesis of the cluster hexamolybdenum dodecachloride Mo6Cl12 from MoCl5, via chloromolybdic acid,(H3O) 2 [Mo6 (μ3-Cl) 8Cl6]· 6H2O.* Inorganica chimica acta, 2004. **357**(3): p. 644-648.

185. Saito, Y., et al., *Temperature dependence of the luminescence lifetime of hexanuclear molybdenum (II) chloride cluster. Identification of lower excited triplet sublevels.* The Journal of Physical Chemistry, 1985. **89**(21): p. 4413-4415.

186. Blessing, R., *SADABS V2.008/2 Program for absorption corrections using Bruker-AXS CCD based on the method of Robert Blessing.* Acta Crystallographica Section A: Foundations of Crystallography, 1995. **A51**: p. 33-38.

187. Sheldrick, G.M., *A short history of SHELX.* Acta Crystallographica Section A: Foundations of Crystallography, 2007. **64**(1): p. 112-122.

188. Dolomanov, O.V., et al., *OLEX2: a complete structure solution, refinement and analysis program.* Journal of Applied Crystallography, 2009. **42**(2): p. 339-341.

189. Casida, M.E., et al., *Molecular excitation energies to high-lying bound states from time-dependent density-functional response theory: Characterization and correction of the time-dependent local density approximation ionization threshold.* The Journal of Chemical Physics, 1998. **108**(11): p. 4439-4449.

190. Gross, E. and W. Kohn, *Local density-functional theory of frequency-dependent linear response.* Physical Review Letters, 1985. **55**(26): p. 2850.

191. Yanai, T., D.P. Tew, and N.C. Handy, *A new hybrid exchange–correlation functional using the Coulomb-attenuating method (CAM-B3LYP).* Chemical Physics Letters, 2004. **393**(1): p. 51-57.

192. Wadt, W.R. and P.J. Hay, *Ab initio effective core potentials for molecular calculations. Potentials for main group elements Na to Bi.* The Journal of Chemical Physics, 1985. **82**(1): p. 284-298.

193. Shao, Y., et al., *Advances in methods and algorithms in a modern quantum chemistry program package.* Physical Chemistry Chemical Physics, 2006. **8**(27): p. 3172-3191.

194. Becke, A.D., *Density-functional thermochemistry. III. The role of exact exchange.* The Journal of Chemical Physics, 1993. **98**(7): p. 5648-5652.

195. Stephens, P., et al., *Ab initio calculation of vibrational absorption and circular dichroism spectra using density functional force fields.* The Journal of Physical Chemistry, 1994. **98**(45): p. 11623-11627.

196. Peumans, P. and S. Forrest, *Very-high-efficiency double-heterostructure copper phthalocyanine/C60 photovoltaic cells.* Applied Physics Letters, 2001. **79**(1): p. 126-128.

197. Yang, X.H., et al., *Efficient polymer electrophosphorescent devices with interfacial layers.* Advanced Functional Materials, 2006. **16**(16): p. 2156-2162.

198. Maverick, A.W., et al., *Spectroscopic, electrochemical, and photochemical properties of molybdenum (II) and tungsten (II) halide clusters.* Journal of the American Chemical Society, 1983. **105**(7): p. 1878-1882.

199. Kovalenko, M.V., M. Scheele, and D.V. Talapin, *Colloidal nanocrystals with molecular metal chalcogenide surface ligands.* Science, 2009. **324**(5933): p. 1417-1420.

200. Nag, A., et al., *Effect of metal ions on photoluminescence, charge transport, magnetic and catalytic properties of all-inorganic colloidal nanocrystals and nanocrystal solids.* Journal of the American Chemical Society, 2012. **134**(33): p. 13604-13615.

201. Martin, R.L., *Natural transition orbitals.* The Journal of Chemical Physics, 2003. **118**(11): p. 4775-4777.

202. Koh, T.-W., et al., *Metal nanocluster light-emitting devices with suppressed parasitic emission and improved efficiency: exploring the impact of photophysical properties.* Nanoscale, 2015. **7**(20): p. 9140-9146.

203. Xie, M., et al., *White electroluminescent phosphine-chelated copper iodide nanoclusters.* Chemistry of Materials, 2017. **29**(16): p. 6606-6610.

204. Kuttipillai, P.S., et al., *Phosphorescent Nanocluster Light-Emitting Diodes.* Advanced Materials, 2016. **28**(2): p. 320-326.

205. Kamiguchi, S., et al., *Catalytic ring-attachment isomerization and dealkylation of diethylbenzenes over halide clusters of group 5 and group 6 transition metals.* Journal of Catalysis, 2004. **223**(1): p. 54-63.

206. Kamiguchi, S., et al., *Catalytic dehydrohalogenation of alkyl halides by Nb, Mo, Ta, and W halide clusters with an octahedral metal framework and by a Re chloride cluster with a triangular metal framework.* Journal of Molecular Catalysis A: Chemical, 2003. **203**(1): p. 153-163.

207. Fucugauchi, L., et al., *Chemical effects of (n, γ) nuclear reaction on (Mo 6 Cl 8) Cl 4.* Journal of radioanalytical and nuclear chemistry, 1994. **178**(2): p. 437-442.

208. Christiano, S.P. and T.J. Pinnavaia, *Intercalation in montmorillonite of molybdenum cations containing the Mo6Cl8 cluster core.* Journal of Solid State Chemistry, 1986. **64**(3): p. 232-239.

209. Neaime, C., et al., *Time-gated luminescence bioimaging with new luminescent nanocolloids based on [Mo 6 I 8 (C 2 F 5 COO) 6] 2− metal atom clusters.* Physical Chemistry Chemical Physics, 2016. **18**(43): p. 30166-30173.

210. Sokolov, M.N., et al., *Highly luminescent complexes [Mo 6 X 8 (nC 3 F 7 COO) 6] 2−(X= Br, I).* Dalton Transactions, 2011. **40**(24): p. 6375-6377.

211. Ströbele, M., R. Thalwitzer, and H.-J.r. Meyer, *Facile Way of Synthesis for Molybdenum Iodides.* Inorganic chemistry, 2016. **55**(22): p. 12074-12078.

212. Kirakci, K., et al., *A highly luminescent hexanuclear molybdenum cluster–A promising candidate toward photoactive materials.* European Journal of Inorganic Chemistry, 2012. **2012**(19): p. 3107-3111.

213. Amela-Cortes, M., et al., *Versatility of the ionic assembling method to design highly luminescent PMMA nanocomposites containing [M 6 Q i 8 L a 6] n− octahedral nano-building blocks.* Dalton Transactions, 2016. **45**(1): p. 237-245.

214. Riehl, L., et al., *Molecular Oxygen Modulated Luminescence of an Octahedro-hexamolybdenum Iodide Cluster having Six Apical Thiocyanate Ligands.* Zeitschrift für anorganische und allgemeine Chemie, 2016. **642**(5): p. 403-408.

215. Akagi, S., et al., *Zero-Magnetic-Field Splitting in the Excited Triplet States of Octahedral Hexanuclear Molybdenum (II) Clusters:[{Mo6X8}(n-C3F7COO) 6] 2–(X= Cl, Br, or I).* The Journal of Physical Chemistry A, 2017. **121**(38): p. 7148-7156.

216. Karl, N., *Charge carrier transport in organic semiconductors.* Synthetic Metals, 2003. **133**: p. 649-657.

217. Kirakci, K., et al., *Hexamolybdenum cluster complexes with pyrene and anthracene carboxylates: ultrabright red emitters with the antenna effect.* European Journal of Inorganic Chemistry, 2014. **2014**(14): p. 2331-2336.

218. Newsham, M.D., *Excited-sate properties of transition-metal complexes in solution and the solid state*, in *Chemistry*. 1988, Michigan State University: East Lansing.

219. Gabriel, J.-C.P., et al., *Chemistry of hexanuclear rhenium chalcohalide clusters.* Chemical reviews, 2001. **101**(7): p. 2037-2066.

220. Lunt, R.R., J.B. Benziger, and S.R. Forrest, *Growth of an ordered crystalline organic heterojunction.* Advanced Materials, 2007. **19**(23): p. 4229-4233.

221. Wang, L., et al., *Unlocking the Single-Domain Epitaxy of Halide Perovskites.* Advanced Materials Interfaces, 2017. **4**(22).

222. Chen, P., et al., *Homoepitaxial growth of metal halide crystals investigated by reflection high-energy electron diffraction.* Scientific reports, 2017. **7**: p. 40542.

223. Mangolini, L., E. Thimsen, and U. Kortshagen, *High-yield plasma synthesis of luminescent silicon nanocrystals.* Nano letters, 2005. **5**(4): p. 655-659.

224. Mangolini, L., et al., *Plasma synthesis and liquid-phase surface passivation of brightly luminescent Si nanocrystals.* Journal of luminescence, 2006. **121**(2): p. 327-334.

225. Ditchfield, R., W.J. Hehre, and J.A. Pople, *Self-consistent molecular-orbital methods. IX. An extended Gaussian-type basis for molecular-orbital studies of organic molecules.* The Journal of Chemical Physics, 1971. **54**(2): p. 724-728

226. Frisch, M.J.T., G. W.; Schlegel, H. B.; Scuseria, G. E.; Robb, M. A.; Cheeseman, J. R.; Montgomery, Jr., J. A.; Vreven, T.; Kudin, K. N.; Burant, J. C.; Millam, J. M.; Iyengar, S. S.; Tomasi, J.; Barone, V.; Mennucci, B.; Cossi, M.; Scalmani, G.; Rega, N.; Petersson, G. A.; Nakatsuji, H.; Hada, M.; Ehara, M.; Toyota, K.; Fukuda, R.; Hasegawa, J.; Ishida, M.; Nakajima, T.; Honda, Y.; Kitao, O.; Nakai, H.; Klene, M.; Li, X.; Knox, J. E.; Hratchian, H. P.; Cross, J. B.; Bakken, V.; Adamo, C.; Jaramillo, J.; Gomperts, R.; Stratmann, R. E.; Yazyev, O.; Austin, A. J.; Cammi, R.; Pomelli, C.; Ochterski, J. W.; Ayala, P. Y.; Morokuma, K.; Voth, G. A.; Salvador, P.; Dannenberg, J. J.; Zakrzewski, V. G.; Dapprich, S.; Daniels, A. D.; Strain, M. C.; Farkas, O.; Malick, D. K.; Rabuck, A. D.; Raghavachari, K.; Foresman, J. B.; Ortiz, J. V.; Cui, Q.; Baboul, A. G.; Clifford, S.; Cioslowski, J.; Stefanov, B. B.; Liu, G.; Liashenko, A.; Piskorz, P.; Komaromi, I.; Martin, R. L.; Fox, D. J.; Keith, T.; Al-Laham, M. A.; Peng, C. Y.; Nanayakkara, A.; Challacombe, M.; Gill, P. M. W.; Johnson, B.; Chen, W.; Wong, M. W.; Gonzalez, C.; and Pople, J. A, *Gaussian 09, revision A. 02*. 2009, Gaussian, Inc., Wallingford CT.

227. D'Andrade, B.W., et al., *Relationship between the ionization and oxidation potentials of molecular organic semiconductors.* Organic Electronics, 2005. **6**(1): p. 11-20.

228. Djurovich, P.I., et al., *Measurement of the lowest unoccupied molecular orbital energies of molecular organic semiconductors.* Organic Electronics, 2009. **10**(3): p. 515-520.